UNIVERSITY OF SOUTHAMPTON

Tantalum Pentoxide Waveguides for Photonic Crystal Circuits

Chao-Yi Tai

A thesis submitted for the degree of Doctor of Philosophy

School of Physics and Astronomy & Optoelectronics Research Centre

Faculty of Engineering, Science and Mathematics

May 2004

UNIVERSITY OF SOUTHAMPTON

ABSTRACT

Faculty of Engineering, Science and Mathematics
School of Physics and Astronomy & Optoelectronics Research Centre

Doctor of Philosophy

Tantalum Pentoxide Waveguides for Photonic Crystal Circuits

by Chao-Yi Tai

Tantalum pentoxide is a widely used dielectric material having a high index (n>2.0) and low loss over a wide wavelength range, rendering it suitable for planar lightwave circuits incorporating photonic crystal elements. This thesis presents a study of Ta_2O_5 aimed at exploring its optical properties and demonstrating practical waveguide structures for the construction of Si-compatible densely integrated multifunctional optical waveguide devices.

A reliable fabrication process for Ta_2O_5 rib waveguides with a range of geometries was established and the correlation between the modal field distributions and the waveguide geometries was studied. The results provide useful guidelines for the design of monomode waveguides, particularly at a wavelength of 1550nm, and the structures established were used as effective test beds for a variety of device structures studied in this thesis. The UV photosensitivity of the material was investigated based on a Ta_2O_5 rib waveguide Mach-Zehnder interferometer structure. A significant UV induced index change of $\Delta n=-2.1\times10^{-3}$ at a wavelength of 1550nm was observed in Ta_2O_5 films with no hydrogen loading, demonstrating significant potential advantages for inscribing microstructures and tuning photonic crystals. The optical third-order nonlinearity was examined in a Ta_2O_5 stripe waveguide using self-phase modulation. The large nonlinear refractive index obtained, $n_2\sim7.2\times10^{-19}$ m^2/W, demonstrates the potential of this material for all-optical switching devices. Hybrid integration of a Ta_2O_5 stripe waveguide with a self-assembled microsphere grating was demonstrated as an alternative route to microstructuring. In this study, the waveguide was used as a structure for physically trapping the microspheres and for the interrogation of the grating transmission spectrum. A transmission stop-band close to the Bragg wavelength was observed, demonstrating the feasibility of this potentially cheap method for realising wavelength-dependent devices. Finally, a process for incorporating photonic crystals within Ta_2O_5 rib waveguides was established. The transmission spectra provide evidence of band-gap behaviour, which show promise for future photonic crystal devices incorporating Ta_2O_5 rib waveguides. In particular, the challenge of fabricating perpendicular sidewalls for nano-sized holes has been overcome.

Ta_2O_5 is shown to have great potential as a high-index waveguide material for application in a variety of planar lightwave circuit elements. Routes to solve the remaining development problems identified in this thesis are proposed, so that Ta_2O_5 waveguides may be applied in practical devices.

Table of Contents

List of Figures

List of Tables

Acknowledgements

I would like to express my deepest gratitude to Professor James Wilkinson for his nonstop encouragement and support throughout my PhD period, and giving me the opportunity to work in a professional group, where I can always find experts to get help. I am also grateful to Professor Jeremy Baumberg for his expertise, which inspires me to think and conduct experiments more comprehensively. I am thankful to Professor Philip Bartlett and Dr Mohamed Ghanem for introducing me some interesting chemical processes. I am also thankful to Dr Christos Grivas for his help on the UV laser arrangement. A special thank to the people in Mesophotonics for their assistance.

Finally, I would like to thank my parents, Hui-Wen, and my family for their endless love and very thoughtful support.

Chapter 1 Introduction

1.1 Background and motivation

The concept of integrated optics, inspired by the success of electronic integrated circuits (ICs), was first introduced by Miller in 1969 [1] with the original purpose of replacing discrete optical components so as to avoid multi-stage alignment, and also with the aim of providing a common platform to combine with electronics. The distributed feedback (DFB) laser, achieved by Kogelink in 1971 [2], is a significant breakthrough, where a compact spatially periodic structure was utilized to replace a pair of cavity mirrors, providing stable feedback and flexible spectral selection. With the progress of the thin-film technology, an electrically pumped distributed feedback injection laser was realized. This achievement, made by Scifres in 1974 [3], demonstrates the first example where electronics and optics are combined and share a common substrate. Meanwhile, a number of passive guided wave devices (Mach-Zehnder interferometers, Bragg gratings, optical switches and modulators, for instance) were successfully created by either altering the physical structures or tailoring the material properties (refractive index), both of which may be termed refractive index engineering. However, in contrast to electronic integrated circuits, in which millions of components are integrated on a microchip, the number of optical components that can be integrated is still very limited. The major obstacle that hinders progress is that photons, unlike electrons, suffer considerable attenuation, particularly when being steered around bends with radius comparable to the wavelength. In addition, the difficulty of low-loss fiber-to-chip coupling and

of effective component-to-component interfaces also limits the number of components that can be integrated, slowing down progress towards forming densely integrated planar lightwave circuits (PLCs).

To increase the integration yield, over the years, much effort has been devoted to the development of low-loss, high-index contrast (Δn), and silicon compatible material systems because the device size scales down with increasing Δn [4]. Silicon on insulator (SOI) [5] is a remarkable success which allows the fabrication of low-loss micrometer/nanometer sized passive optical devices utilizing existing silicon integrated circuit processing technology. The III-V semiconductor material systems such as GaAs/GaAlAs and InGaAsP/InP is another prominent achievement. Since these materials have direct band gaps, laser diodes, photodetectors, passive optical components, and optical interconnections can be monolithically integrated on a single substrate. With the successful demonstrations of dense wavelength division multiplexed (DWDM) transmitter/receiver [6], laser and optical amplifier modules [7], tunable multi-channel filter [8] and optical switching matrix [9], integrated optics may be convincingly considered to be the most promising route for low-cost, high-integration-yield, and mass production.

Recently, the concept was further modernized with the emergence of photonic crystals (PCs) - artificially made perforated structures which use a band gap as the wave guiding mechanism instead of conventional index guiding based on the principle of total internal reflection (TIR). Theoretically, it has been shown that PC

waveguides can efficiently guide light around sharp corners, even if the radius of the bend is comparable to the wavelength [10]. This property could not only scale the size of a device down a further order of magnitude but could make the interconnection between separate components ease to achieve. Besides, the band gaps can be flexibly tailored by changing the arrangement of the array of holes, or by varying the index contrast of the materials which comprise the structure. So far, a diversity of applications have been suggested [11] that make photonic crystal waveguides a competitive candidate for photonic platforms.

However, there are still challenging issues facing both the fabrication techniques and the material systems. On the fabrication side, the utilization of high Δn material systems and photonic crystals has pushed the requirement of the smallest feature size further down to the submicron scale. Current techniques such as chemical vapour deposition (CVD) and molecular beam expitaxy (MBE) can deposit atomic layers of dielectrics. However for the "top-down" processes such as patterning and etching, the current techniques (electron beam lithography, focused ion beam, and reactive ion etching) are on the borderline of coping with the stringent fabrication tolerance for point defects in PCs and for sharp tips of tapers. Fabrication errors cause undesired deviations in device performance, particularly in the case of photonic crystals, and extra cost in compensating them. More advanced fabrication techniques and low-cost post-fabrication trimming methods have to be developed to broaden the fabrication tolerance. While on the material side, using III-V semiconductors as platforms provide monolithic integration but the wavelength

range of the emitted light is limited by the available direct band gap range. The larger index-temperature coefficient (dn/dT) requires extra cost on the compensation. Lithium niobate, although incompatible with Si, has important applications in nonlinear optics due to its high electro-optical and acousto-optical coefficients. To date, most of the wavelength conversion devices are based on this material. However, the anisotropic characteristic results in polarization dependent devices. Some polymers exhibiting large nonlinear coefficients, are also attractive candidates due to the ease of fabrication and significantly lower cost than other materials. But their mechanical and long term stability is relatively low. Since each different material has its advantages in specific applications, the competition between material systems is still controversial. It is therefore necessary to pursue material exploration in order to find suitable alternatives or systems compatible with hybrid integration, and compatible with existing material systems to broaden the applications.

Tantalum pentoxide (Ta_2O_5) is a wide-gap, high dielectric constant material which has been widely used in microelectronic devices. It is the motivation of this thesis to assess its potential for sophisticated planar lightwave circuits. To add more functionality and thereby further broaden the applications of waveguide devices, two approaches are demonstrated in this thesis. On the one hand, material properties such as UV photosensitivity and optical third-order nonlinearity are explored and utilized, showing the capability to modulate, switch, and trim. On the other hand, the physical structure of the waveguide is altered to include photonic crystals, or

hybrid integration with microspheres, showing wavelength filtering characteristics. Combining both these and other known properties has the potential to provide more functionality and material flexibility for a wide variety of applications.

1.2 Material overview

Tantalum pentoxide (Ta_2O_5) has been known since the 1970's as a promising material for optical antireflective and photovoltaic applications [13], and has attracted persistent attention and extensive research due to its diverse potential for applications in a wide variety of areas such as microelectronics, integrated optics, solar cells, chemical sensors, biological devices and so on. Due to its extensive range of novel properties, this section is devoted to a detailed introduction of the electronic, optical, and chemical properties of Ta_2O_5, which has led to many important applications and may lead to new applications.

1.2.1 Electronic properties

Ta_2O_5 was originally used in antireflection coatings for optical and photovoltaic applications. However, with the advanced progress in fabrication of electronic devices in the last decade, Ta_2O_5 regained much attention due to its integrability with silicon microcircuits, high dielectric constant (~35 has been reported [14]), high resistivity, low internal stress [15], achievable low leakage current, and high dielectric breakdown voltage which give it considerable advantages as an insulator over conventional silicon dioxide (SiO_2). These promising properties allow Ta_2O_5 to be considered as an alternative capacitor material to scale down the size of

electronic devices such as dynamic random access memory (DRAM) [16]. In addition to its use in capacitors, it has also been employed as a gate material for complementary metal-oxide-semiconductor devices [17]. This breakthrough significantly increases packing density, particularly in ultra-large-scale-integrated (ULSI) circuits [18] and thereby allows continuation of the scaling law (Moore's law) of present microelectronic circuit and communication techniques.

1.2.2 Optical properties

It has been shown that the refractive index and the extinction coefficient (the imaginary part of refractive index) of Ta_2O_5 are sensitive to the thin-film stoichiometry [19]. Stoichiometric Ta_2O_5 films have a refractive index n~2.2 and an almost zero extinction coefficient over a broad spectral range below the band gap energy (E_g~4.2 eV). For this reason, from an early stage, Ta_2O_5 has been used as a high refractive index material in multilayer interference filters [20]. It has been also used for antireflecting coatings in solar cells [21]. Due to the high index and low absorption characteristics in the telecommunications wavelength window, in particular, it has been suggested for use as an optical waveguide. Ta_2O_5 may be used on its own, or as a dopant in SiO_2, providing a widely adjustable refractive index by simply varying the SiO_2/Ta_2O_5 ratio [22]. Experimentally, Ta_2O_5 planar waveguides have been demonstrated to have a loss less than 0.9 dB/cm at wavelength λ=633 nm [23]. Dilute tantalum oxide silica waveguides with index difference of 5.6% have also been demonstrated with single-mode operation at a wavelength λ=1.3 μm with a propagation loss of 0.6 dB/cm [24].

As integrated optics has been modernized by the concept of photonic crystals, pure Ta_2O_5, being a high-index low-absorption material, renders itself a promising candidate. In order to make a complete photonic band gap, it has been suggested that a minimum refractive index contrast $\Delta n=2$ is required for a typical periodic lattice arrangement [25]. Ta_2O_5 not only fulfils this requirement but has excellent compatibility with existing Si/SiO_2 planar processing technology, enabling use of established processes in microelectronics.

While not having been exploited so directly, Ta_2O_5 has other potential advantages. From the UV-IR spectrum [26], the wide energy gap (E_g~4.2 eV) indicates that the material may have a very small two-photon absorption (TPA) [27] (when the operating wavelength corresponds to an energy less than half the band gap e.g. λ=1550 nm), which is considered to be a severe limiting factor for the attainable light-induced phase shift in most semiconductor materials. Additionally, considering the peak in the absorption spectrum at a wavelength of 260 nm [28], it is expected that there may be potential for UV irradiation below this wavelength to result in an index change. Experimentally, UV photosensitivity has been addressed at a signal wavelength λ=850 nm based on a side-polished fibre coupler [29]. A large negative index change Δn=-0.01 induced by UV was reported. Despite the uncertainty in the experimental accuracy and lack of information for Δn at λ=1550 nm, it does show the great potential for microstructuring devices utilizing the UV direct-write technique.

The extensive IR transparency in conjunction with the Raman spectrum [14] also implies a low phonon energy (<900 cm^{-1}) [14]. This gives a very important indication that the material itself is a good host for doping with suitable ions to realize optically pumped solid-state lasers and amplifiers, providing a possibility to realize a wide range of compact light sources. Towards this goal, in the past many attempts have been carried out to incorporate rare-earth elements into Ta_2O_5. Pr and Er doped Ta_2O_5 waveguides have been fabricated using ion-implantation. The Nd-containing crystal $NdTa_7O_{19}$ [30] and Nd-doped Ta_2O_5 [31] have also been reported using flux growth and thermal indiffusion techniques, respectively. However, only the absorption and fluorescence spectra but no lasing operation have ever been reported. Very recently, a Nd-doped Ta_2O_5 rib waveguide laser [32] has been demonstrated in our group, promising the great potential for other rare-earth elements to realize multi-wavelength light sources.

1.2.3 Chemical properties

Ta_2O_5 has been found to be highly resistant to many chemicals [13] and can be readily used as a protective coating for sensors [15] or as an etch mask [13]. Since sensors generally need to handle signals in different forms (e.g. pressure, temperature, pH value, etc) under a variety of situations, it is very important that the packaging and protective material can serve multiple purposes in the sensor systems. As a general rule, the desired properties include: good adhesion and high corrosion resistance, low residual stress to avoid the reduction of sensitivity, effectiveness as a diffusion barrier, and good transparency for visual observation.

Ta_2O_5 has been shown to be chemically very inert [33], particularly in alkaline environments, which is very unusual for most semiconductor materials. The etch rate in aqueous KOH with pH 11 at 140℃ has been reported to be lower than 8×10^{-4}nm/h [15], providing extremely large selectivity over silicon, and has been suggested for sensor purposes. This corrosion-resistant film has been utilized in a electrolyte-insulator-semiconductor configuration [34] to provide a wide pH response range. When use as an etch mask, this property can be useful especially for the fabrication of microelectromechanical systems (MEMs).

Additionally, Ta_2O_5 has been widely applied in electrochromic (EC) devices due to its good conductivity for protons and ions. Electrochromism refers to the color change of the film in response to an applied voltage/current. Usually, a electrochromic cell is composed of an ion storage layer, an ion electrolyte, and an electrochromic layer, which are sandwiched between two transparent electrodes. Small ions such as H^+ and alkali ions which can be intercalated electrochemically, subject to the applied potential, are able to move back and forth between the ion storage layer and the electrochromic layer, causing a reversible color change. Numerous applications such as smart windows [35], electroluminescent displays [35], and batteries [36] have been suggested.

1.2.4 Other properties

Most of the properties reported so far are based on the amorphous phase of Ta_2O_5. The crystalline phase of Ta_2O_5 has grain boundaries that may cause a high leakage

current. Optically, the grain boundaries cause severe volume scattering, resulting in a high loss film. Chemically, the grain boundaries cause a higher pinhole density which may degrade the corrosion resistance. Nevertheless, it has been shown that piezoelectric properties exist in crystalline Ta_2O_5 films [37], and the effect has been reported to be comparable to the well-known ZnO films [38]. Piezoelectricity is a stress induced polarization effect. When a material is subjected to a stress, the polarization (corresponding to an induced electric field) of the material changes in response to the applied force. Conversely, a piezoelectric material undergoes a shape change in response to an applied electric field. As a consequence, surface acoustic waves (SAWs) can be excited electrically. This opens up various applications of Ta_2O_5 including transducers, high-frequency signal processing filters, and delay lines. In addition, based on the interaction between light and SAW, piezoelectric materials have important applications in optical switching devices such as optical deflectors and modulators. Crystalline Ta_2O_5 can be obtained when thin films are grown or annealed at an elevated temperature (>650℃).

1.3 Thesis outline

In the previous section, the material properties of Ta_2O_5 have been briefly reviewed. This thesis focuses on the optical properties of Ta_2O_5 and puts emphasis on assessing largely unexplored properties and their application in waveguides. Chapter 2 introduces some basic properties of Ta_2O_5 rib waveguides. It begins by describing a repeatable fabrication process for Ta_2O_5 rib waveguides established in this work. Single mode cut-off dimensions were determined for rib waveguides with

a range of widths and etch depths. The results are compared with theory, leading to reliable guidelines for designing waveguides. Modal field properties are examined for both polarizations and the coupling loss with a standard telecommunication fibre was calculated based on the modal overlap integral. The result gives a clear picture of the modal field evolution in relation to the corresponding waveguide geometry, forming the cornerstone of the waveguide design process for the remaining chapters. Finally, the loss of the waveguides is presented, and the loss mechanism was identified evidenced by the polarization dependent loss (PDL). This chapter concludes by proposing some routes that may lead to a further reduction of propagation and coupling losses in practical devices.

Chapter 3 starts to address the material properties which have not yet been widely explored. UV photosensitivity was assessed using a Ta_2O_5 rib waveguide based Mach-Zehnder interferometer configuration. The design considerations and the fabrication procedures are based upon the guidelines built up in Chapter 2. Through the UV induced differential phase shift, the output signal cycles through several on-off-on states and is monitored in real time. The associated refractive index change is then calculated from the modulation characteristics of the output power. The sign of the refractive index change was further ascertained by monitoring the splitting ratio of a partially irradiated Ta_2O_5 Y-junction. The chapter ends by comparing the magnitude of the UV-induced index change with that of conventional Ge-doped silica glasses and also pointing out the potential applications.

Chapter 4 is devoted to exploring the third-order optical nonlinearity ($\chi^{(3)}$ or n_2) of a Ta_2O_5 rib waveguide, which to the knowledge of the author, has never been determined. A number of techniques used to measure n_2 are briefly reviewed in a detailed introduction, particularly devoted to self-phase modulation (SPM), which is the technique employed in this study. The chapter then details the laser systems, experimental setup, and sample structures used in the SPM measurement. The observed spectra under different peak-coupled power are presented and the estimation of n_2 based on a simplified theory which ignores the impact of group velocity dispersion (GVD) is described. To justify the validity and reliability of the estimated n_2, the second part of the chapter describes the GVD measurement based on a femtosecond time-of-flight Kerr-shutter configuration. The wavelength region where the GVD has a negligible impact upon the determination of n_2 is also drawn out. The chapter concludes by discussing potential applications for optical switching devices.

Chapter 5 starts to broaden the functionality of Ta_2O_5 waveguides by means of geometrically tailoring the structures. Hybrid integration was demonstrated by combining a self-assembled microsphere grating with a Ta_2O_5 rib waveguide. The optical coupling in this newly demonstrated composite structure was tested by carrying out fibre-coupled transmittance measurements. The optical coupling, evidenced by the observed transmission drop was described by grating theory. An simplified theory was used to explain the results and was found to agree qualitatively with the measured spectrum. Coupling strength adjustment by varying

the refractive index of the cladding medium was also demonstrated. The chapter concludes with a brief discussion of the applications of this type of structure, and focuses on issues which may provide a route leading to a larger-scale, less disordered structure.

Chapter 6 gives another example of added functionality achieved by altering the physical structure of the waveguide using photonic crystals (PCs). First, numerical schemes (plane wave expansion (PWE) and transfer matrix method (TMM)) for simulating the band structures and the transmission spectrum of the PCs are briefly introduced and tested. The fabrication of an embedded photonic crystal within a Ta_2O_5 rib waveguide is then described. Results of the transmission spectrum shows band-gap like transmission drops. The comparison between the various theoretical models and of theory with experiment are made and the discrepancies are listed. This chapter concludes by discussing the discrepancies and provides directions for improvement.

Chap 7 gives a comprehensive summary of each individual work drawn out from the conclusions of each chapter. Future work proposed is included in the discussions and puts emphasis on possible routes to improve the device fabrication.

References

[1] S. E. Miller, "Integrated Optics: An Introduction," The Bell System Technical Journal, vol. **48**, 2059 (1969).

[2] H. Kogelnik and C. V. Shank, Appl. Phys. Lett., vol. **18**, 152 (1971).

[3] D. R. Scifres, R. D. Burnham, and W. Streifer, VIII International Quantum Electronics Conference, R1, (1974).

[4] A. Agarwal, L. Liao, J. Foresi, M. Black, X. Duan, and L. Kimerling, J. Appl. Phys. Vol. **80**, 6120 (1996).

[5] A. Rickman, G. T. Reed, B. L. Weiss, and F. Namavar, IEEE Photon. Technol. Lett., vol. **4**, 633 (1992).

[6] DWDM SFP Product Brief [Online]. 2003 [Accessed 13th Feb 2004]. Available from World Wide Web: <http://www.luminentoic.com/dwdm>

[7] Optical Amplifier Products [Online]. 2003 [Accessed 13th Feb 2004]. Available from World Wide Web: <http://www.teemphotonics.com/documents/product/>

[8] Voltage-Controlled Optical Filters [Online]. 2003 [Accessed 13th Feb 2004] Available from World Wide Web: <http://www.jdsu.com/index/>

[9] High-performance large-scale 16x16 optical matrix switch module [Online]. 2002 [Accessed 13th Feb 2004]. Available from World Wide Web: <http://www.phlab.ecl.ntt.co.jp/eng/theme/2002/e2002a_08_4.pdf>

[10] A. Mekis, J. C. Chen, I. Kurland, S. Fan, P. R. Villeneuve, and J. D. Joannopoulos, Phys. Rev. Lett., vol. **77**, 3787 (1996).

[11] T. F. Krauss and R. M. De La Rue, Prog. Quantum Electron., vol. **23**, 51 (1999).

[12] V. Mizrahi, K. W. Delong, G. I. Stegeman, M. A. Saifi, and M. J. Andrejco, Opt. Lett., vol. **14**, 1140 (1989).

[13] C. Chaneliere, J. L. Autran, R. A. B. Devine, and B. Balland, Mater. Sci. Eng., vol. **22**, 269 (1998).

[14] P. S. Dobal, R. S. Katiyar, Y. Jiang, R. Guo, and A. S. Bhalla, J. Raman Spec. vol. **31**, 1061 (2000).

[15] C. Christensen, R. de Reus, and S. Bouwstra, J. Micromech. Microeng., vol. **9**, 113 (1999).

[16] N. V. Nguyen, C. A. Richter, Y. J. Cho, G. B. Alers, and L. A. Stirling, Appl. Phys. Lett., vol. **77**, 3012 (2000).

[17] G. B. Alers, D. J. Werder, Y. Chabal, H. C. Lu, E. P. Gusev, E. Garfunkel, T. Gustafsson, and R. S. Urdahl, Appl. Phys. Lett. vol. **73**, 1517 (1998).

[18] E. Atansassova, T. Dimitrova, and J. Koprinarova, Appl. Surf. Sci., vol. **84**, 193 (1995).

[19] M. Cevro and G. Carter, Opt. Eng., vol. **34**, 603 (1995).

[20] A.J. Waldorf, J. A. Dobrowolski, B. T. Sullivan, and L. M. Plante, Appl. Opt., vol. **32**, 5583 (1993).

[21] F. Rubio, J. M. Albella, J. Denis, and J. M. Martinez-Duart, J. Vac. Sci. Technol., vol. **21**, 1043 (1982).

[22] M. Kobayashi and H. Terui, Appl. Opt., vol. **22**, 3121 (1983).

[23] D. H. Hensler, J. D. Cuthbert, R. J. Martin, and P. K. Tien, Appl. Opt., vol. **10**, 1037 (1971).

[24] H. Takahashi, S. Suzuki, and I. Nishi, J. Lightwave Technol., vol. **12**, 989

(1994).

[25] V. Berger, Opt. Mat., vol. **11**, 131 (1999).

[26] E. Franke, C. L. Trimble, M. J. Devries, J. A. Woollam, M. Schubert, and F. Frost, J. Appl. Phys., vol. **88**, 5166 (2000).

[27] K. W. Delong and G. I. Stegeman, Appl. Phys. Lett., vol. **57**, 2063 (1990).

[28] N. V. Nguyen, C. A. Richter, Y. J. Cho, G. B. Alers, and L. A. Stirling, Appl. Phys. Lett., vol. **77**, 3012 (2000).

[29] M. P. Roe, M. Hempstead, J. –L. Archambault, P. St. J. Russell, and L. Dong, Proc. CLEO Europe'94, 67 (1994).

[30] E. Cavalli, L. I. Leonyuk, and N. I. Leonyuk, J. Crystal Growth, vol. **224**, 67 (2001).

[31] D. A. Sager, V. Apostolopoulos, and J. S.Wilkinson, J. Ceramic Soc. Amer., vol. **85**, 2581 (2002).

[32] B. Unal, D. P. Shepherd, C. Y. Tai, M. C. Netti, J. S. Wilkinson, and G. J. Parker, to be submitted to Appl. Phys. Lett.

[33] U. Gramberg, M. Renner, and H. Diekmann, Mater. Corrosion, vol. **46**, (1995).

[34] S. Yoshida, N. Hara, and K. Sugimoto, J. Electrochem. Soc., vol. **151**, H53 (2004).

[35] E. B. Franke, C. L. Trimble, M. Schubert, J. A. Woollam, and J. S. Hale, Appl. Phys. Lett., vol. **77**, 930 (2000).

[36] M. S. Mattsson and G. A. Niklasson, J. Appl. Phys., vol. **85**, (1999).

[37] Y. Nakagawa and T. Okada, J. Appl. Phys., vol. 68, 556 (1990).

[38] Y. Nakagawa and Y. Gomi, Appl. Phys. Lett., vol. 46, 139 (1984).

Chapter 2 Rib waveguide design, fabrication and characterization

2.1 Introduction

Rib waveguides, with step discontinuities in the transverse direction of the core, are attractive structures for planar lightwave circuits. The choice of horizontal and vertical index steps are flexible and easily controlled to meet a particular requirement. In addition, the modal field distribution and propagation constant of the guided mode can be accurately controlled by tailoring the physical geometry in combination with the refractive indices of the materials employed. Moreover, it has been suggested that single mode operation with an "oversized" dimension with respect to the stripe type waveguide is feasible regardless of the refractive index contrast due to its weaker lateral confinement [1]. Experimentally, oversized rib waveguides have been demonstrated in many material systems including GeSi-Si [2], silicon-on-insulator (SOI) [2-5], and polymers [6]. This not only solves the long-standing fibre-to-chip coupling problem particularly in high index contrast material systems, but greatly improves the stringent alignment tolerance in waveguide characterization. In this chapter, these properties are experimentally addressed using Ta_2O_5 rib waveguides designed for a wavelength of λ=1.55 μm. Ideally, to minimize the coupling loss between the fibre and waveguides, the modal field distributions have to be matched. For the standard telecommunication fibre (Corning© SMF-28), the modal field diameter (MFD) is 10.4±0.8 μm at λ=1550 nm [7]. This requires a waveguide cross-section to be made comparable to that of the fibre. Practically, the uniformity of the film thickness across a Si wafer substrate

degraded with increasing deposition thickness, in particularly, for thick films. In order to achieve a good compromise between film uniformity and the coupling efficiency using current fabrication techniques, waveguides of thickness 1 μm are considered. In section 2.2, the fabrication of Ta_2O_5 rib waveguides is described. In section 2.3, the single mode cut-off dimension (SMCD), defined as the biggest size of waveguide core for single mode operation, was determined based on the experimental observation of the number of modes from the range of fabricated waveguides. In section 2.4, waveguide mode properties are discussed in relation to the physical geometries. Predicted coupling efficiency with a standard telecommunication fibre was calculated based on the modal field overlap integral. In section 2.5, the measurements of the propagation loss based on the cut-back technique is presented. In section 2.6, the fiber-chip-fiber loss is discussed in terms of basic measurements and future applications. Possible routes are suggested for the improvement of the propagation loss and coupling loss. In section 2.7, a brief summary is given.

2.2 Fabrication

Ta_2O_5 rib waveguides were fabricated sequentially by sputtering, standard photolithography, and Ar ion beam milling. Figure 2.2.1 shows the fabrication procedure. A 1 μm thick layer of Ta_2O_5 was first sputtered from a Ta_2O_5 target onto a Si wafer with 2μm SiO_2 buffer layer, with the substrate temperature held at 250℃ and RF power setting at 400 W. During the sputtering process, the chamber pressure was kept at 35 mTorr with gas flow rate set for Ar and O_2 equal to 16 and 6 sccm,

respectively. The thickness of the SiO_2 buffer provides sufficient isolation to prevent optical power leaking out into the underlying Si substrate. Waveguides with different widths were created following a standard photolithographic process. First, a layer of 2 μm photoresist (MicroChem SU8-2) was spin-coated (2500 rpm, 60 sec) onto the wafer and soft-baked at 90℃ for 30 minutes. The film was then exposed to U.V. light under a mask with openings ranging from 1 μm to 10 μm. The light source is a 350 W super pressure mercury short-arc lamp providing spectral lines centered around λ=365 nm. The photoresist was fully cross-linked by a 50 second exposure followed by 30 minutes post-exposure baking at 90℃. The film was then developed for 2 minutes resulting in photoresist stripes with nominal widths ranging from 1 μm to 10 μm.

Ar ion beam milling was subsequently used to transfer the pattern into the Ta_2O_5 waveguide layer. An acceleration voltage of 500 Volts and current of 125 mA constructs a plasma which bombards the sample. Rib waveguides with different etch depths were achieved by using different etching times. Fig. 2.2.2 shows the etch depth, measured by an Alfastep surface profiler, as a function of the etching time. It is found that Ta_2O_5 has a linear etch rate of 33 nm/min, under these etching conditions.

In order to release the stress and improve the film uniformity and optical properties, the milled waveguides were cleaned and annealed at 500℃ for 72 hours with ramp rate of 2℃/min to avoid rapid thermal shock.

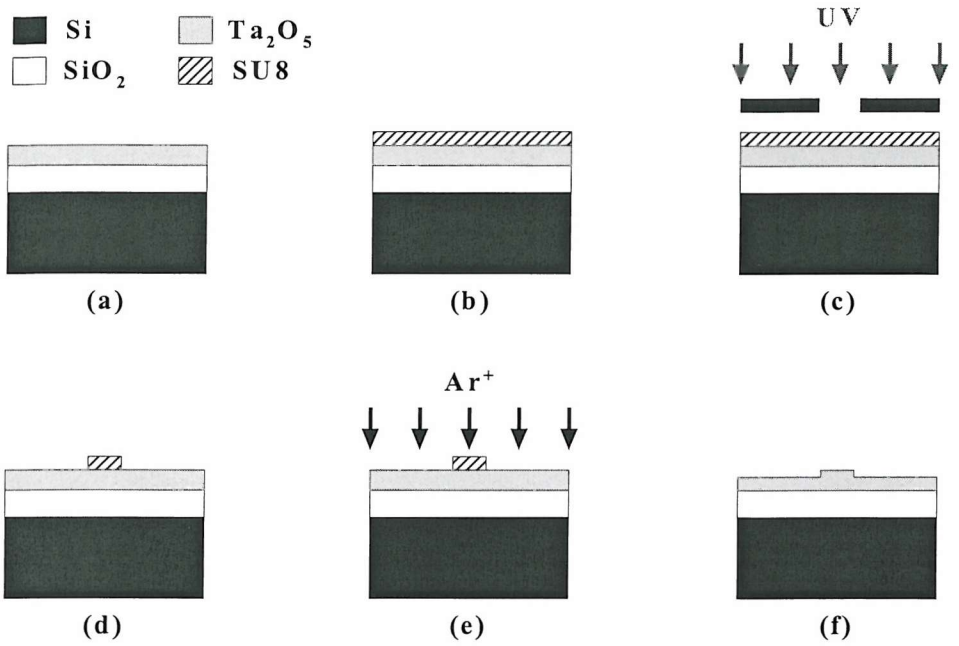

Fig. 2.2.1 Rib waveguide fabrication sequence: (a) sputtering of Ta_2O_5 (1 μm). (b) spin-coating of SU8 (2 μm). (c) UV exposure (d) develop photoresist (e) pattern transfer by ion beam milling (f) clean and cleave.

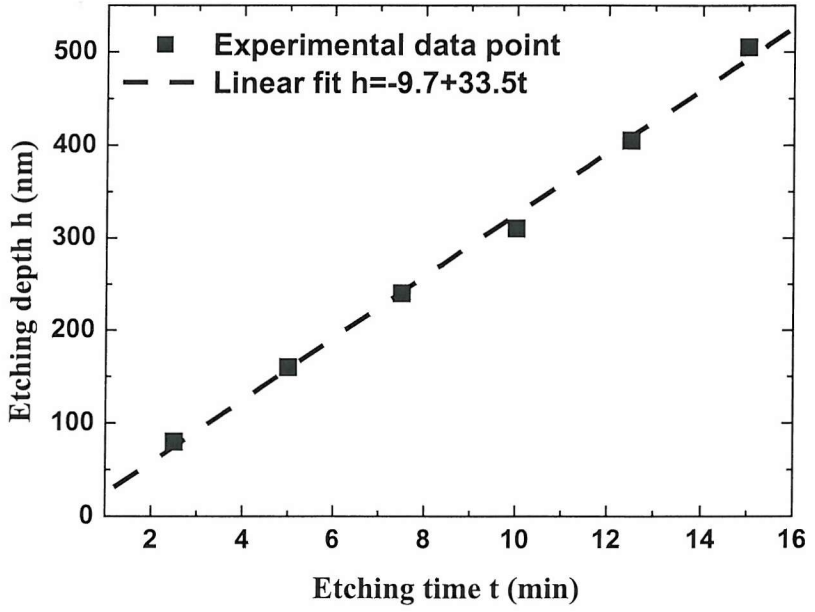

Fig. 2.2.2 Etching depth as a function of etch time.

2.3 Single mode cutoff dimension (SMCD)

One of the most interesting properties of rib waveguide structures is the potential to maintain single-mode propagation with a large cross-section core, regardless of the index contrast between core and cladding layers. Figure 2.3.1 schematically shows the transverse geometric structure of a rib waveguide. The waveguide core consists of three parts: the central ridge region and two slab sections extended on either side. Compared to stripe waveguides (an extreme case of the rib waveguide when the thickness of the slab sections is zero), the optical field is less confined in the lateral direction since the effective refractive index contrast between the central guide region and the lateral slab is reduced. Based on this property, higher order modes in the vertical direction of the central ridge region will be cut-off due to the coupling to slab modes in the slab section. As the effective refractive index of the fundamental slab mode becomes larger than the effective index of the higher order mode in the central ridge region, higher-order modes become leaky due to the coupling to the slab mode, which ensures single mode operation.

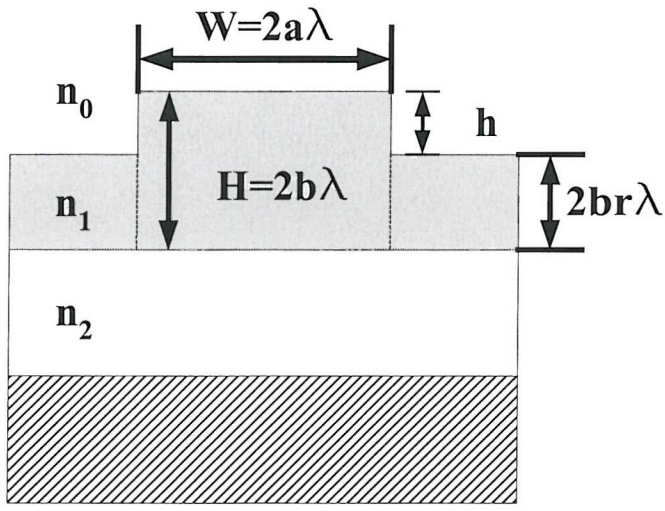

Fig. 2.3.1 Cross-sectional view of the rib waveguide

According to Petermann's theory [2], this condition occurs when the etching depth is less than half of the rib waveguide height ($r \geq 0.5$) and the aspect ratio a/b fulfils the following formula:

$$\frac{W}{H} = \frac{2a\lambda}{2b\lambda} = \frac{a}{b} \leq \left(\frac{q+4\pi b}{4\pi b}\right) \frac{1+0.3\sqrt{\left(\frac{q+4\pi b}{q+4\pi rb}\right)^2 - 1}}{\sqrt{\left(\frac{q+4\pi b}{q+4\pi rb}\right)^2 - 1}} \tag{2.1}$$

where q represents the geometric parameter defined by:

$$q = \frac{\gamma_0}{\sqrt{n_1^2 - n_0^2}} + \frac{\gamma_2}{\sqrt{n_1^2 - n_2^2}} \tag{2.2}$$

with $\gamma_0 = \gamma_2 = 1$ for the TE mode and $\gamma_0 = \left(\frac{n_0}{n_1}\right)^2$, $\gamma_2 = \left(\frac{n_2}{n_1}\right)^2$ for the TM mode, respectively. According to equation (2.1), a maximum waveguide width for single mode operation can be determined.

Table I shows the range of waveguides fabricated and the corresponding number of modes at λ=1.55 μm. To count the number of modes in each waveguide, light from a pigtailed DFB laser operating at λ=1.55 μm was end-fire launched into the waveguide. In order to excite any possible mode, the launching fibre was scanned across the waveguide facet. An infrared camera monitors the modal intensity profile in real time enabling one to determine the mode order.

For all of the fabricated waveguides listed in Table I, only one mode was found in the vertical direction. In addition, it is found that the SMCD increases with reduced

etch depth. In the case of a 1 μm thick stripe waveguide (etched throughout the Ta_2O_5), the SMCD has the smallest value of 1×1 μm^2. As the etch depth is decreased to h=80 nm, single mode operation can be realized in a 3 μm wide rib waveguide at 1550 nm. This dimension is well within the limitation of conventional photolithography and is three times bigger than that of the stripe waveguide, offering a significant improvement in the coupling efficiency to fibre.

Table I Modal properties of the fabricated Ta_2O_5 rib waveguides

width (μm)	etching depth (nm)						
	80	160	240	310	405	480	1000
W=1	*	*	*	*	*	*	*
W=2	*	*	*	#	#	#	#
W=3	*	#	#	#	#	#	#
W=4	#	#	#	#	#	#	#

* TE_{00} and TM_{00} mode only, # multimode

Figure 2.3.2 shows the theoretical single-mode boundary line and the experimentally observed single mode waveguides formed in a 1 μm thick Ta_2O_5 film. It is found that the experimental data points lie within the region where single mode operation is predicted. In addition, the deviation of the refractive index of Ta_2O_5 makes only very little difference, as shown in the figure. This result demonstrates the validity of equation (2.1) and shows its potential for use as a guideline for waveguide design.

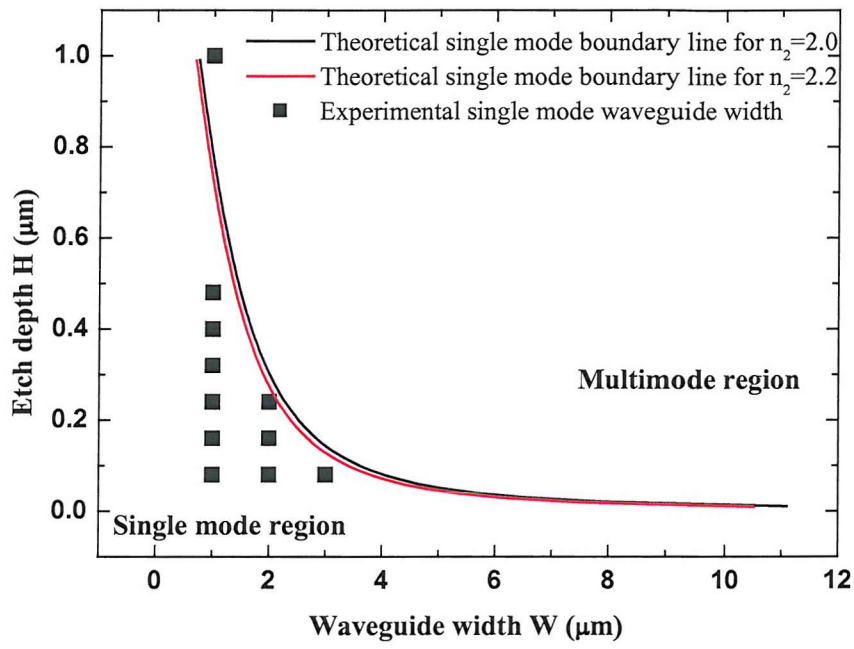

Fig. 2.3.2 Experimental single mode waveguide dimension (square symbol) and theoretical single mode boundary line (dashed line). The refractive indices used for the simulation here are: n_0=1, n_2=1.46, and n_1=2 and 2.2.

2.4 Mode properties and coupling efficiency

To evaluate modal field profiles, the fabricated rib waveguides were excited using a DFB laser operating at λ=1.55 μm with a pigtailed single mode polarization maintaining fibre. The fibre was butt coupled to the cleaved facet of waveguides and the light out of waveguides was collected using a 40× microscope objective. The light was subsequently focused through a pinhole onto an infrared camera. The experimental setup is shown schematically in Fig. 2.4.1. A collection of some typical modal intensity profiles recorded using the CCD camera was shown in Fig. 2.4.2.

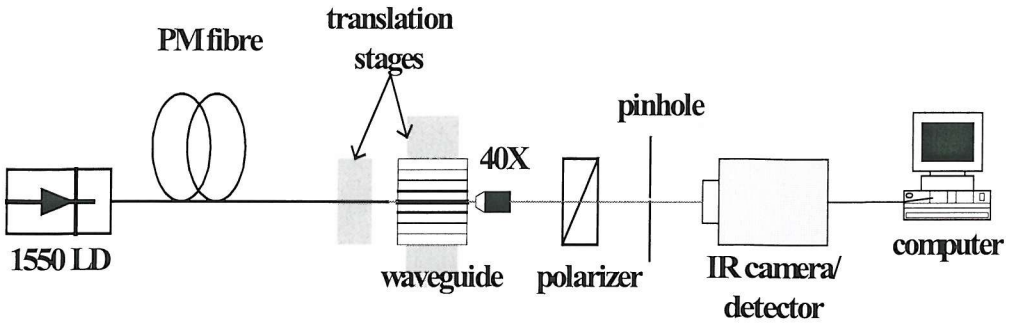

Fig. 2.4.1 Experimental arrangement for waveguide characterization.

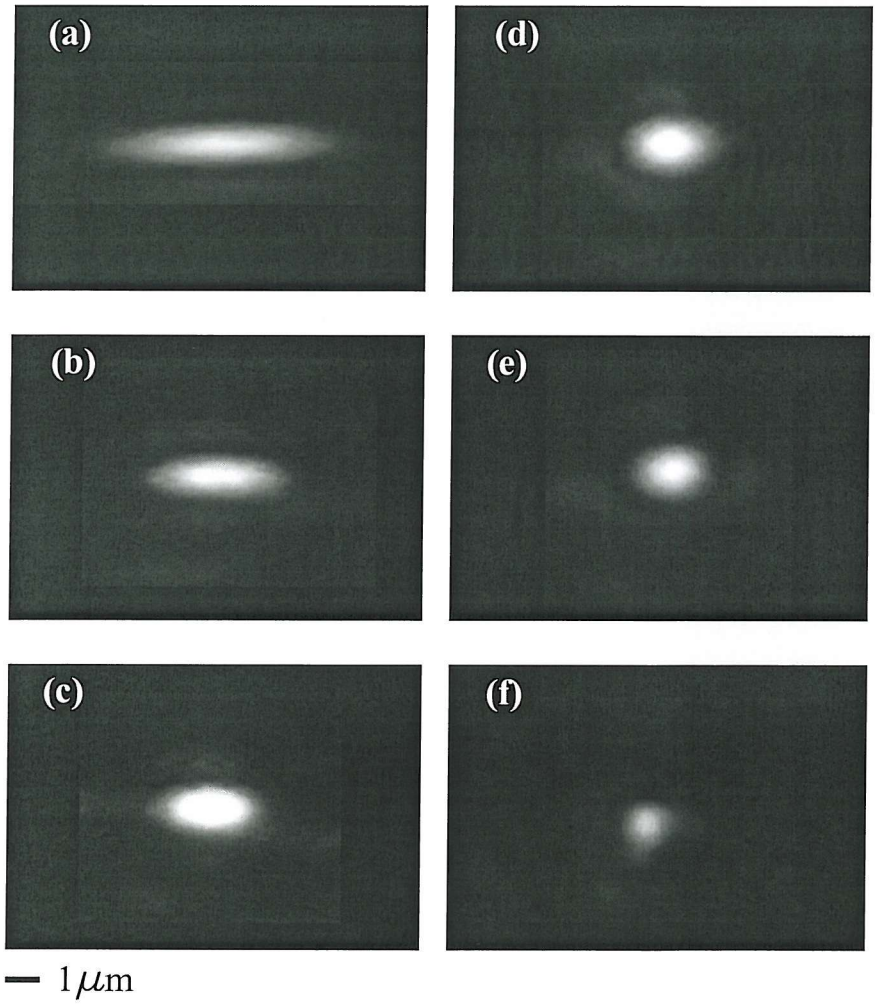

Fig. 2.4.2 Some typical modal intensity profiles (TE mode) recorded by the CCD camera. (a)-(e) Rib waveguides with a width W=1 μm, height H=1 μm, and etch depth h=80, 160, 240, 310, and 405 nm, repectively. (f) Stripe waveguide with a width W=1 μm and height H= 1 μm.

The recorded modal intensity images were digitized with a spatial resolution of ~ 0.1 μm per pixel along both horizontal and vertical axis. The modal field width and height were defined as the $1/e^2$ of the normalized intensity width and height, respectively. Figure 2.4.3 and Fig. 2.4.4 shows the TE and TM mode intensity distribution along the horizontal axis for rib waveguides (W=1 μm, H=1μm) with etch depth h ranging from 80 nm to 405 nm, respectively. For both polarizations, the modal field widths decrease with increasing etch depth indicating a stronger field confinement due to the increased effective refractive index contrast in the lateral direction. Comparing the TE and TM modes, it is found that the TE modal field width is larger than that of the TM one by a factor of ~1.5 for the same waveguide geometry. This result shows that the TE mode is less confined laterally while the TM mode appears to be better confined in the central part of the rib waveguide. As a result, it is expected that the TE mode is more sensitive to the sidewall roughness while the TM mode is more sensitive to the interface ($Air/Ta_2O_5/SiO_2$) imperfections.

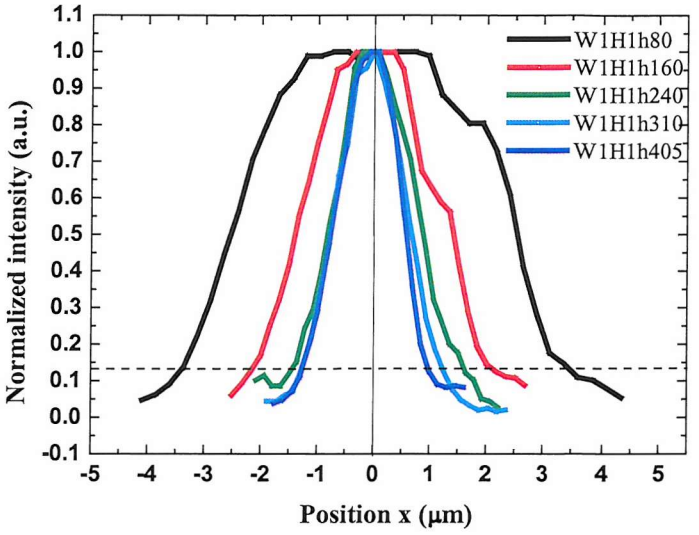

Fig. 2.4.3 The TE Modal intensity profiles in the horizontal direction for waveguides with etch depth range from 80 nm to 405 nm.

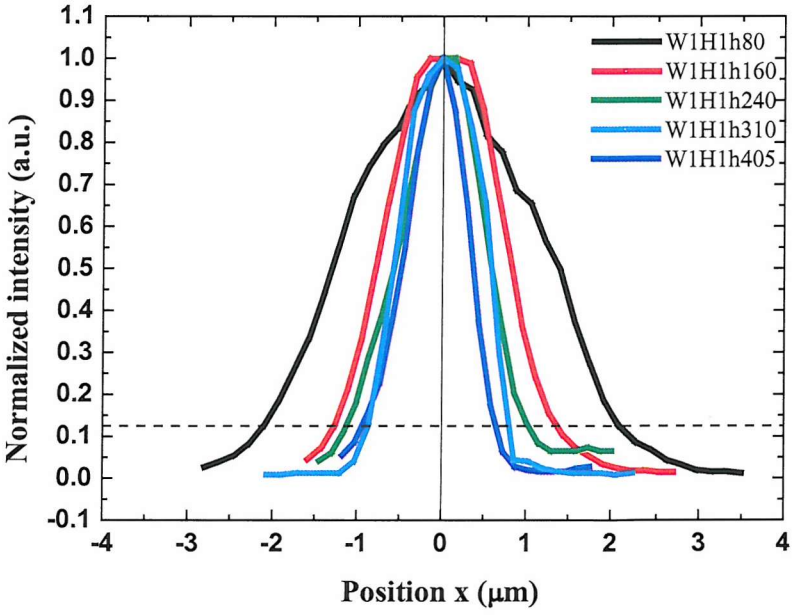

Fig. 2.4.4 The TM Modal intensity profiles in the horizontal direction for waveguides with etch depth range from 80 nm to 405 nm.

The modal intensity distributions along the vertical axis were plotted in Fig. 2.4.5 and Fig. 2.4.6 for the TE and TM modes, respectively. It is found that the modal field heights for both polarizations first decrease with increased etch depth, and increase as the etch depth rises above 240 nm. This effect is due to the growing effective refractive index contrast in the lateral direction. When the etch depth is small, the effective refractive index of the rib mode is close to that of the slab mode. Therefore, the field is drawn out due to the strong coupling to the slab mode. As the etch depth is increased, the larger effective refractive index difference weakens this coupling, and the optical field is able to be confined in the central rib region rather than coupling to the slab mode. This causes the field to be more confined in the central rib region and more power are distributed in the SiO_2 buffer layer, resulting in the increase of the modal field height.

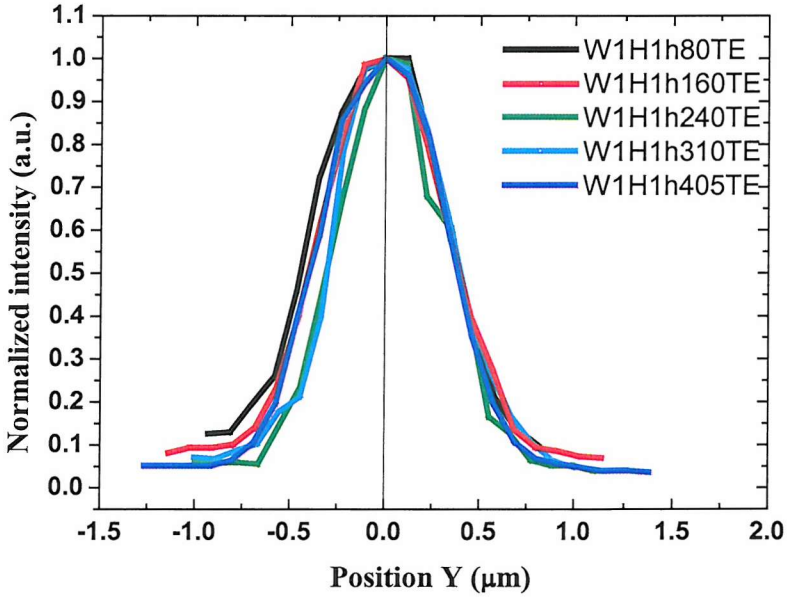

Fig. 2.4.5 The TE Modal intensity profiles in the vertical direction for waveguides with etch depth range from 80 nm to 405 nm.

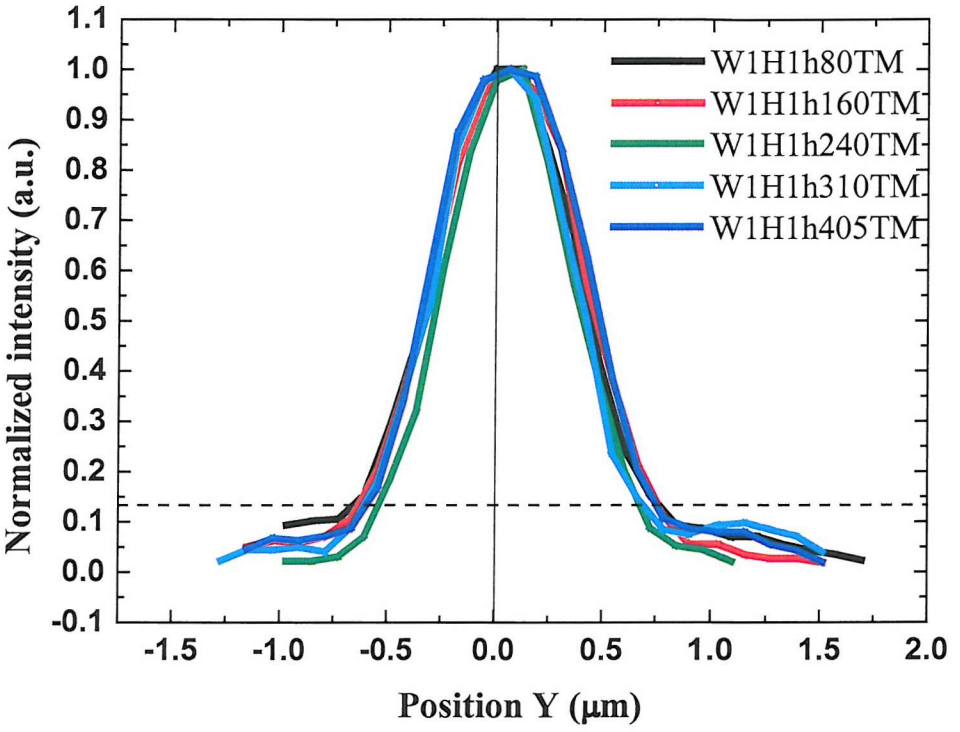

Fig. 2.4.6 The TM Modal intensity profiles in the vertical direction for waveguides with etching depth range from 80 nm to 405 nm.

In order to compare experimental results with theory, mode profiles for the range of fabricated waveguides were calculated using the commercial software BEAMPROP^{TM} based on the beam propagation method (BPM) [8]. Figure 2.4.7 and 2.4.8 show the theoretical fundamental mode width as a function of waveguide width for the TE and TM mode, respectively. The experimental data points for the single mode waveguides are plotted on this figure and it is found that experimental values for the fabricated single mode waveguides qualitatively agree with theory. From these diagrams, it is found that rib waveguides with a shallow etch depth not

only have a larger modal spot size but also have a larger single mode cutoff dimension.

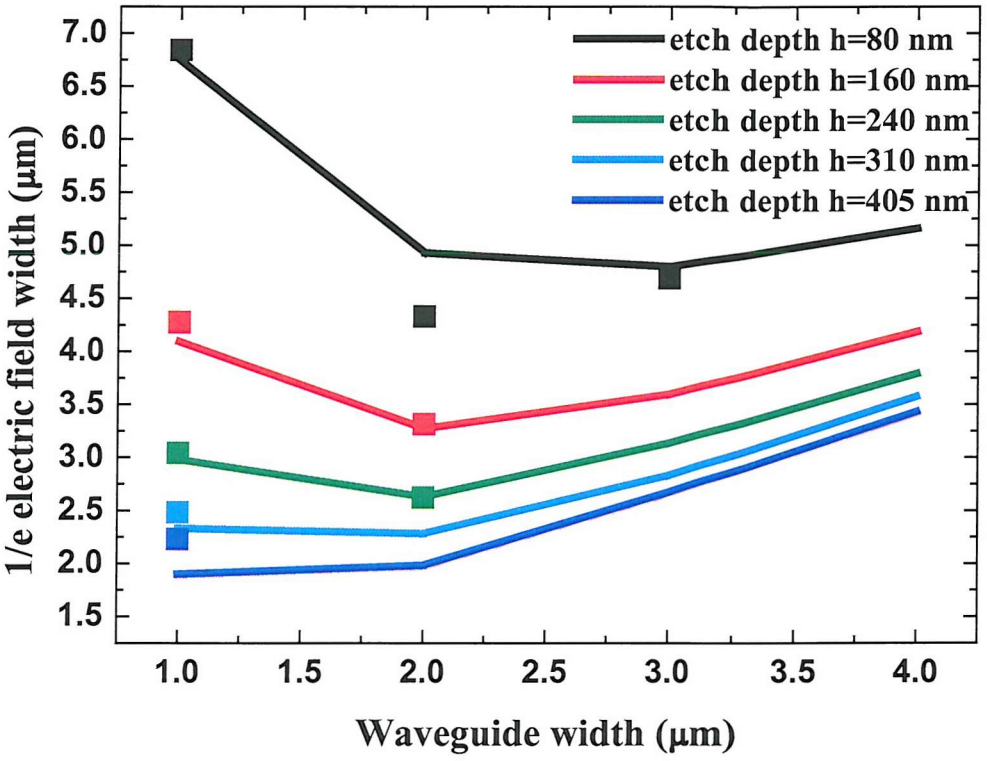

Fig. 2.4.7 The TE mode field width for waveguides with various etch depths. Solid lines are theoretical predictions, and solid square denotes experimental values.

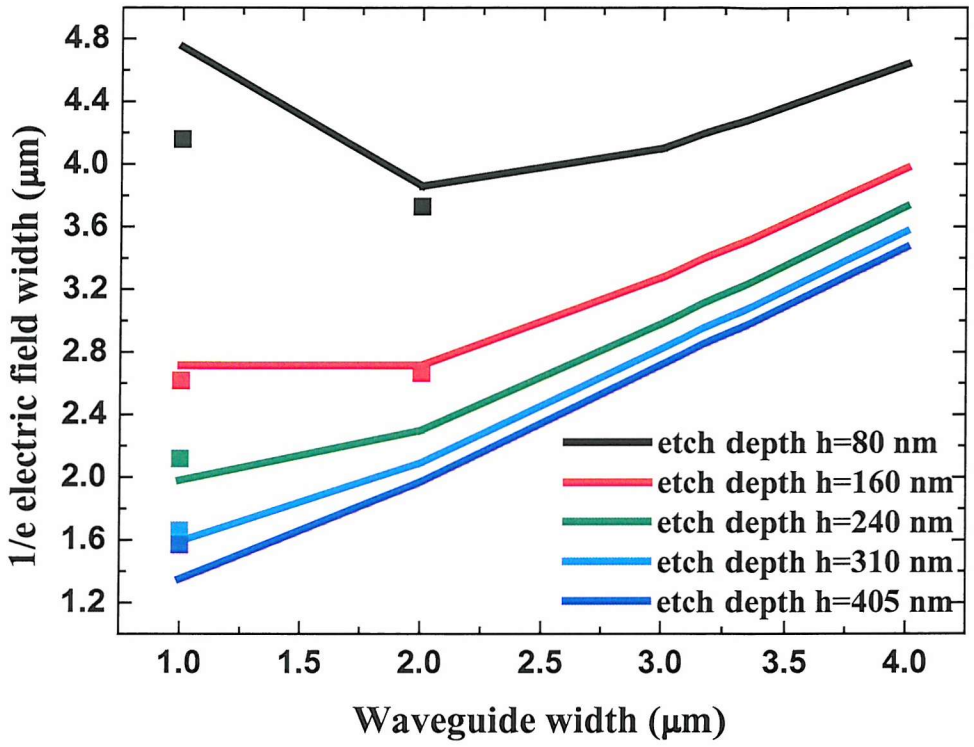

Fig. 2.4.8 The TM mode field width for waveguides with various etch depths. Solid lines are theoretical predictions, and solid square denotes experimental values.

To illustrate the predicted effect of the modal intensity profile on coupling efficiency with a standard telecommunication fibre (Corning® SMF-28™, 9/125, 0.13 NA), the single mode rib waveguide with the largest modal field size (W1H1h80TE) was chosen for comparison with single mode stripe waveguide with the same film thickness. The fibre-to-waveguide coupling coefficient is defined by the following overlap integral [9]:

$$\eta=\left|\iint \Psi_1(x,y)\Psi_2(x,y)dxdy\right|^2 \qquad (2.3)$$

where Ψ_1 and ψ_2 denotes the normalized modal field for the fibre and the waveguide, respectively. These images are loaded into EasyAccess, a commercial software which discretizes images into 2D arrays of numbers and allows translation and rotation to find the best match between the two images. The similarity between the two optical modes was evaluated by computing a normalized correlation score, which is the 2D numerical integral (eqn. 2.3) over an appropriate area covering the modal profile patterns. The coupling loss in decibels due to mode mismatch at the interface can be calculated as:

$$L_c = -10 \cdot \log \eta \tag{2.4}$$

Figure 2.4.9 shows the mode images for the selected rib waveguide and stripe waveguide. These images are first digitized into 2D arrays, and then numerically integrated following equation (2.3). The coupling loss, obtaining from equation (2.4), yields a value of 6 dB and 11 dB for rib and strip waveguides, respectively. For waveguides with the same thickness, the coupling efficiency η was enhanced by a factor of 3.4.

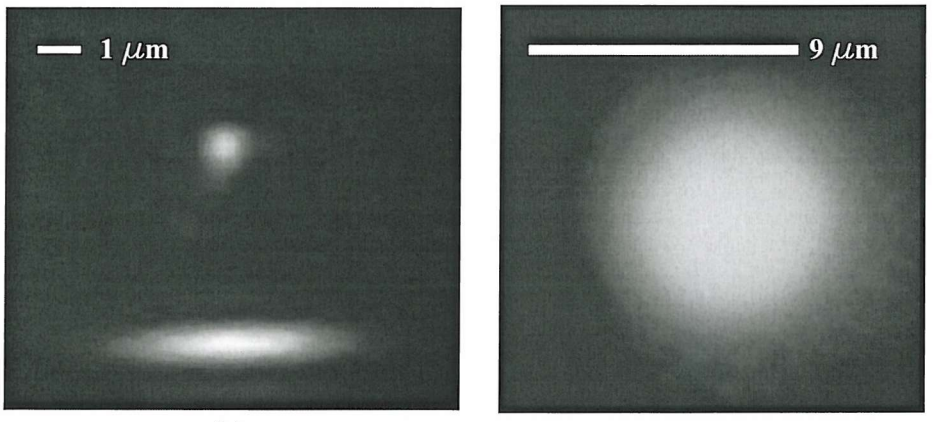

Fig. 2.4.9 Recorded modal field profiles for (a) stripe waveguide (upper) and rib waveguide. (b) standard telecommunication fibre.

2.5 Waveguide loss

The attenuation coefficient of a waveguide is determined by measuring the optical power decay along the waveguide. Assuming that the coupled optical power has an exponential decay through the waveguide, the output power P_{out} can be related to the input power P_{in} by the following equation:

$$P_{out} = \eta P_{in} \exp(-\alpha L) \tag{2.5}$$

where η is the coupling efficiency, α is the attenuation coefficient, and L is the length of the waveguide. Generally, the propagation loss L_p is expressed in units of decibels per centimeter (dB/cm) and can be obtained from equation (2.5) as follows:

$$L_p = \frac{10}{L}\log\frac{\eta P_{in}}{P_{out}} \approx 4.34\left(\frac{1}{L}\ln\frac{\eta P_{in}}{P_{out}}\right) \approx 4.34\alpha \tag{2.6}$$

In this study, the propagation loss of the fabricated waveguide was measured by the cut-back technique. Light from a fibre pigtailed DFB laser operating at λ=1.55 μm was end-fire coupled into the waveguide under investigation. The light out of the waveguide was measured using a power meter. The waveguides were cleaved successively into chips with different lengths and the output power throughput different waveguide lengths were measured. Figure 2.5.1 shows the insertion loss, defined as the logarithm of the input to output power ratio, as a function of the waveguide length for the rib waveguide (W1H1h80TE) and stripe waveguide, respectively. From the plot, the propagation loss L_p is obtained from the slope of the plot and the coupling loss L_c is obtained from the intercept on the Y axis. This can be understood by rearrangement of equation (2.6) in the following way:

$$10\log\frac{P_{in}}{P_{out}} = -10\log\eta + L_p L \tag{2.7}$$

where the first term on the right-hand-side of the equation is exactly the formula in equation (2.4) which represents the coupling loss, and L_p in the second term is the slope.

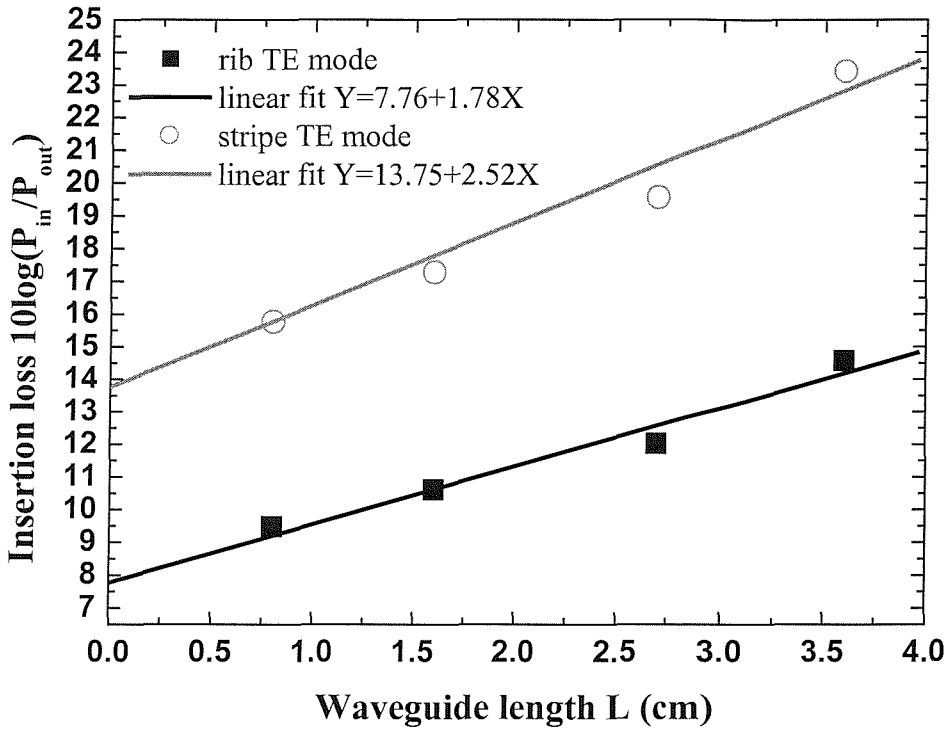

Fig. 2.5.1 Insertion loss of the TE mode as a function of waveguide length for the rib waveguide (W1H1h80) and the stripe waveguide (h=1 μm).

The experimental data shows that the propagation loss is 1.78 dB/cm and 2.52 dB/cm for the shallow etched rib waveguide and the strip waveguide, respectively. This result shows that the propagation loss increases as the etching depth is increased, suggesting that the excess loss is from the sidewall roughness

incorporated during the ion beam milling process. From the intercept value, a total coupling loss of 7.8 dB and 13.8 dB for the rib and stripe waveguide are obtained. The Fresnel reflection loss was estimated to be 1.1 dB assuming that Ta_2O_5 has a refractive index of 2. Taking this loss into account, the coupling loss arising from the modal mismatch was estimated to be 6.7 dB and 12.7 dB for the rib and stripe waveguide, respectively. These values are in close agreement with those obtained from the modal field overlap integrals in section 2.3 (5.9 dB for the rib and 11.2 dB for the stripe waveguide). Figure 2.5.2 shows the insertion loss for the TM mode. Following the same procedure as in the case of TE mode, the propagation loss is 1.7 dB/cm for the rib waveguide and 2.4 dB/cm for the strip waveguide. Taking into account the Fresnel reflection loss, the coupling loss is 7.4 dB and 13. dB for the rib and stripe waveguides, respectively.

Comparing the propagation loss between the TE and TM modes, it is found that the TE mode is more lossy than the TM mode. This polarization dependent loss (PDL) can be explained by the distribution of the modal field that aids identification of the loss mechanism. As shown in the previous section, the TE mode is less confined in the lateral direction while the TM mode is less confined in the vertical direction. For this reason, it is expected that sidewall roughness cause more scattering for the TE mode than interface ($Air/Ta_2O_5/SiO_2$) imperfections for the TM mode, causing the major propagation loss.

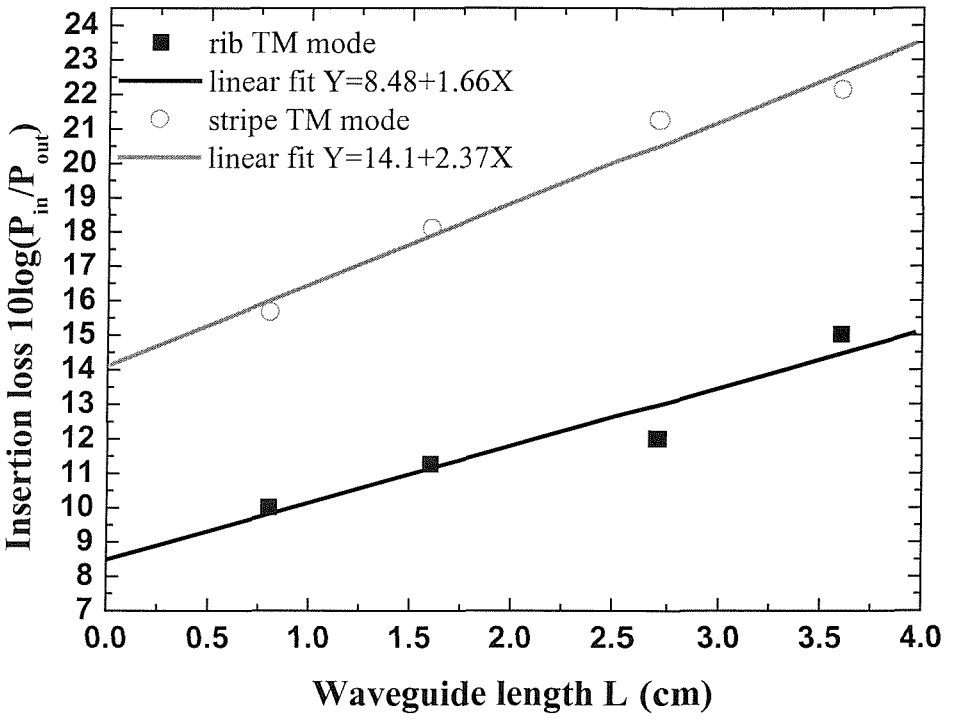

Fig. 2.5.2 Insertion loss of the TM mode as a function of waveguide length for the rib waveguide (W1H1h80) and the stripe waveguide (h=1 μm).

Table II lists the propagation and coupling losses, and the coupling losses are compared with those predicted by BPM. The error is attributed to the imperfectly cleaved waveguide facet and misalignment. Since the stripe waveguide has a more stringent alignment tolerance, it is to be expected that the error is higher than that in the rib waveguide. The result supports this justification.

Table II Individual loss separate from loss measurement

	Waveguide type			
	Rib waveguide		Stripe waveguide	
	TE	TM	TE	TM
Propagation loss (dB/cm)	1.78	1.66	2.52	2.37
Modal mismatch loss (dB)	6.7	7.4	12.7	13.0
BPM value (dB)	6.4	6.9	11.9	12.0
Error	7.3%	11.2%	15.6%	19%

2.6 Discussion

The goal of this thesis is to evaluate material properties (UV photosensitivity and optical nonlinearity) and to demonstrate the functionality of composite structures ultilising short length waveguides. According to Table II, a 2.5 dB/cm propagation loss in conjunction with a 13 dB/facet coupling loss yields a maximum fiber-chip-fiber insertion loss of ~30dB for a 1 cm long device. With this loss level and assuming a 10mW light source, the output signal is still within the apparatus detection limit. Nevertheless, for the purpose of combining more components to form densely packed sophisticated planar lightwave circuits, more effort need to be made on improving both the propagation loss and the coupling loss.

Sidewall roughness has been identified to be the major source which introduces excess propagation loss to the stripe waveguide, and this is a common feature for all of the high index contrast material systems. Oxidation smoothing has been proposed

for the SOI system,where the loss has been reduced from 32 dB/cm (conventional fabrication method) to 0.8 dB/cm [10]. For Ta_2O_5, oxidation smoothing may be applied on the wet-etched metallic Ta_2O_5 strip. This technique was originally been applied to obtain a low-loss Ta_2O_5 planar waveguide [11]. Apart from the sidewall roughness, the intrinsic loss of the as-grown film can be improved as well. Post-fabrication annealing treatment has been used for the reduction of the leakage current of the Ta_2O_5 film due to the reduced porosity and oxygen vacancies of the film [12]. However, the effect is limited since molecular oxygen cannot repair oxygen vacancies at low temperatures [13]. Oxygen-Radical annealing [13] or UV-assisted oxygen annealing [14] may provide an effective way leading to the improvement of the intrinsic loss. Recently, O_2 cluster ion assisted deposition [15] also presenting convincing result for further improvement of the thin film quality.

The coupling loss can be improved by incorporating tapered waveguide structures. A number of tapered structures for achieving low-loss fiber-to-chip coupling have been suggested [16-18]. In particular, the tapered velocity coupler (TVC) is most attractive due to its insensitivity to the operating wavelength and the polarization state. Less than 1dB fiber-to-waveguide coupling loss has been reported [19] which promises a route for further reduction of the coupling loss in the present study.

2.7 Conclusion

This chapter describes the fabrication of rib waveguides with a range of dimensions. Single mode cut-off dimensions (SMCD) for waveguides with different etch depths

were determined, and the result can be well described by Petermann's theory for oversized rib waveguides. Comparisons are made between a rib waveguide with an etch depth of 80 nm and a stripe waveguide having the same film thickness (1 μm) It is found that the width of the rib waveguide can be made three times (3 μm) wider than that of the stripe waveguide while still maintaining single mode operation at λ=1.55μm. This property greatly relaxes the stringent alignment tolerance for waveguide characterization. In addition, the required dimension is well within the range of conventional photolithography. The coupling efficiency with a standard telecommunication fibre was predicted using a modal field overlap integral. The result suggests that the coupling efficiency is enhanced by a factor of 3.4 for rib waveguide with a shallow etch depth. The propagation loss of the waveguides was determined by cut-back measurements and the coupling loss was separated from the measured total loss. From the propagation loss between rib and stripe waveguides, and the measured PDL, a substantial excess loss introduced to the propagation loss was confirmed to be due to sidewall roughness.

This chapter includes most of the important properties which provide useful guidelines for the design of waveguides. The waveguide structures described here form the building blocks of the devices in the following chapters. The correlation between the modal field distributions and the waveguide geometry, in particular, becomes the major design consideration for different applications. For example, less confined rib waveguides (Chapter 3) are preferred when mono-mode operation with high coupling efficiency is required. On the other hand, tightly confined stripe

waveguides (Chapter 4) are preferred for nonlinear applications because of the smaller effective area, which may exhibit larger nonlinear effect. It should also be noted that this approach can still be applied for waveguide of several microns thickness, as long as the thickness uniformity is at an acceptable level.

References

[1] Petermann K., Properties of optical rib-guides with large cross-section. Arch Electron Ubertragungstechnik, vol. **30**, p. 139 (1976).

[2] Richard A. Soref, Joachim Schmidtchen, and Klaus Petermann, IEEE J. Quantum Electron. Vol. **27**, p. 1971 (1991).

[3] J. Schmidtchen, A. Splett, B. Schüppert, and K. Petermann, Electron. Lett., vol. **27**, p. 1486 (1991).

[4] A. G. Rickman, G. T. Reed, and Fereydoon Namavar, J. Lightwave Technol., vol. **12**, p. 1771 (1994).

[5] U. Fischer, T. Zinke, J. –R. Kropp, F. Arndt, and K. Petermann, IEEE Photon. Tech. Lett., vol. **8**, p. 647 (1996).

[6] Wei Shi, Yujie J. Ding, Changshui Fang, Qiwei Pan, and Qingtian Gu, Optics and Laser in Engineering, vol. **38**, p. 361 (2002).

[7] *Corning® SMF-28™ Optical Fiber –Product Information* [Online]. 2002 [Accessed 3rd Jan 2004]. Available from World Wide Web: <http://www.corning.com/opticalfiber>

[8] R. Scarmozzino, A. Gopinath, R. Pregla, and S. Helfert, J. Selected Topics in Quantum Electron., vol. **6**, p. 150 (2000).

[9] S. I. Hosain, J. P. Meunier, and Z. H. Wang, J. Lightwave Technol., vol. 14, 901 (1996).

[10] K. K. Lee, D. R. Lim, L. C. Kimerling, J. Shin, and F. Cerrina, Opt. Lett., vol. **26**, 1888 (2001).

[11] D. H. Hensler, J. D. Cuthbert, R. J. Martin, and P. K. Tien, Appl. Opt., vol. **10**,

1037 (1971).

[12] S. Kamiyama, P. Y. Lesaicherre, H. Suzuki, A. Sakai, I. Nishiyama, and A. Ishitan, J. Electrochem. Soc., vol. **140**, 1617 (1993).

[13] Y. Matsui, K. Torii, M. Hirayama, Y. Fujisaki, S. Iijima, and Y. Ohji, IEEE Electron Device Lett., vol. **17**, 431 (1996).

[14] S. Tanimoto, M. Matsui, K. Kamisako, K. Kuroiwa, Y. Tarui, J. Electrochem, Mater., vol. **139**, 320 (1992).

[15] Y. Fujiwara, N. Toyoda, K. Mochiji, T. Mitamura, I. Yamada, Nucl. Instrum. Met. Phys. Res. B, vol. **206**, 870 (2003).

[16] A. F. Milton and W. K. Burns, Appl. Opt., vol. **14**, 1207 (1975).

[17] O. Mitomi, K. Kasaya, and H. Miyazawa, IEEE J. Quantum Electron., vol. **30**, 1787 (1994).

[18] M. K. Chin and C. W. Lee, Optics Express, vol. **12**, 117 (2003).

[19] T. Bakke, C. T. Sullivan, S. D. Mukherjee, J. Lightwave Technol.. vol. **20**, 1188 (2002).

Chapter 3 Evaluation of UV photosensitivity using Ta_2O_5 rib waveguide Mach-Zehnder interferometers

3.1 Introduction

Photosensitive materials have many diverse applications due to the availability of simple, direct and low-cost techniques for optical inscription of microstructures in bulk, thin film and fibre materials. In particular, Germania-doped silica has received considerable attention due to the potential for high-performance optical fibre devices and due to the enhancement of its photosensitivity by hydrogen loading [1]. UV induced refractive index change as large as 0.01 have been achieved by diffusing hydrogen into glass at high pressures [2]. Using photoinduced refractive index change, Bragg gratings are routinely inscribed holographically into the core of fibers [2] and planar waveguides [3]. A variety of guided wave devices including buried channel waveguides [4], directional couplers and power splitters [5]-[7] have been demonstrated using the UV direct-writing technique.

In addition to writing of microstructures, photosensitivity has also been considered as a powerful technique for post-fabrication trimming of devices [8]-[9]. Existing fabrication techniques are often insufficient to control dimensions precisely down to the wavelength scale, so that errors may be incorporated during the fabrication process. These errors cause variations in optical path lengths, leading to the degraded performance of devices. Therefore, it needs to be compensated in a simple and inexpensive way such as UV trimming. The potential for direct writing of waveguides, for trimming of devices, and for superimposing microstructures in

conventional waveguides give photosensitive materials an important role in optoelectronics. In particular the UV trimming of the band-edge wavelengths of a photonic crystal waveguide could be a useful application of this technique.

To evaluate the photosensitivity, different device structures such as diffraction gratings and thin film fiber couplers can be used [10]. In this chapter, the fabrication of a Mach-Zehnder interferometer based on a Ta_2O_5 rib waveguide structure is described together with its use for the evaluation of the photosensitivity. Tuning of the MZI phase is achieved by UV light irradiation on one arm of the MZI. In Section 3.2, the waveguide design considerations and the fabrication process are described. Section 3.3 details the UV-tuning experiment and the procedure for the calculation of the induced refractive index change. A comparison between the experimental result and that simulated by the beam propagation method (BPM) is also presented. A summary is given in section 3.4.

3.2 Design considerations and fabrication

The top view and the cross-section of the MZI are shown in Figures 3.2.1. A rib waveguide structure with a shallow etch depth was chosen because single mode operation could be achieved with a large modal width, resulting in reduced coupling loss to conventional monomode fibre, as described in chapter 2. In the layout of the MZI, in order to avoid excess radiation loss, the S-bend radius was chosen to be large (63 mm), and the separation between the two arms was chosen to be small (50 μm) to keep the splitting angle of the two S-bends small. The UV exposure window

was 3 mm long and sufficiently wide that all the Ta_2O_5 in which the mode propagates was irradiated over the 3mm length.

To create such a structure, a 1 μm thick layer of Ta_2O_5 was first RF sputtered onto a Si wafer with a 2 μm SiO_2 buffer layer, in an Ar/O_2 atmosphere with the substrate held at 250°C. During the sputtering process, the chamber pressure was kept at 35 mTorr with Ar/O_2 flow rate set to16 sccm and 6 sccm, respectively. The film was subsequently annealed in pure O_2 at 500℃ for 12 hours.

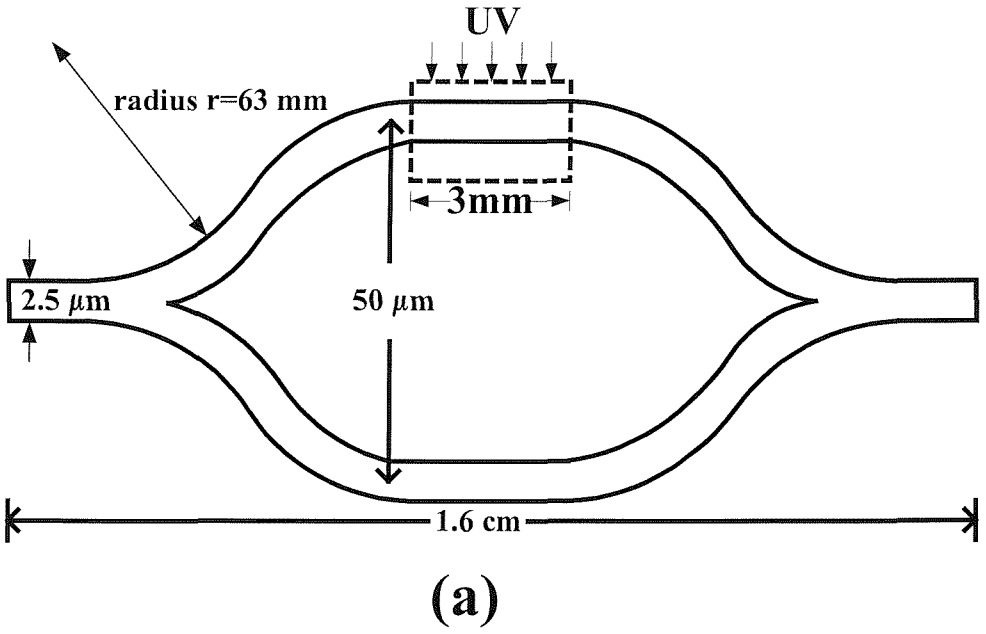

Fig. 3.2.1 Configuration of the rib waveguide Mach-Zehnder interferometer (MZI): (a) Top view of the MZI. The exposed region is enclosed by a dashed line.

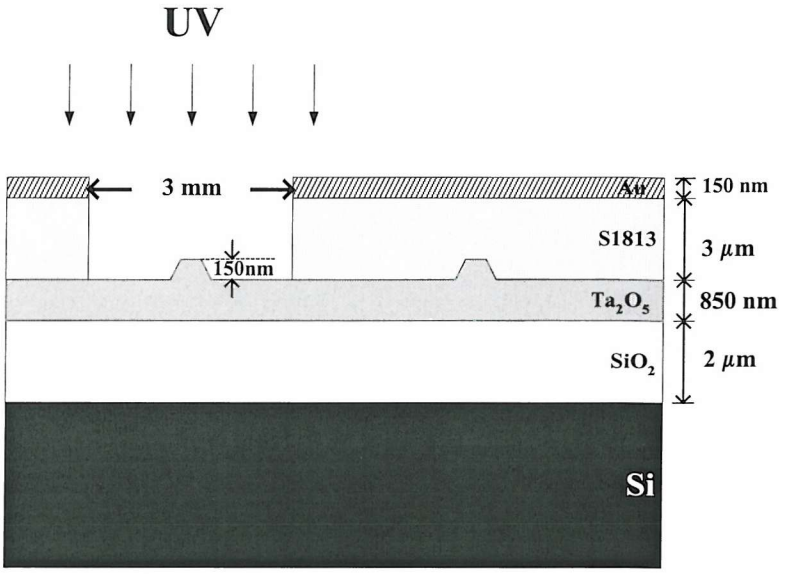

(b)

Fig. 3.2.1(b) Cross-sectional view of the MZI. The thickness and refractive index of individual layers are: Au (150 nm), S1813 (n=1.6, 3μm), Ta_2O_5 (n=2, 1μm) and SiO_2 (n=1.46, 2μm).

According to the report in [11], a stoichiometric thin film may be obtained provided the oxygen flow is appropriately set during the sputtering process. In addition, based on reference 18, the residual stress can be further reduced by annealing the as-grown film in pure O_2 at 450℃ for 30 minutes. These conditions are close to the fabrication condition in this study, therefore, a closely stoichiometric and nearly stress-free film is expected here.

The MZI pattern was formed in a photoresist layer spin-coated onto the Ta_2O_5 film, using standard photolithography, and subsequently transferred into the Ta_2O_5 by argon ion beam milling [12], as described in chapter 2. The rib waveguides used in

the MZI were nominally 2.5 μm wide and were etched to a depth of 150 nm, as shown in Figure 3.2.1(b). The shallow etch depth was chosen in order to ensure single mode operation at wavelength λ=1.55 μm, as described in chapter 2. The MZI waveguides were clad with a 3 μm layer of photoresist (n~1.6), which was overexposed to eliminate the possibility of any further changes in index due to subsequent UV exposure. The cladding material absorbs UV, so that a window is opened in it over one waveguide to allow localized exposure. However, to ensure that no residual UV light penetrates the cladding and exposes other parts of the structure, an additional 150 nm thick layer of Au, acting as a light blocking layer, was sputtered onto the device and the 3 mm long window was opened over one arm of the MZI, in both the gold and the photoresist, to enable UV exposure of that arm alone. This procedure allows a large area of the sample to be illuminated by the excimer laser beam, while only the desire part of the waveguide circuit is exposed, eliminating the need for precise alignment in the UV-writing setup.

3.3 Experimental results and discussion

Prior to the UV irradiation, the propagation loss of a straight rib waveguide with the same cross-section was measured to be 1.6 dB/cm using the cut-back technique, and the waveguide confirmed to be monomode at λ=1.5 μm. The absorption spectrum for a 1 μm thick Ta_2O_5 thin film sputtered on a CaF_2 substrate was measured by spectrophotometry and is shown in Fig. 3.3.1. The strong absorption below λ=263 nm indicates that there is potential for UV irradiation below this wavelength to result in an index change.

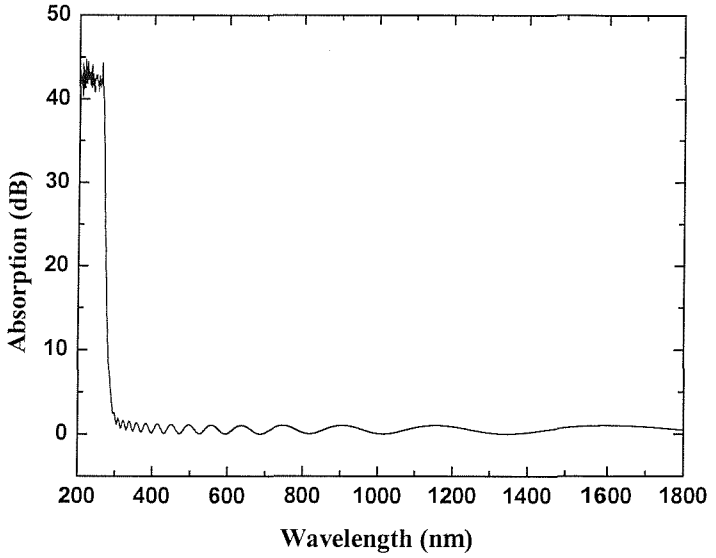

Fig. 3.3.1 Absorption spectrum for 1μm thick Ta_2O_5.

The experimental arrangement for UV-tuning was shown in Fig. 3.3.2. Ultraviolet light from an excimer laser operating at wavelength λ=248 nm, with a repetition rate of 1 Hz and a pulse duration of 20 ns, was directed toward to the region to be exposed on the MZI. Prior to exposure of the sample itself, the beam was focused and adjusted through an aperture until the energy was evenly distributed over a spot of diameter 16 mm. This was accomplished by visually inspecting the image recorded on thermally sensitive paper. The energy density for each single shot was measured to be 0.024 J/cm^2. A DFB laser operating at λ=1550 nm, with a polarization maintaining (PM) fibre pigtail, was on-off modulated with a square wave at 1 kHz and the output radiation end-fire launched into the MZI in the TE polarisation. The output of the MZI was directed onto an InGaAs detector through a 40× microscope objective. The signal was then fed into a lock-in amplifier and was

monitored and acquired by a computer.

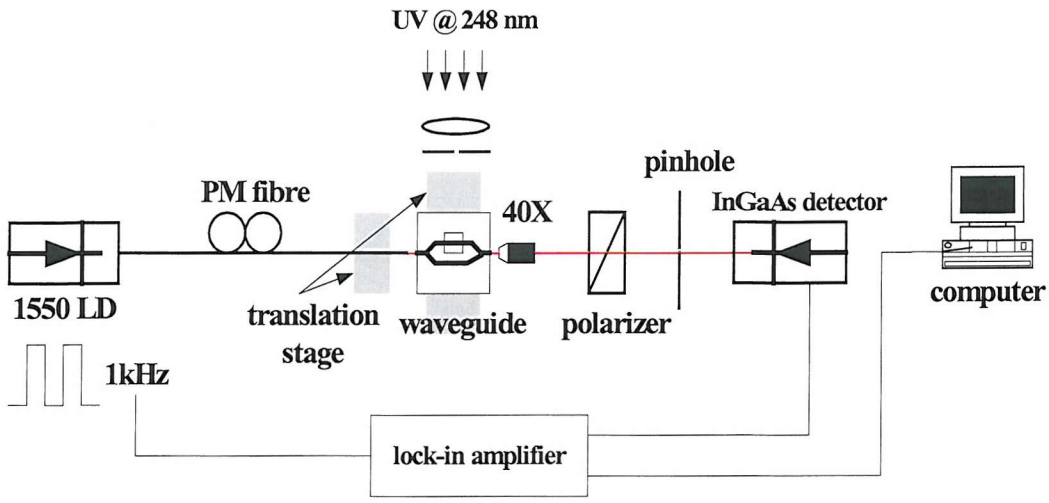

Fig. 3.3.2 Experimental setup for the UV-tuning experiment.

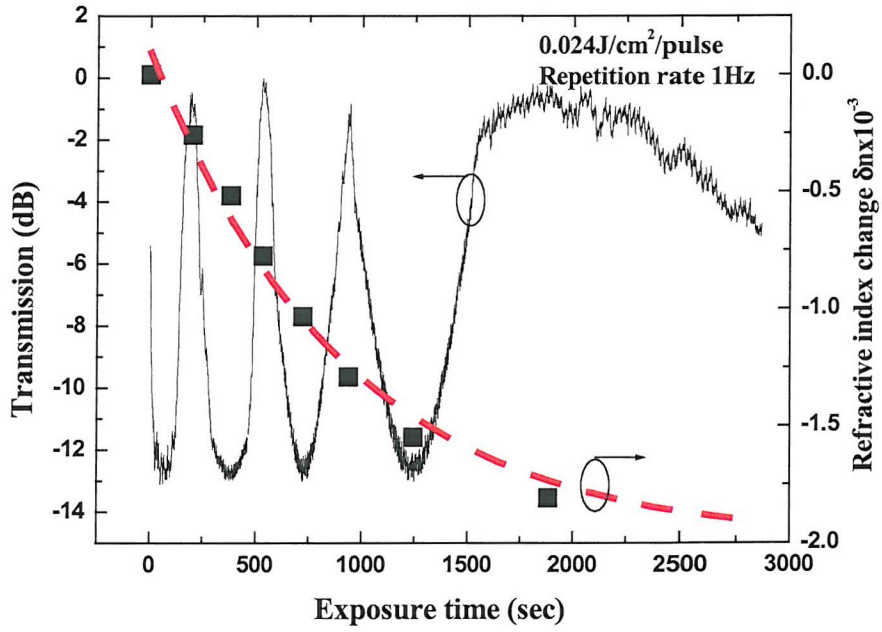

Fig. 3.3.3 Output power as a function of exposure time. The dashed line shows the calculated refractive index change.

Figure 6.3.3 shows the normalized output power as a function of the exposure time. The periodic modulation characteristic arises from the UV induced phase shift

defined by the following equation:

$$\Delta\phi = \frac{2\pi\Delta N_{eff} L}{\lambda} \tag{3.1}$$

where ΔN_{eff} is the effective refractive index change, L is the length of the exposed region (3 mm), and λ is the wavelength of the signal. The output power response of the MZI is then described by:

$$P_{out} = P_{in} \cos^2(\tfrac{1}{2}\Delta\phi) \tag{3.2}$$

A π radian phase shift requires an effective index change of 2.5×10^{-4} according to eqn.(3.1), for the wavelength and length under consideration. As the differential phase shift increased with fluence, the MZI cycled through several on and off states with an extinction ratio of -13 dB. This extinction ratio is believed to be limited by the contribution of scattered light, not passing through the MZI, being collected by the lens. With a total cumulative fluence of 72 J/cm^2, a total phase shift of 8π radians was observed, corresponding to a refractive index change $(2.1\pm0.1)\times10^{-3}$. The chirped modulation period shows that the rate of induced index change reduced with exposure energy and that it saturates with a longer exposure time. Figure 3.3.3 also shows that the calculated index change decays approximately exponentially with exposure time, which confirms this point. The noisy behavior after 1500 seconds is attributed to the degraded stability of the alignment of the apparatus.

To determine whether the induced refractive index change is positive or negative, a further experiment was performed on a rib waveguide Y junction as shown in Fig. 3.3.4. The waveguides are the same as those in the MZI with an identical device

being cleaved in half to produce two Y-junctions. A window was opened, in a UV blocking layer, on one arm of a Y-branch and part of the input waveguide, as shown by the enclosed region in Fig. 3.3.4.

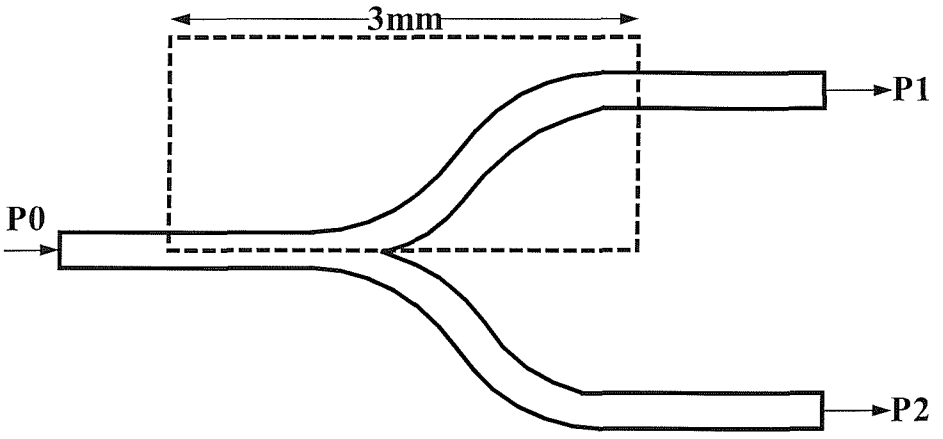

Fig. 3.3.4 Top view of the rib waveguide Y-junction. The exposed region is enclosed by a dashed line.

UV irradiation was carried out as with the MZI, and the power splitting ratio was monitored. Fig. 3.3.5 shows the modal power distributions for the post-trimmed Y-junction, and their relative intensity indicates the output power ratio. Before exposure the power splitting ratio was 50:50 with ±1% estimation error, and this was trimmed to 46:54 after ~3000 shots, showing a decreased power output from the branch exposed to UV.

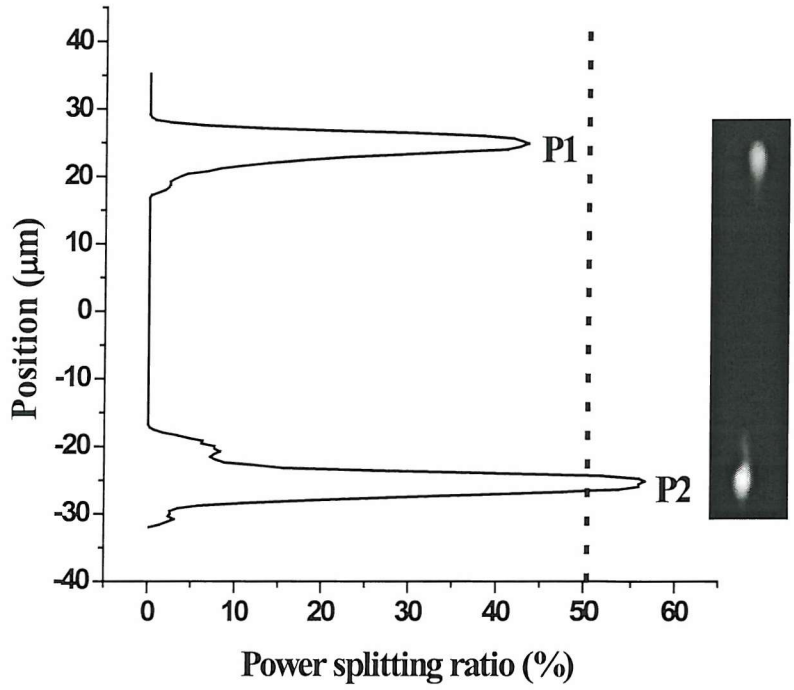

Fig. 3.3.5 The output power of the two branches. The inset shows the modal field profile recorded by the CCD camera.

This structure with reduced refractive index Δn=-0.0021 in the enclosed region was simulated by the beam propagation method [14], and the modal power evolution along the Y-junction was plotted in Fig. 3.3.6. The power splitting ratio at the end of the Y branch was found to be 40:60, in reasonable agreement with the experimental result. The discrepancy between theory and experiment is believed to be due to inaccuracy in placing the UV blocking mask, which is modeled to be precisely aligned along the centre of the 2.5 μm wide input waveguide.

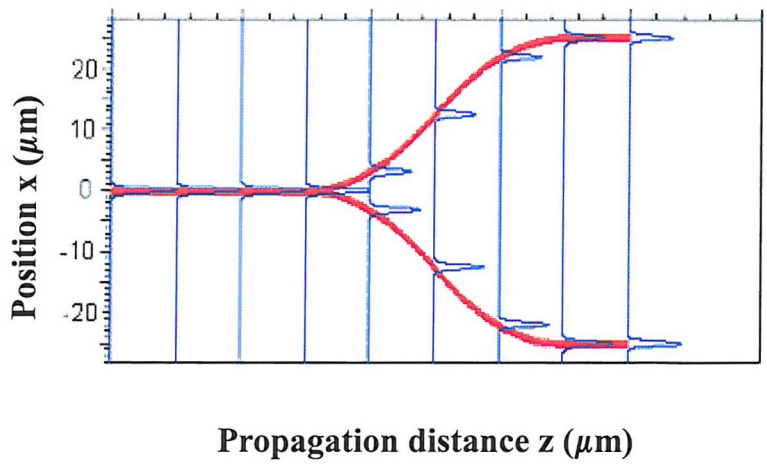

Fig. 3.3.6 The structure in fig 3.3.4 simulated by beam propagation method.

Since there is no noticeable degradation of the modulation visibility in Fig. 3.3.3 as fluence increases, UV induced excess loss at the signal wavelength is ruled out. Therefore, this behavior indicates that UV light induces a negative index change in the exposed arm, as the optical power flows preferentially into the arm with the higher refractive index.

It is notable that the achieved index change is significant without any pretreatment such as hydrogen loading. Compared to conventional germanosilicate glass, this presents a substantial advantage since hydrogen loading introduces some unwanted effects. Transient behavior due to the gas out-diffusion and excess loss due to UV induced absorption at λ=1.5μm are the most serious problems [15]. To date, low-loss, intrinsically UV photosensitive germanosilicate glass has been fabricated by hollow cathode plasma-enhanced chemical-vapor deposition (HC-PECVD) technique [16]. However, an index change of 2×10^{-3} requires a cumulative UV

fluence of over 1 kJ/cm^2, which is substantially higher than that (72 J/cm^2) of the Ta_2O_5 reported here.

3.4 Conclusion

In this chapter, the fabrication of a Mach-Zehnder interferometer using rib Ta_2O_5 waveguides was described. The adjustment of the optical path length in one branch of the MZI using UV irradiation is reported. Tuning over 4 periods was achieved through the differential photoinduced phase shift between the two arms of the MZI. The device exhibits an extinction ratio of -13 dB and a negative UV-induced refractive index change of 2.1×10^{-3}.

The low material absorption throughout the telecommunication wavelength window [17] and high refractive index in conjunction with the significant UV photosensitivity presented in this chapter shows the great potential of Ta_2O_5 for compact optical waveguide devices in the 1.5 μm telecommunications window, with the advantages of combined UV written and relief waveguide structures, and the flexibility to correct fabrication errors through UV trimming. Moreover, since the group velocity of optical pulses was dispersed and delayed at the photonic band edge, the significant UV photosensitivity may provide a simple route for tuning of the photonic crystal based dispersion compensation devices.

References

[1] P. J. Lemaire, R. M. Atkins, V. Mizrahi, and W. A. Reed, Electron. Lett., vol. **29**, 1191 (1993).

[2] K. O. Hill, Y. Fujii, D. C. Johnson, and B. S. Kawasaki, Appl. Phys. Lett., vol. **32**, 647 (1978).

[3] J. E. Romàn, and K. A. Winick, Opt. Lett., vol. **18**, 808 (1993).

[4] M. Svalgaard, C. V. Poulsen, A. Bjarklev, and O. Poulsen, Electron. Lett., vol. **30**, 1401 (1994).

[5] G. D. Maxwell, and B. J. Ainslie, Electron. Lett., vol. **31**, 95 (1995).

[6] M. Svalgaard, Electron. Lett., vol. **33**, 1694 (1997).

[7] Kjartan Faerch, and Mikael Svalgaard, IEEE Photon. Technol. Lett., vol. **14**, 173 (2002).

[8] R. Kashyap, G. D. Maxwell, and B. T. Ainslie, IEEE Photon. Technol. Lett., vol. **5**, 191 (1993).

[9] K. P. Chen and P. R. Herman, IEEE Photon. Technol. Lett., vol. **14**, 71 (2002).

[10] M. P. Roe, "Photosensitive and piezoelectric thin films for optical devices", PhD. Thesis, University of Southampton, Southampton, (1995).

[11] J. M. Ngaruiya, S. Venkataraj, R. Drese, O. Kappertz, T. P. Leervad Pedersen, and M. Wuttig, Phys. Stat. Sol., vol. **198**, 99 (2003).

[12] C. Christensen, R. de Reus, and S. Bouwstra, J. Micromech. Microeng., vol. **9**, 113 (1999).

[13] K. P. Lee, K. B. Jung, R. K. Singh, S. J. Pearton, C. Hobbs, and P. Tobin, J. Vac. Sci. Technol. A, vol.**18**, 1169 (2000).

[14] BeamPROP™ version 5.0.

[15] M. V. Bazylenko, M. Gross, P. L. Chu, and D. Moss, Electron. Lett., vol. **32**, 1198 (1996).

[16] M. V. Bazylenko, D. Moss, and J. Canning, Opt. Lett., vol. **23**, 697 (1998).

[17] E. Franke, C. L. Trimble, M. J. Devries, J. A. Woollam, M. Schubert, and F. Frost, J. Appl. Phys., vol. **88**, 5166 (2000).

Chapter 4 Determination of nonlinear refractive index in a Ta_2O_5 rib waveguide using self-phase modulation (SPM)

4.1 Introduction

Reliable, efficient generation of high peak power, ultrashort laser pulses has allowed the exploitation of many new material phenomena and, in particular, is stimulating intensive research into nonlinear optical effects. Ultrafast all-optical switching devices will play an increasingly important role in modern optical communication systems where signals are transmitted at high speed and high-bit-rate. Nonlinear refraction which exploits third-order electronic polarization has a subpicosecond response time and is thus suitable for high speed switching. Silica optical fibers have been widely used for all-optical switching due to their low loss and long interaction length. However, the small nonlinear refractive index of silica, n_2 ($\sim 2.2\times10^{-20}$ m^2/W) [1], requires high switching power and a very long length of fiber to achieve useful optical switching. Although many materials with higher nonlinear refractive index have been reported [2]-[6], there is a need to explore alternatives, particularly those compatible with planar processing technology, due to the rapid growth of planar devices such as wavelength division multiplexers and add-drop filters in advanced networks.

To achieve compact low-power high-speed switching devices, a large optical nonlinear refractive index (n_2) is required. In addition, materials with minimal loss and absorption at the operating wavelength, a fast response, low toxicity with highly

thermal and mechanical stability are preferred. Although Ta_2O_5 is widely used for multilayer dielectric mirrors, there are no reports, to the knowledge, on its optical nonlinearity to date. In this chapter, the experimental measurement of the nonlinear refractive index in a Ta_2O_5 rib waveguide, based on self-phase modulation (SPM) induced spectral broadening is presented. Section 4.2 briefly describes and compares several experimental techniques for measuring n_2, with the emphasis put on SPM, which is the technique employed in this study. In section 4.3, the experimental configurations are detailed, and the observed SPM spectra are presented. In section 4.4, a simplified theory is introduced and the procedure leading to the estimation of the associated nonlinear refractive index n_2 is described. The impact of group velocity dispersion (GVD) is discussed in section 4.5, where the femtosecond time of flight measurements is described. Based on the GVD value obtained, the validity of the estimated n_2 is confirmed. A conclusion is given in section 4.6.

4.2 Experimental techniques and theoretical background

The optical third order nonlinear effect (also termed the Kerr effect) is characterized by the intensity dependent refractive index $n=n_0+n_2I$, where n_2 is the nonlinear refractive index. Although n_2 is very small (10^{-19}-10^{-20} m^2/W for most materials) compared to the linear part (n_0), it cannot be ignored, particularly in transmission systems utilizing high-peak-power light sources, and amplifiers [7]. Several experimental techniques such as self-phase modulation (SPM) [8], cross-phase modulation (XPM) [9], modulational instability (MI) [10], and four-wave mixing

(FWM) [11] have been used for the determination of n_2 based on different nonlinear processes. XPM and FWM need to incorporate at least two pump beams into the waveguide under investigation, increasing the complexity of the setup. On the other hand, MI, originating from the interplay between the nonlinear and the dispersive effect, must be performed in the anomalous dispersion regime. SPM, utilizing a single pump beam, is relatively simple and was used in this study for the determination of n_2. The following gives a brief overview of the theoretical background of this effect.

The propagation of optical pulses in a dispersive and nonlinear medium is governed by the nonlinear Schrödinger equation (NLSE) [12]:

$$\imath\frac{\partial U}{\partial z}=\frac{\mathrm{sgn}(\beta_2)}{2L_D}\frac{\partial^2 U}{\partial \tau^2}-\frac{\exp(-\alpha z)}{L_{NL}}|U|^2 U \tag{4.1}$$

where α accounts for the loss of the waveguide, $\mathrm{sgn}(\beta_2)=\pm 1$ depends on the sign of the group velocity dispersion β_2, $U(z,\tau)$ is the normalized amplitude, and τ is a time scale normalized to the initial pulse width T_0 through

$$\tau=\frac{T}{T_0}=\frac{t-z/v_g}{T_0} \tag{4.2}$$

where T is measured in a frame of reference moving with the group velocity v_g of the pulse. The dispersion length L_D and the nonlinear length L_{NL} are defined as:

$$L_D=\frac{T_0^{\,2}}{|\beta_2|} \tag{4.3}$$

$$L_{NL}=\frac{1}{\gamma P_0} \tag{4.4}$$

where P_0 is the peak power of the incident pulse, and the nonlinear coefficient γ is

defined by:

$$\gamma = \frac{n_2 \omega_0}{cA_{eff}} \tag{4.5}$$

where n_2 is the nonlinear refractive index, ω_0 is the central frequency of the pulse, c is the speed of light in vacuum and the effective area A_{eff} is defined by:

$$A_{eff} = \frac{\left[\iint |F(x,y)|^2 \, dxdy\right]^2}{\iint |F(x,y)|^4 \, dxdy} \tag{4.6}$$

where F (x,y) is the mode field distribution. The physical meaning of L_D is that at $z=L_D$, the Gaussian pulse broadens by a factor of $\sqrt{2}$; while for L_{NL}, it is the effective propagation distance at which the nonlinear phase shift $\phi = 1$.

To understand the pulse evolution along the waveguide requires the numerical solution of equation (4.1). The relative magnitude of the two characteristic lengths L_D , L_{NL}, and the sample length L, describes the relative significance of the nonlinear and the dispersive effect. However, assuming that $L_D > L > L_{NL}$ provides a way to simplify equation (4.1) while still keep physical insight on the propagation behavior of a pulse as the dispersion term may be ignored. For pure SPM effect (GVD $\beta_2=0$), the first term in equation (4.1) is zero and the equation can be readily solved analytically to obtain:

$$U(z,T) = U(0,T)\exp[\imath\phi_{NL}(z,T)] \tag{4.7}$$

where the intensity-dependent nonlinear phase shift is:

$$\phi_{NL}(z,T) = |U(0,T)|^2 \left(\frac{Z_{eff}}{L_{NL}}\right) \tag{4.8}$$

with

$$z_{eff} = \frac{[1-\exp(-\alpha z)]}{\alpha} \tag{4.9}$$

SPM induced spectral broadening is a consequence of the time dependence of the nonlinear phase shift and can be described as:

$$\delta\omega(T) = -\frac{\partial\phi_{NL}}{\partial T} = -\frac{\partial}{\partial T}\left(|U(0,T)|^2\right)\frac{z_{eff}}{L_{NL}} \tag{4.10}$$

From (4.10), it can be seen that for a Gaussian pulse, the leading edge of the pulse induces a negative frequency chirp (wavelength red shifted) and the trailing edge induces a positive frequency chirp (wavelength blue-shifted). As a consequence, the spectrum broadens. By measuring the bandwidth of the SPM spectrum as a function of the incident power, the nonlinear refractive index n_2 can be extracted using equation (4.10). The sign of n_2 could be confirmed by inserting a fibre with zero GVD at the operating wavelength and a known n_2 into the optical path. By comparing the output spectrum with that in the absence of the fibre, the sign of n_2 can be determined from the broadening or narrowing of the spectrum, as discussed in [13].

4.3 SPM experiment and results

The waveguide under investigation was fabricated by sputtering a 1 μm thick Ta_2O_5 film onto a Si wafer, on which a 2 μm thick SiO_2 buffer layer had been grown. Photolithography and argon ion beam milling were then used to create stripe waveguides in the Ta_2O_5 with a width of 3μm and a depth of 1μm. The wafer was then cleaved into chips of 10mm length to allow end-fire coupling of light. The

fundamental mode of the waveguide was excited at λ=800 nm and the loss corresponding to the mode was measured to be ~1.5 dB/cm. Fig. 4.3.1 shows the cross-sectional view of the stripe waveguide structure and the excited fundamental mode recorded by the infrared camera.

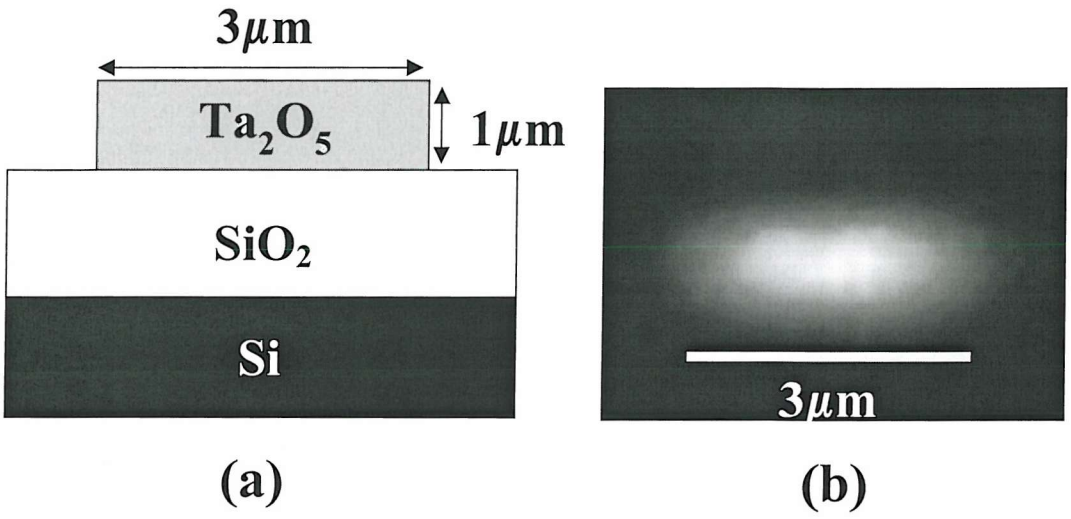

Fig. 4.3.1 (a) The cross-sectional view of the stripe waveguide. (b) The modal intensity profile of the fundamental waveguide mode.

The experimental apparatus for the SPM measurement is shown schematically in Fig. 4.3.2. A diode-pumped frequency-doubled Nd:YVO_4 laser, producing single frequency output at λ=532 nm, was used to pump a Ti-Sapphire laser which generated sub-150 femtosecond modelocked pulses at λ=800 nm with a repetition rate of 80 MHz. These pulses seeded a regenerative amplifier system (RegA) working at a 250 kHz repetition rate. Nearly transform-limited pulses with duration at full width half maximum of Δt_{FWHM}=160 fs were obtained. The pulses were then end-fire launched into the rib waveguide using a microscope objective lens. The light emerging from the waveguide was collected and directed into a high resolution

spectrum analyzer without passing through any other optical components. The incident power was controlled by using calibrated neutral density filters and the modal intensity profile was monitored using a CCD camera to confirm single mode operation and to determine the modal spotsize.

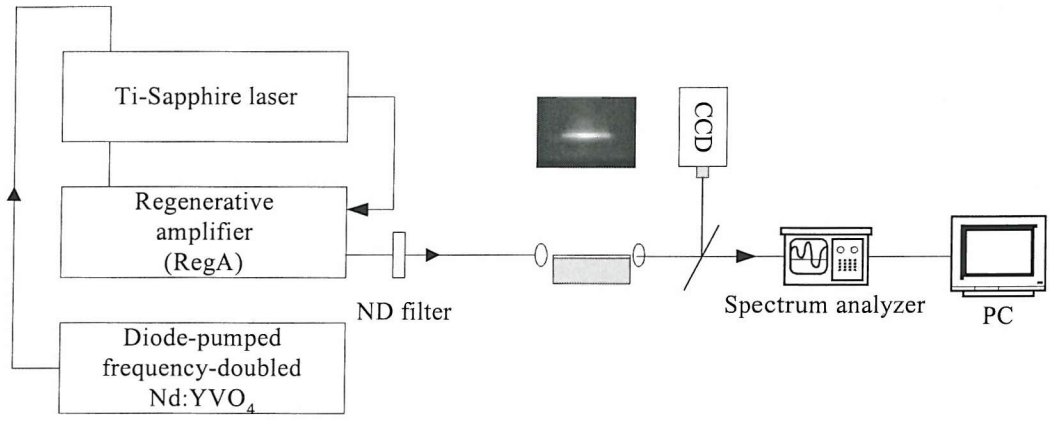

Fig. 4.3.2 Experimental apparatus for measurement of n_2.

Fig. 4.3.3(a) shows the spectrum of the incident pulses at the output of the regenerative amplifier, while Fig. 4.3.3(b)-(d) shows the observed spectral evolution of this transform-limited Gaussian pulse having passed through the 1-cm-long Ta_2O_5 rib waveguide at various peak coupled powers. From the measurement of the input to output power ratio, and taking account of the propagation loss, the coupling loss was estimated to be 18 dB. As the peak power in the waveguide was increased, the output spectrum broadened significantly, accompanied by the development of oscillatory structures with intense outermost peaks. This multipeak structure, arising from the interference of the chirped frequency components induced by SPM, is the signature of SPM spectra [12] and is clearly in evidence in Fig. 4.3.3.

There are also several other features worth mentioning. It should be noted that as the peak coupled power is increased to 113.4 W, noticeable sidelobes developed on either side of the central wavelength (Fig. 4.3.3(c)). This indicates that higher order nonlinear processes start to take place at this power lever. As the peak coupled power is increased to 176 W, the spectrum (Fig. 4.3.3(d)) has a shape that no longer resembles the typical SPM spectrum, indicating that higher order competing nonlinear effects such as optical wave breaking (OWB), self-steeping, stimulated Raman scattering (SRS), and combined effects with group velocity dispersion (GVD) have taken place. These higher order phenomena are demonstrated by the appearance of sidelobes and the asymmetric broadening in the spectra [12].

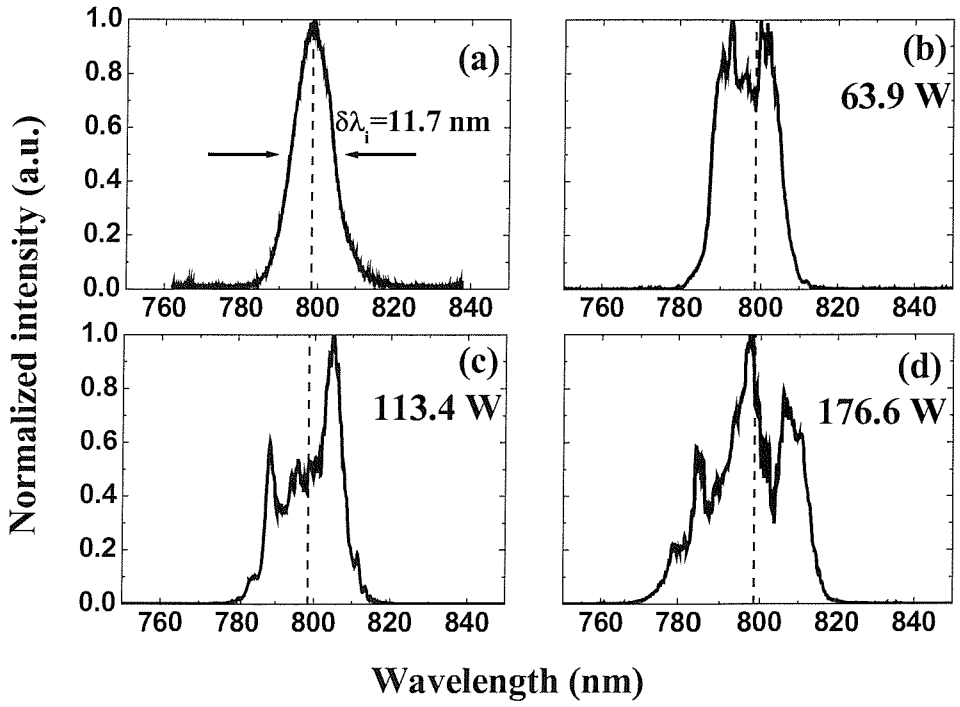

Fig. 4.3.3(a) Spectrum of the incident radiation; (b), (c) and (d) Observed self-phase modulation output spectra at peak coupled powers of 63.9 W, 113.4 W, and 176.6 W.

4.4 The estimation of n_2

To calculate the nonlinear refractive index, n_2, the simplified theory which ignores the influence of GVD was employed as the lowest-order approach [12]. The SPM-induced frequency shift is a consequence of a temporally varying phase and can be expressed in terms of the intensity-dependent refractive index n_2 as

$$\delta\omega = -\frac{\partial\phi_{NL}}{\partial t} = -\frac{2\pi}{\lambda}\cdot n_2 \cdot L_{eff} \cdot \frac{dI(t)}{dt} \tag{4.11}$$

where I(t) is the temporal intensity profile of the incident pulse and L_{eff} is the effective length defined by

$$L_{eff} = \frac{1-\exp(-\alpha L)}{\alpha} \tag{4.12}$$

in which L is the physical sample length and α is the attenuation constant. For an unchirped Gaussian input pulse, the full width half maximum (FWHM) spectral bandwidth, $\delta\lambda$, of the SPM pulse can be found from Equation (4.11) to be [14]:

$$\delta\lambda = \delta\lambda_i + 4\sqrt{\frac{2\ln 2}{e}}\cdot\frac{\lambda n_2 L_{eff}}{cA_{eff}}\cdot\frac{P}{t_p} \tag{4.13}$$

where $\delta\lambda_i$ and t_p represent the bandwidth and pulsewidth of the input laser pulse, respectively. P is the peak input power and A_{eff} is the effective core area defined by equation (4.6).

Figure 4.4.1 shows the SPM-induced spectral bandwidth (FWHM value), $\delta\lambda$, against the peak coupled power with a linear least-squares fit to the data points. This verifies the linear relationship between bandwidth and power predicted by Eqn. (4.13). Extrapolating the line to P=0, representing the bandwidth of the input pulse,

yields an intercept value of 12±0.4 nm, which is in good agreement with the recorded input spectrum ($\delta\lambda_I$=11.7±0.4 nm), as shown in Fig. 4.3.3(a).

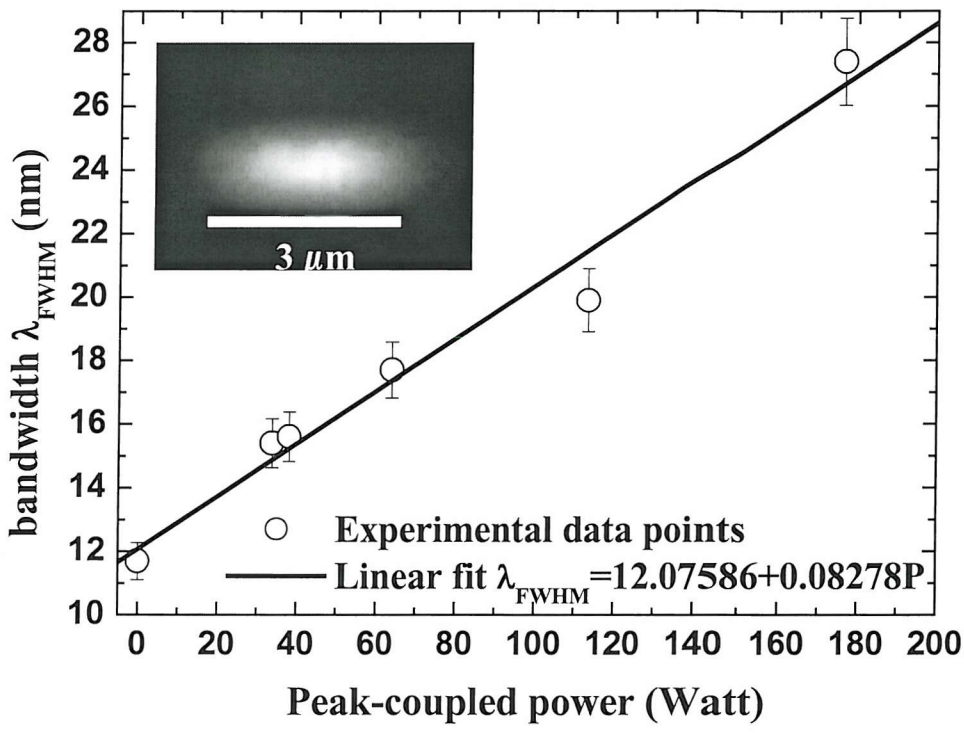

Fig. 4.4.1 SPM spectral bandwidth against peak-coupled power; the inset shows the modal intensity profile from the rib waveguide.

The nonlinear refractive index, n_2, was estimated from equation (4.13) using the fitted slope (0.083 nm/W), and the following values for the other parameters: α=0.345 cm^{-1} measured by imaging of scattered light [15], L=1 cm, A_{eff}=(3.5±0.18) μm^2 estimated from the recorded modal intensity profile from eqn. (4.6), λ=800 nm and t_p=160 fs. In this way, the intensity-dependent refractive index n_2 was found to be (7.2±0.4)×10^{-19} m^2/W, which is higher than silica glass (n_2 ~2.2×10^{-20} m^2/W) by

more than one order of magnitude.

4.5 Chromatic dispersion

In the previous section, the value of n_2 was obtained under the assumption that the group velocity dispersion (GVD) has a negligible impact on the pulse shape. To ascertain the validity of this assumption, femtosecond time of flight measurements, based on a Kerr shutter configuration [16] as shown in Fig. 4.5.1, were used to investigate the effect of GVD.

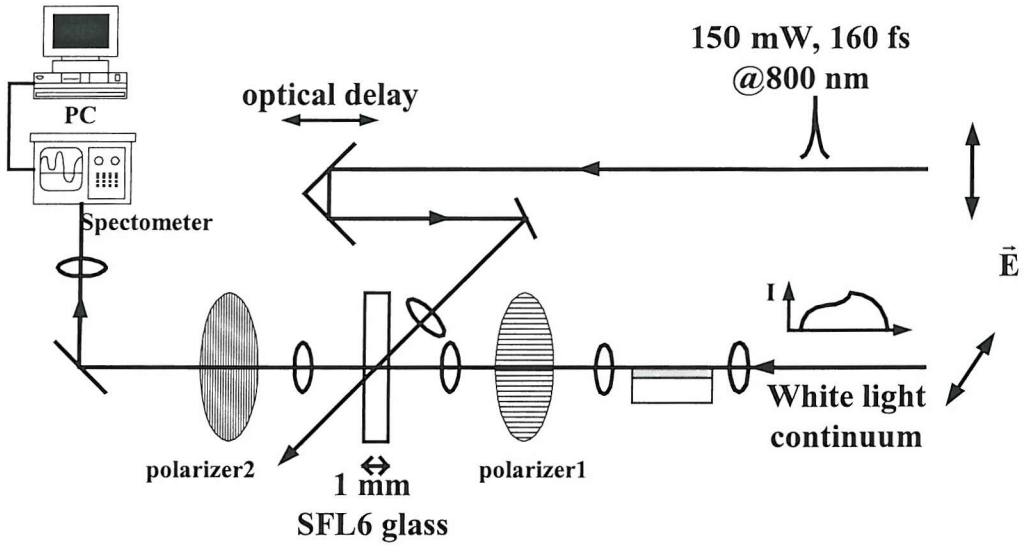

Fig. 4.5.1 Experimental configuration for femtosecond time of flight measurements.

The optical Kerr shutter was composed of a 1 mm thick SFL6 glass plate between two crossed polarizers. SFL6 glass has a high third-order nonlinear susceptibility which responses to the pump pulse almost instantaneously [17]. When a pump pulse (150 mW, λ=800nm, 160fs) is incident on the glass plate, a transient birefringence is induced, allowing the ultrabroadband white light continuum (WLC) probe pulse (from 450 nm to 1100 nm) to pass through. In order to exclude the intense

component at λ=800 nm, and prevent damage to the detector, an available hot mirror was used to cut out wavelengths longer than 710nm. The time delay of the pump pulse was scanned, and the spectrum of the resultant gated signal at each time delay was analyzed on a spectrum analyzer and recorded. This results in a temporally resolved spectrum, where the gated transmission spectra can be expressed as a correlation function as [18]:

$$S(\tau,\lambda) = \kappa \int_{-\infty}^{\infty} I_{WG}(t,\lambda) I_{gate}^{2}(t-\tau)dt \qquad (4.14)$$

where κ is a constant related to the Kerr efficiency, and I_{WG} and I_{gate} are the intensities of the transmitted WLC probe and the pump gate pulse, respectively. Fig. 4.5.2 shows the typical gated spectra recorded at each time delay.

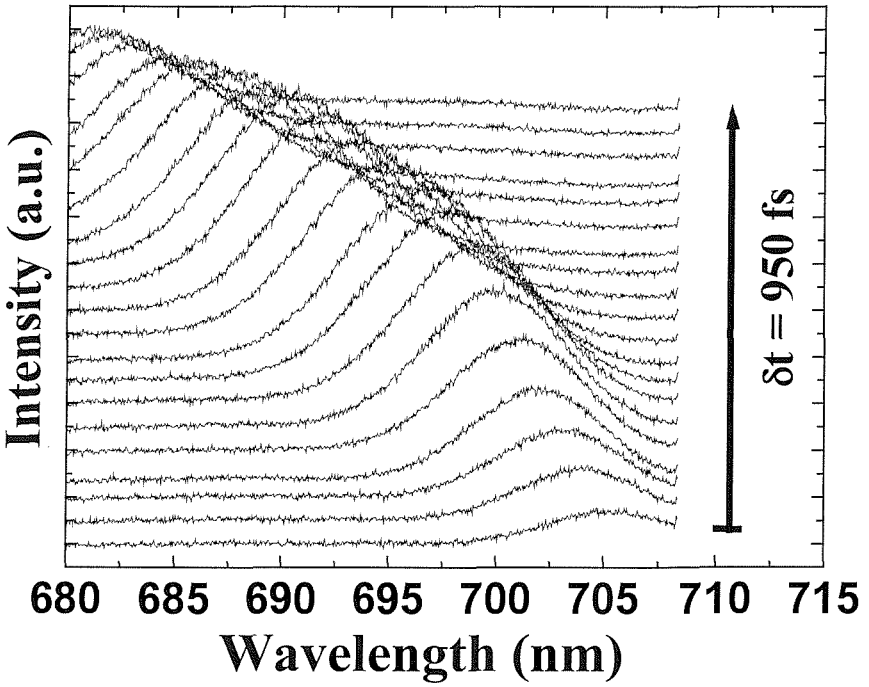

Fig. 4.5.2 The gated transmission spectra at each time delay.

The time of flight for the fundamental waveguide mode was obtained by subtracting the delay when sample is absent from the measured delay time, to eliminate the system dispersion. Figure 4.5.3 (black line) shows the time of flight versus wavelength for the fundamental TE mode propagating through the rib waveguide. The curve was extrapolated to λ=850 nm using a polynomial fit. The dispersion parameter (D), obtained from the differentiation of the time of flight with respect to wavelength, was also plotted (grey line). From this figure, it should be noted that the dispersion near wavelength λ= 800 nm, where the SPM measurement was performed, is small. The GVD (β_2) at λ=800nm was calculated from the following formula [12]:

$$\beta_2 = -\frac{D\lambda^2}{2\pi c} \tag{4.15}$$

which yields a value of 246 fs^2/cm with D=-0.7 (fs/nm cm) at λ=800 nm. With the GVD obtained from (4.15), the dispersion length was calculated (using eqn. (4.3)) to be L_D=104 cm, which is much larger than the sample length (L=1cm) indicating a negligible impact at λ=800nm. The hatched region shown in Fig. 4.5.3 is where the dispersion length L_D >10 cm. It clearly shows that the measured dispersion is well within the region, where GVD has a negligible impact, with wide tolerance. This result confirms the validity of the simplified theory used here for the estimation of the nonlinear refractive index.

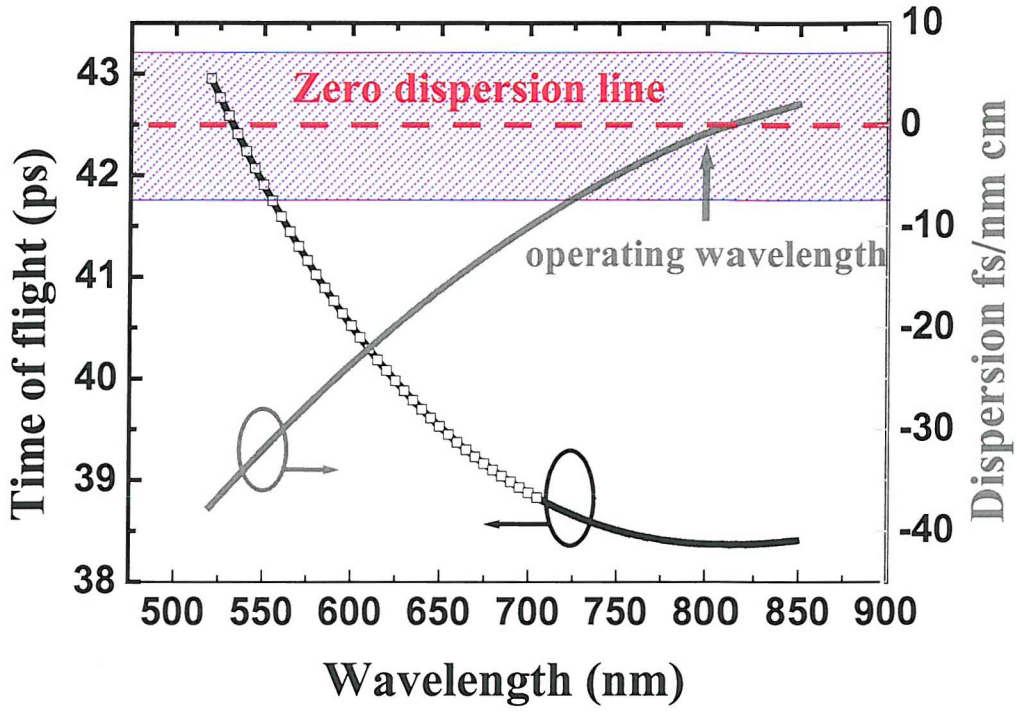

Fig. 4.5.3 Time-of-flight spectra (black line) and dispersion (grey line) for the fundamental TE mode. The hatched region shows where the dispersion length L_D is larger than 10 cm.

4.6 Conclusion.

This chapter demonstrates the measurement of the nonlinear refractive index of a Ta_2O_5 rib waveguide by directly monitoring the output spectra broadened by self phase modulation. Using a simplified theory which assumes that the group velocity dispersion has a negligible effect, the nonlinear refractive index was determined to be $n_2=(7.2\pm0.4)\times10^{-19}$ m^2/W, which is larger than the value of silica glass ($n_2\sim2.2\times10^{-20}$ m^2/W) by more than one order of magnitude. Femtosecond time of flight measurements based on a Kerr shutter configuration shows that the group

velocity dispersion has a negligible impact upon the spectral broadening within a 1-cm-long sample at λ=800nm, which confirms the validity and of the approximation used in the estimation.

Ta_2O_5 has the advantages of wide transparency in the telecommunication window and low toxicity in fabrication process. The wide material bandgap also promises a small two-photon absorption (TPA) effect. Moreover, the large value of n_2 in Ta_2O_5, in conjunction with its excellent compatibility with present silicon/silica processing technologies makes it being a more competitive and attractive candidate for compact, low-power, high-speed, and all-optical planar switching devices.

References

[1] B. P. Nelson, K. J. Blow, P. D. Constantine, N. J. Doran, J. K. Lucek, I. W. Marshall, and K. Smith, Electron. Lett., vol. **27**, 704 (1991).

[2] A. Samoc, M. Samoc, M. Woodruff, and B. Luther-Davies, Opt. Lett., vol. **20**, 1241 (1995).

[3] M. Asobe, I. Yokohama, T. Kaino, S. Tomaru, and T. Kurihara, Appl. Phys. Lett., vol. **67**, 891 (1995).

[4] Th. Gabler, R. Waldhäusl, A. Bräuer, F. Michelotti, H. –H. Hörhold, and U. Bartuch, Appl. Phys. Lett., vol. **70**, 928 (1997).

[5] Masaki Asobe, Ken'ichi Suzuki, Terutoshi Kanamori, and Ken'ichi Kubodera, Appl. Phys. Lett., vol. **60**, 1153 (1992).

[6] T. Kobayashi, *Nonlinear Optics of Organics and Semiconductors*, (Springer, Berlin, 1989).

[7] D. Marcuse, J. Lightwave Technol., vol. 9, 356 (1991).

[8] R. H. Stolen and C. Lin, Phys. Rev. A, vol. **17**, 1448 (1978).

[9] T. Kato, Y. Suetsugu, M. Takagi, E. Sasaoka, and M. Nishimura, Opt. Lett., vol. **20**, 988 (1995).

[10] M. Artiglia, E. Ciaramella, and B. Sordo, Electron. Lett., vol. **31**, 1012 (1995).

[11] L. Prigent and J. –P. Hamaide, IEEE Photon. Technol. Lett., vol. **5**, 1092 (1993).

[12] G P. Agrawal, *Nonlinear Fiber Optics,* (Academic, San Diego, 1989).

[13] R. S. Grant and W. Sibbett, Appl. Phys. Lett., vol. **58**, 1119 (1991).

[14] P. N. Kean, K. Smith, and W. Sibbett, IEE Proceedings, vol. **134**, 163 (1987).

[15] B. M. Foley, P. Melman, and K. T. Vo, Electron. Lett., vol. **28**, 584 (1992).

[16] J. Takeda, K. Nakajima, S. Kurita, S. Tomomoto, S. Saito, and T. Suemoto, Phys. Rev. B., vol. **62**, 10083 (2000).

[17] S. Kinoshita, H. Ozawa, Y. Kanematsu, I. Tanaka, N. Sugimoto, and S. Fujiwara, Rev. Sci. Instrum., vol. **71**, 3317 (2000).

[18] M. C. Netti, C. E. Finlayson, J. J. Baumberg, M. D. B. Charlton, M. E. Zoorob, J. S. Wilkinson, and G. J. Parker, Appl. Phys. Lett., vol. **81**, 3927 (2002).

Chapter 5 Hybrid integration of a self-assembled microsphere grating side-coupled to a Ta_2O_5 rib waveguide

5.1 Introduction

There is growing interest in integrating more functionality in planar lightwave circuits (PLCs). Wavelength selective devices are in particularly high demand due to their ability to provide filtering, routing and feedback, which are fundamental requirements for signal processing. Bragg gratings realised in planar waveguides date back to the early 1970's [1] and intensive research on distributed feedback structures has been pursued since then. Photosensitive [2][3] and etched relief gratings [4][5] are presently the most widely used structures. In comparison, relief gratings provide greater material flexibility because there is no requirement for photosensitivity. However, sub-micron scaled patterning and stringent etching tolerances are unavoidable for transferring patterns onto waveguides, resulting in high fabrication costs.

Recently, with processing techniques for producing mono-dispersed spherical colloids becoming mature, considerable research has been devoted to self-assembled photonic structures. Based on this simple and inexpensive technique, 3D photonic crystals have been fabricated [6][7]. Using a patterned substrate as a template, self-assembly has been tailored to fabricate more complex and well-defined structures [8][9].

To demonstrate the capability and powerful potential to make more functional and sophisticated planar devices, in this chapter, the hybrid integration of a self-assembled microsphere grating side-coupled to a Ta_2O_5 rib waveguide is described. Polystyrene has a refractive index of approximately 1.59, so that a higher index waveguide material was chosen (Ta_2O_5; $n \approx 2$) from which to form the rib waveguides. The great advantage of this configuration is that all the fabrication techniques employed are relatively simple, inexpensive and compatible with existing planar devices which makes this an attractive candidate for scaling up to more sophisticated PLCs. Furthermore, this technique provides a simple route to hybrid circuits combining microspheres in novel functional materials with waveguides in conventional materials.

This chapter was organized as follows: Section 5.2 describes the operation principles and the design considerations for the device. The fabrication process was detailed in section 5.3. Device characterizations was presented in section 5.4. The performance of the device including the Bragg wavelength, grating strength, and bandwidth were discussed in section 5.5. A summary is given in section 5.6.

5.2 Operational principles and device design considerations

When sub-micron polystyrene spheres are self-assembled to one side of a photolithographically-defined Ta_2O_5 rib waveguide, they may form a linear array. As a consequence, the optical field is drawn out resulting in a strengthened interaction with the spheres. The resultant periodic perturbation of the refractive

index experienced by the modal evanescent field leads to coupling to the backward-travelling mode at the Bragg wavelength. Fig. 5.2.1 schematically shows the concept. The waveguide was physically perturbed by the spheres and can be described in terms of the effective refractive index distributions.

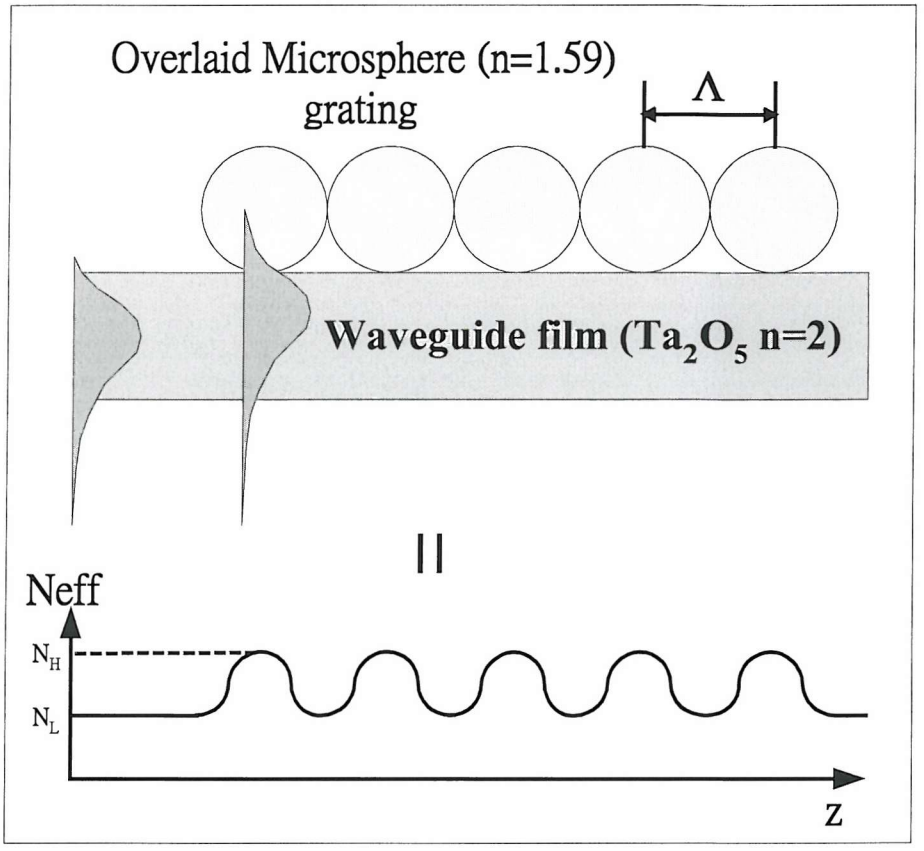

Fig. 5.2.1 Illustration of the operation concept of the self-assembled microsphere waveguide grating

According to the grating theory, the strongest interaction occurs for the fundamental Bragg order and the wavelength was determined by the effective index of the waveguide mode N_{eff} and the grating period Λ as:

$$\lambda_{Bragg} = 2N_{eff}\Lambda \quad (5.1)$$

Based on eqn. (5.1), a suspension of microspheres with diameter of ~500 nm was chosen in an attempt to get a resonant wavelength between 1550-1650 nm, assuming N_{eff} =1.55~1.65. The waveguide was designed to be single mode at the wavelength of operation (aiming at λ~1550 nm), to be sufficiently narrow to ensure that a significant proportion of the modal power travelled in the lateral evanescent region, and to have a sufficient height to trap the microspheres physically. Based on the results described in Chapter 2, a stripe waveguide with a width of 1 μm and a depth of 0.5μm fulfils these requirements.

5.3 Fabrication

A 500nm thick layer of tantalum pentoxide was first sputtered from a Ta_2O_5 target in an Ar/O_2 (16/6 sccm, 35 mTorr) atmosphere onto a Si wafer with a 2μm thick SiO_2 buffer layer, with the substrate held at 250°C. The film was then photolithographically patterned with stripes of photoresist of nominal width 1 μm, and argon ion beam milled to transfer the pattern into the Ta_2O_5 resulting in a rib waveguide with an etch depth of 500 nm, and a nominal width of approximately 1 μm. This process provides a waveguide as a patterned template for the following self- assembly process and is similar to that described in Chapter 2.

In preliminary work, microspheres were assembled on both sides of the waveguide, but this led to degradation in the effective strength of the grating due to

misalignment of the grating phases between the two sides. To avoid this problem, polystyrene spheres were intentionally assembled along only one side of the rib waveguide by first coating photoresist over one side of the waveguide. A fluidic cell was then assembled by sandwiching a ~0.5 mm thick gasket between the waveguide substrate and a cover glass. A suspension of mono-dispersed polystyrene spheres (1wt%, 499±5 nm in diameter, obtained from Brookhaven Ltd.) was then injected into the cell with a syringe. The sample was then placed vertically in a temperature-controlled incubator at 25°C, enabling the liquid slug which pushes the polystyrene spheres to sweep across the sample at a speed of 1.5 mm/h during the dewetting process. Once the spheres were physically trapped by the rib waveguide, the capillary immersion force (as shown in Fig. 5.3.1 (c)) forced the beads to adjust themselves into a well-packed array lined up along the waveguide. When the cell had dried, the sample was heated to 93°C for 1 minute in order to stick the polystyrene spheres to the surface of the waveguide. The remaining photoresist was then removed using 2-propanol, thereby lifting the microspheres away from one side of the rib. A microsphere array of approximately 3mm length was formed along the waveguide. Fig. 5.3.1 schematically shows the fabrication procedure. A scanning electron micrograph of part of the resultant device is shown in Fig. 5.3.2.

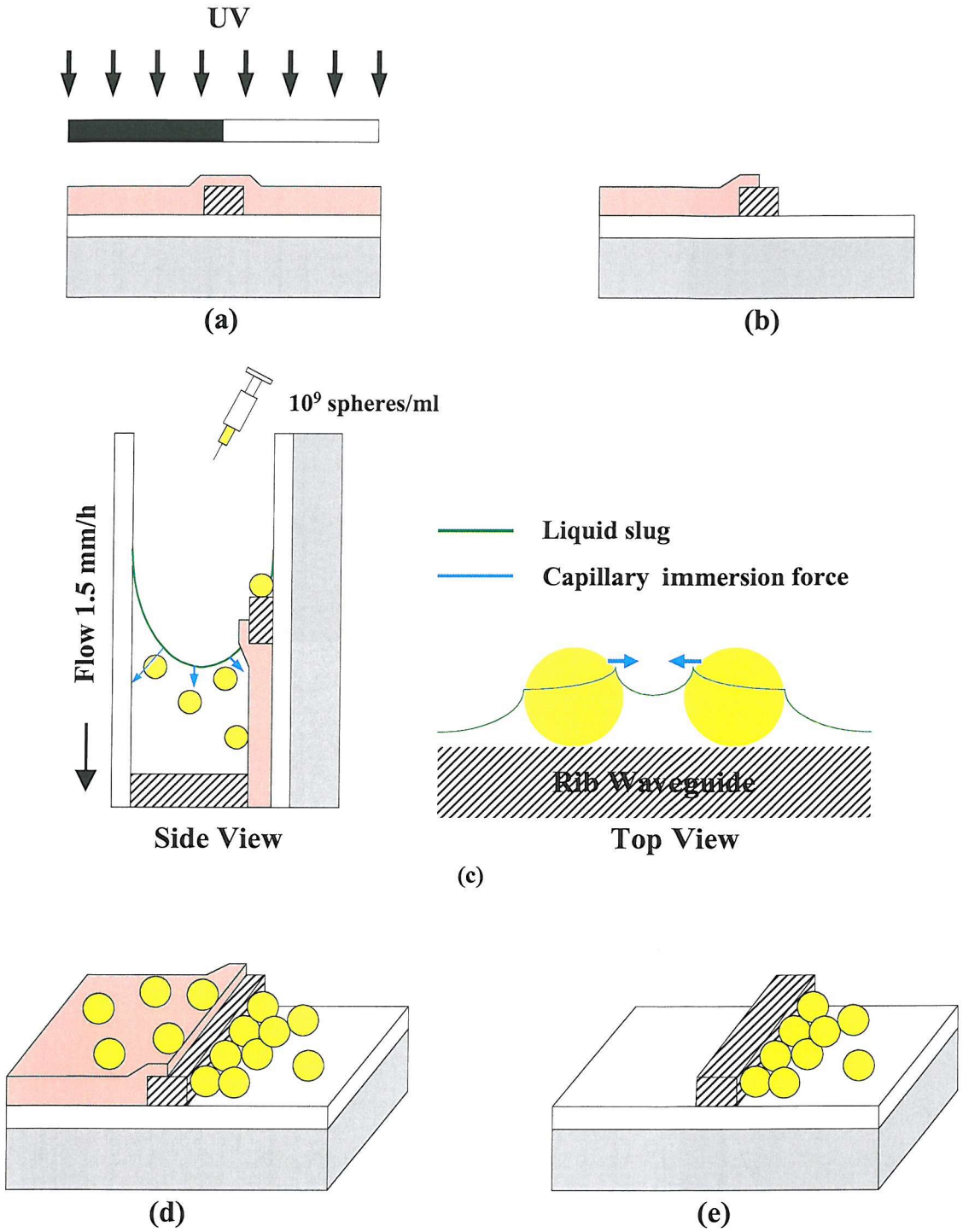

Fig. 5.3.1 Fabrication process of the self-assembled microsphere grating against the rib waveguide.

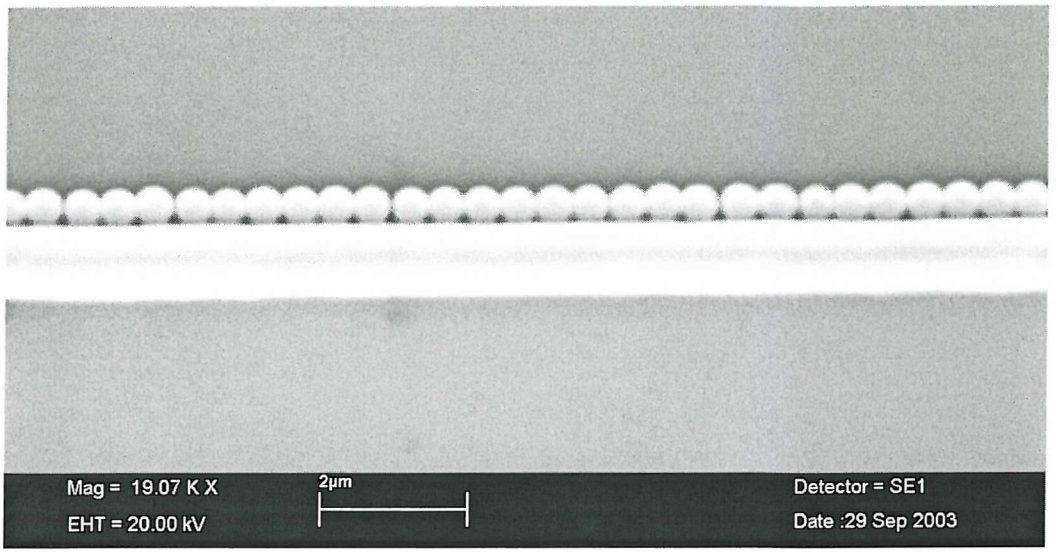

Fig. 5.3.2 SEM image of part of the microsphere grating.

The uniformity of the assembled microsphere grating was estimated by analyzing the SEM image. Fig. 5.3.3 shows the digitized intensity profile corresponding to the microsphere grating image shown in Fig. 5.3.2. The peak positions were marked with symbol "+" and were labeled with the corresponding positions.

Based on this figure, the periods can be calculated by subtracting the position values between adjacent peaks. The probability density (frequency) of the obtained periods can thereby be plotted, as shown in Fig.5.3.4. It is found that the histogram distributed in a Gaussian profile and accordingly, the microsphere grating has an average period Λ=491 nm, with standard deviation ±19 nm, corresponding to a maximum disorder 7.7%.

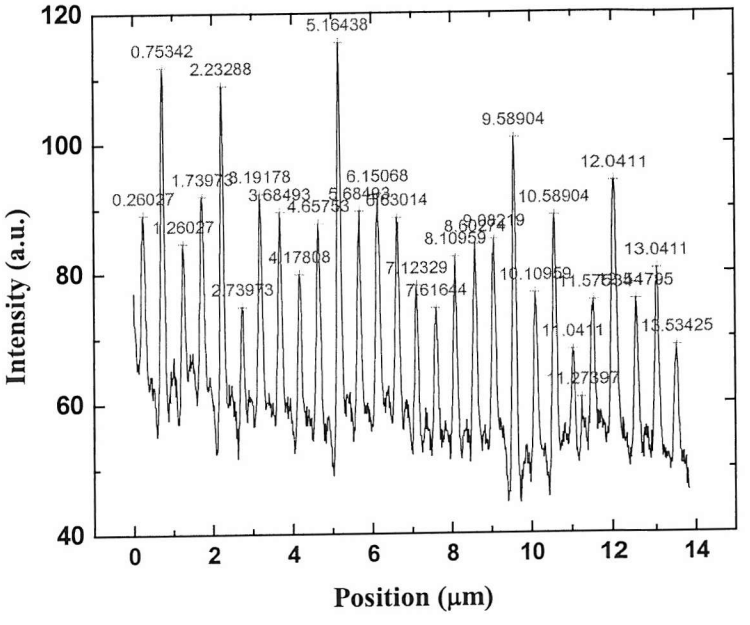

Fig. 5.3.3 The intensity profiles by digitizing the microsphere grating image in Fig. 5.3.2.

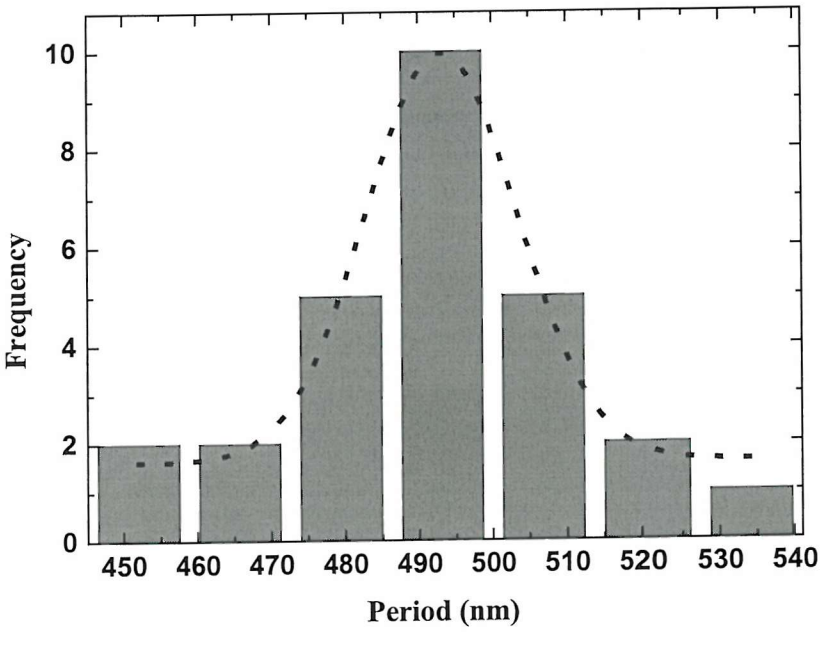

Fig. 5.3.4 The distribution of the inter-spacing between two adjacent spheres.

5.4 Characterization

The transmission spectrum of the sphere-waveguide coupled system was measured using the apparatus shown in Fig. 5.4.1. White light from a 150W tungsten lamp was chopped and end-fire launched into a single mode fibre using a 10× microscope objective lens. The fibre was then butt-coupled to the rib waveguide under investigation. The light emerging from the waveguide was collected using a 40× objective lens, passed through a monochromator onto an InGaAs detector, and the signal was fed into a lock-in amplifier and recorded on a computer.

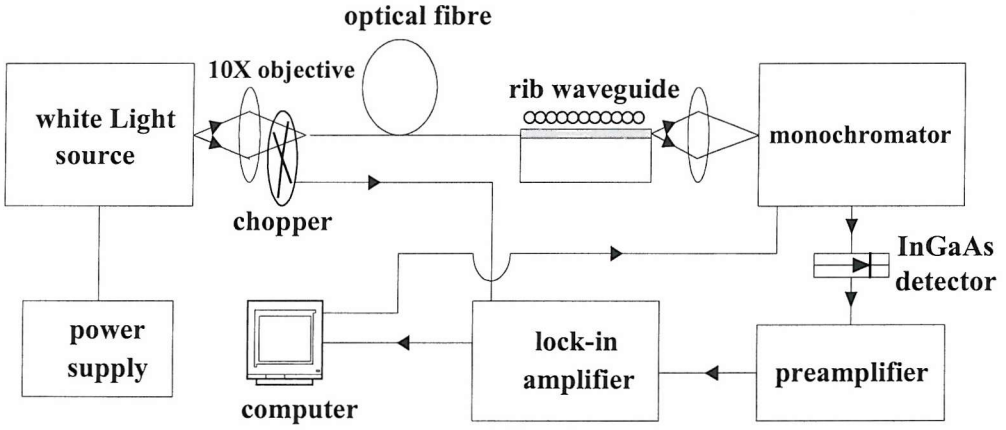

Fig. 5.4.1 Experimental arrangement for the transmission measurement.

Figure 5.4.2 shows the transmission spectra (TE polarized) for different cladding media (Air, n=1, and index matching oil, n=1.71), normalised to those obtained in the absence of spheres. When the device was surrounded by air, the transmission spectrum shows a notch centred at λ=1591 nm with a depth of approximately 1.47 dB (28%) and a bandwidth at full width at half maximum power ($\delta\lambda_{FWHM}$) of 17 nm. As the refractive index of the cladding medium increases to n=1.71 (index matching

oil), the centre of the stopband shifts to a longer wavelength of λ=1679 nm and exhibits a greater depth of 2.1 dB (38%) and a bandwidth $\delta\lambda_{FWHM}$ of 11nm.

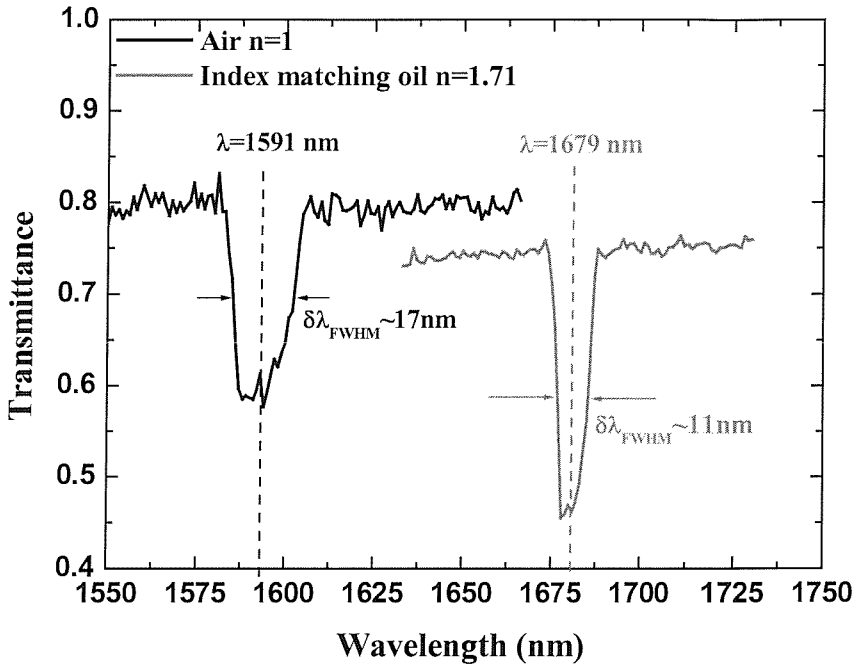

Fig. 5.4.2 Transmission spectra for cladding media of index 1.0 and 1.71.

5.5 Discussion

To explain the observed spectra, perturbation theory [10] was applied to the composite system shown in Fig. 5.5.1(a). The refractive index profile along the waveguide in the presence of the linear array of spheres can be represented by:

$$N(z)=N_{eff}+\eta(z)\Delta n \qquad (5.2)$$

where N_{eff} is the effective refractive index of the waveguide, $\Delta n=n_p-n_{clad}$ is the amplitude of perturbation, and η is the overlap integral between the evanescent field

and the polystyrene sphere at position z, defined by:

$$\eta(z) = \frac{\beta}{2\omega\mu} \int_{x1(z)}^{x2(z)} E^2(x)dx \tag{5.3}$$

where $\beta=N_{eff}\,k$, μ is the permeability, and $k=2\pi/\lambda$ is the propagation constant in vacuum. The evanescent field decays exponentially into the cladding medium with the form of:

$$E(x)=E_0\exp(-x/d) \tag{5.4}$$

where E_0 represents the field strength on waveguide surface and $d=(\lambda/2\pi)(N_{eff}^2-n_{clad}^2)^{-1/2}$ is the penetration depth, assuming the total integral power at current z position over a significant large cross-section is unity.

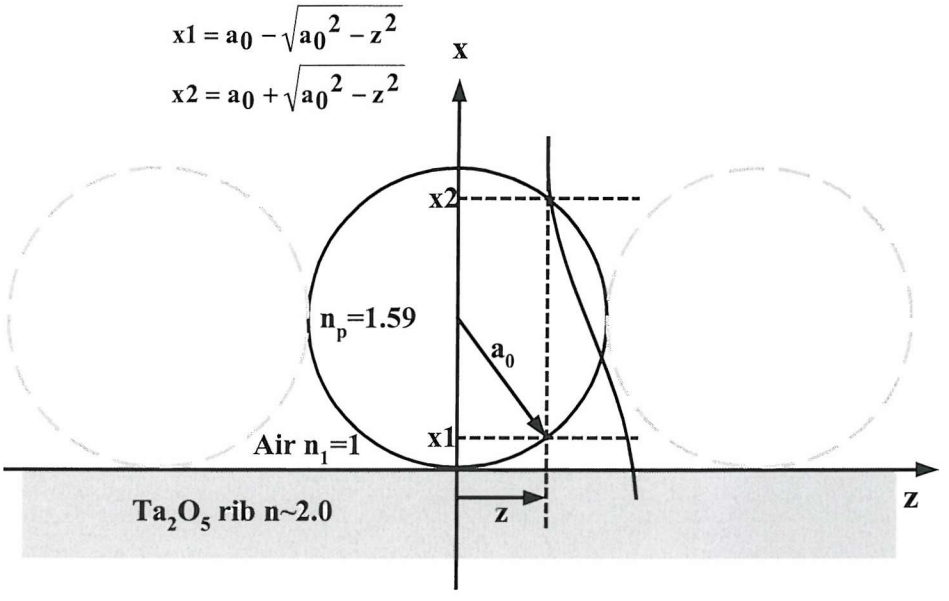

(a)

Fig. 5.5.1(a) Configuration of the microsphere grating side-coupled to the rib waveguide.

Substituting eqn.(5.4) in eqn.(5.3), the magnitude of perturbation can be derived:

$$\eta(z)\Delta n = \frac{\beta}{2\omega\mu}(E_0)^2 d\exp(-\frac{2a_0}{d})\mathrm{Sinh}\left[\frac{2a_0}{d}\sqrt{1-(\frac{z}{a_0})^2}\right]\Delta n \qquad (5.5)$$

Fig. 5.5.1(b) plots the periodically perturbed refractive index alongside the waveguide.

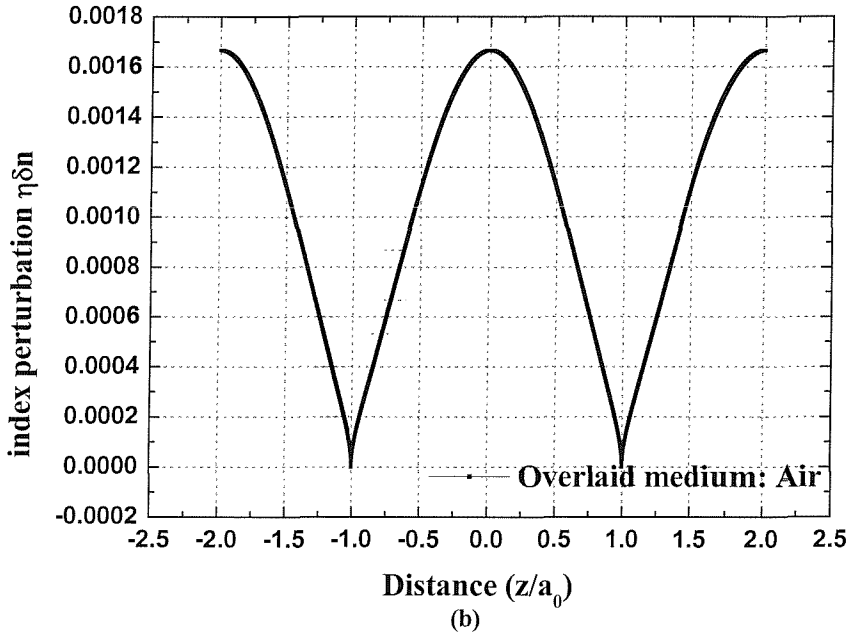

Fig. 5.5.1 (b) Calculated effective index perturbation along the waveguide.

As the index profile is an even function with respect to z=0, it can be expressed as a Fourier series:

$$\eta(z)\Delta n = \Delta n_0 + \sum_{m=1}^{s}\Delta n_m \cos\frac{m\pi}{a_0}z \qquad (5.6)$$

where

$$\Delta n_0 = \frac{1}{a_0}\int_0^{a_0}\eta(z)\Delta n\, dz \qquad (5.7)$$

$$\Delta n_m = \frac{2}{a_0}\int_0^{a_0}\eta(z)\Delta n\cos\frac{m\pi}{a_0}z dz \qquad (5.8)$$

The DC term Δn_0 contributes to the effective refractive index N_{eff}, causing the shift of Bragg wavelength. According to grating theory, the reflection wavelength is given by

$$\lambda_{Bragg} = 2(N_{eff}+\Delta n_0)\Lambda \tag{5.9}$$

where Λ is the grating period. The value of N_{eff} for the Ta_2O_5 rib waveguide here is determined by the finite-difference beam propagation method, assuming Ta_2O_5 has an index of 2.0. The grating period, Λ, estimated from the digitised SEM image is 491±19 nm. The Bragg reflection wavelength is numerically calculated and plotted as a function of cladding index in Fig. 5.5.2, with error bars indicating the effect of specified deviations in the particle size and the uncertainty in N_{eff}. The experimental data points are within the error bars showing agreement with theory.

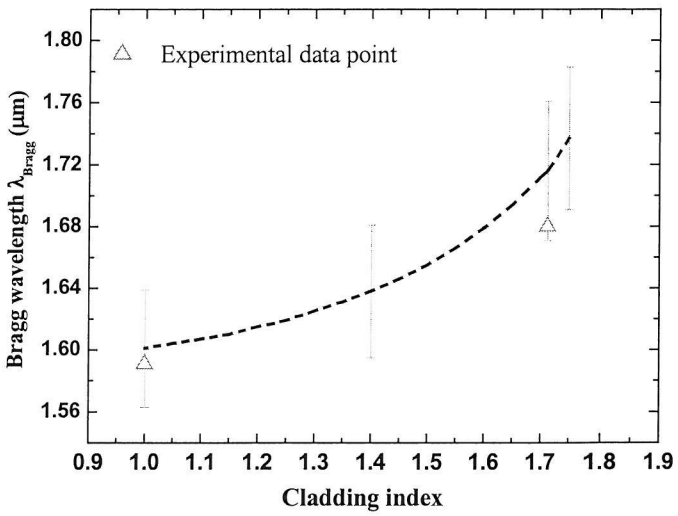

Fig. 5.5.2 Calculated and measured Bragg wavelength as a function of cladding index.

The strength of grating may be described by the coupling coefficient, which is defined as [11]

$$\kappa = (\pi\Delta n/\lambda_{Bragg})\eta \tag{5.10}$$

Fig. 5.5.3 shows the numerically-determined coupling coefficient as a function of cladding index. From this diagram it is expected that, as the cladding index increases from unity, the strength of the interaction first increases slightly. Then, as the cladding index approaches that of the spheres, n_p=1.59, the reduced sphere/cladding index contrast becomes more significant than the increasing overlap between the evanescent field and the spheres, and the coupling coefficient falls. When the cladding index becomes larger than n_p=1.59, the coupling coefficient rises rapidly, due to a combination of increasing index contrast and extending field. In the experiment presented here, the deeper transmission notch at the Bragg wavelength in the case of the oil cladding demonstrates this behaviour. The transmission drop, enhanced by a factor of R=1.38 (from 28% to 38%), agrees qualitatively with the enhanced coupling coefficient ($\kappa_{oil}/\kappa_{air}$=1.35), which results in this enhancement via $R = \frac{\tanh^2(\kappa_{oil} L)}{\tanh^2(\kappa_{air} L)}$.

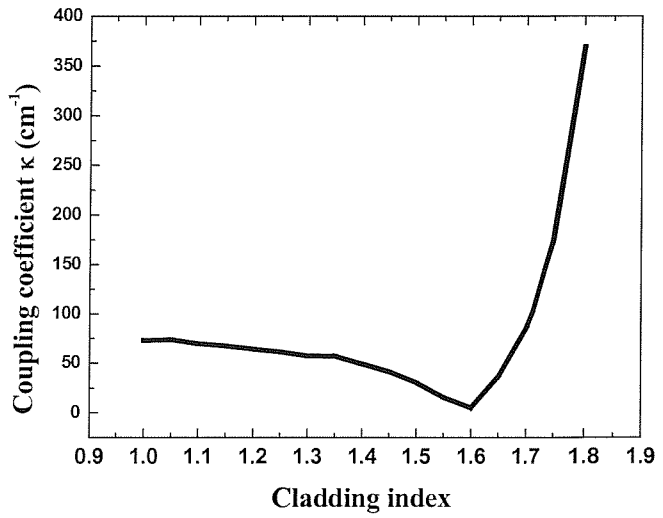

Fig. 5.5.3 Calculated coupling coefficient as a function of cladding index.

The bandwidths of the spectral notches are much greater than would be expected from a weak uniform grating of 3mm length. However, this is a randomly perturbed periodic system [12][13] and the deviation in the diameters of the spheres, imperfections in the periodicity of the packing and imperfections in the rib waveguide will contribute to this broadening and will also cause a reduction in the depth of the transmission notch. It is expected that with improved sphere diameter control and more uniform assembly, a deeper and narrower response will be achieved.

To further improve the uniformity of the self-assembled microsphere gratings, the holographically-generated optical trap could potentially be employed. Periodic intensity patterns are generated by intersecting multiple optical beams and have been demonstrated to induce ordering in colloidal monolayers [14]. This physical method has great promise for dynamically controlling and adjusting the microsphere array to reduce dislocations and vacancies. On the other hand, a chemically patterned substrate provides another possible route for the uniformity improvement. It has been demonstrated that colloidal particles can be selectively deposited on a chemically modified area of the substrate [15]. The polystyrene spheres used in this study are slightly negative charged particles, which may be immobilized on a chemically patterned cationic region. This chemical method has great advantage for preferentially density control, providing a possible route to improve the uniformity. In both approaches, it is notable that the rib waveguide may be used as a test bed, for in-situ interrogation of the self-assembly process through

transmittance measurement.

5.6 Conclusion

This chapter demonstrates a side-coupled rib waveguide microsphere grating using a simple low-cost self-assembly process. The optical coupling between the lateral evanescent field and the self-assembled array results in a stopband in the transmission spectrum, at a wavelength of $\lambda \approx 1590$nm, in close agreement with theory. Grating strength adjustment has been examined by varying the refractive index of the overlaid cladding medium, and an extinction of 38% has been obtained. This study demonstrates the potential for self-assembly of microspheres with waveguides for wavelength-dependent devices, and it is expected that this may be extended to microspheres and microsphere resonators of other materials or as part of more sophisticated planar lightwave circuit configurations.

References

[1] D. C. Flanders, H. Kogelnik, R. V. Schmidt, and C. V. Shank, Appl. Phys. Lett., vol. **24**, 194, (1974).

[2] M. Ibsen, J. Hubner, J. E. Pedersen, R. Kromann, L. –U. A. Andersen, and M. Kristensen, Electron. Lett., vol. **35**, 585, (1996).

[3] D. F. Geragthy, D. Provenzano, W. K. Marshall, S. Honkanen, A. Yariv, and N. Peyghambarian, Electron. Lett., vol. **35**, 585, (1999).

[4] J. E. Román and K. A. Winick, Appl. Phys. Lett., vol. **61**, 2744, (1992).

[5] R. Adar, C. H. Henry, R. C. Kistler, and R. F. Kazarinov, Appl. Phys. Lett., vol. **60**, 1779, (1992).

[6] I. I. Tarhan, and G. H. Watson, Phys. Rev. Lett., vol. **76**, 315 (1996).

[7] Yurii A. Vlasov, Xiang-Zheng Bo, James C. Sturm, and David J. Norris, Nature, vol. **414**, 289 (2001).

[8] Y. –H. Ye, S. Badilescu, Vo-Van Truong, P. Rochon, and A. Natansohn, Appl. Phys. Lett., vol. **79**, 872 (2001).

[9] Yadong Yin, Yu Lu, Byron Gates, and Younan Xia, J. Am. Chem. Soc., vol. **123**, 8718 (2001).

[10] A. W. Snyder and J. D. Love, *Optical Waveguide Theory*, Chapman and Hall, London, pp. 374-380 (1983).

[11] I. Bennion, J. A. R. Williams, L. Zhang, K. Sugden, and N. J. Doran, Opt. Quantum. Electron., vol. **28**, 93 (1996).

[12] Jean Marc Frigerio, Josette Rivory, and Ping Sheng, Opt. Comm., vol. **98**, 231 (1993).

[13] Daozhong Zhang, Zhaolin Li, Wei Hu, and Bingying Cheng, Appl. Phys. Lett., vol. **67**, 2431 (1995).

[14] R. L. Eriksen, P. C. Mogensen, and J. Glückstad, Opt. Lett., vol. **27**, 267 (2002).

[15] J. Aizenberg, P. V. Braun, and P. Wiltzius, Phys. Rev. Lett., vol. **84**, 2997 (2000).

Chapter 6 Embedded photonic crystal structures in Ta_2O_5 rib waveguides

6.1 Introduction

In 1987, Eli Yablonovitch introduced the idea that spontaneous emission can be suppressed when a three-dimensional periodic dielectric structure has an electromagnetic band gap which overlaps the electronic band edge [1]. In the same year, Sajeev John proposed that strong localization of photons may occur in certain superlattice microstructures due to multiple scattering and interference [2]. These two remarkable breakthroughs led to the concept of the "photonic band gap" which is analogous to the electronic band gap in solid state physics.

The photonic band gap (PBG) is a range of frequencies within which propagation of a specific wavelength is blocked, and light is reflected. A complete PBG occurs when light within a band of frequencies cannot propagate whatever the polarization or the direction of propagation is. A PBG may be formed by creating periodic refractive index variations in a structure. Structures like this are known as photonic band gap materials or photonic crystals (PCs). In the past, much effort has been devoted to studying the influence of different lattice arrangements and index contrast [3] on band gaps. As a general rule, the bigger the index contrast, the wider the band gap. A complete PBG is achieved when a band gap exists for all angles of incidence for some range of frequencies. This favours the lattice arrangement when the corresponding Brillouin zone has the most spherical shape [1]. As a

consequence, the hexagonal lattice arrangement in 2D and face centred cubic (fcc) or diamond structures [4,5] in 3D are most likely to create complete band gaps. In addition, it has been proposed that some quasicrystal structures [6,7] raise the order of symmetry further, resulting in a complete PBG even with low index contrast.

Since the convincing demonstration of "Yablonovite" [5] ten years ago, PBG materials have attracted the intense attention of the photonics community. Their ability to control the flow of light and their capability to concentrate light and enhance light-matter interactions have inspired many novel discoveries. Based on strong confinement, sharp bends [8-10] and low crosstalk between adjacent channels [11] have been demonstrated. These properties make photonic crystals a promising platform for miniaturised integrated optical circuits. Combining a variety of components based on photonic crystals, very dense photonic circuits can be realized in a length scale of several tens of microns. In addition to making 1D line defects in an otherwise perfect photonic crystal, very high-Q, small volume microcavities can be made by introducing point defects [12-14]. Defects admit the existence of localized modes within a very narrow frequency band. This property makes photonic crystals very attractive candidates for devices such as frequency-selective mirrors, band-pass filters and high-Q resonant cavities. The ability to control spontaneous emission and enhance light-matter interaction in a small volume is considered especially important in developing novel light sources. The possibility of realizing a low-threshold laser [15] and high extraction-efficiency light emitting diode (LED) [1] was suggested several years ago. Recently, a 2D

photonic crystal defect laser [16] and a LED [17] with 6-fold photoluminescence enhancement have been demonstrated.

Apart from strong confinement, low group velocity at the band edge and high dispersion are also important features of photonic crystals. A low group velocity implies a long optical path in the structure. If an active medium is introduced into a photonic crystal, optical gain can be enhanced. Intriguing phenomena including enhanced light amplification [18-20], photonic band edge lasers [21] and optical delay elements [22] have been investigated. Besides, dispersion properties not only render photonic crystals useful for pulse compression [23] but also for wavelength separation. The superprism phenomenon [24], where the angular dispersion of light is 500 times stronger than that in a conventional prism, was demonstrated recently. The light path in the photonic crystal is deflected over a broad angular range with only a slight change in the incident light angle or wavelength. This property makes it promising for application to a photonic crystal based WDM device [25].

Undoubtedly, photonic crystals are beginning to play an important role in modern optics. Benefiting from their novel properties, it is widely believed that photonic crystals will revolutionise fields such as photonics, quantum optics, semiconductor technology, and laser physics. However, there are still several issues to be overcome before photonic crystals can be applied in practice. In this chapter, a prototype of photonic crystal is fabricated embedded in a Ta_2O_5 rib waveguide and some of the fundamental properties are discussed. In section 6.2, two computational methods

are introduced to model the band structures and transmission spectra of photonic crystals. Both of them are applied to known systems in the literature to confirm their validity. In section 6.3, the fabrication of embedded photonic crystals in Ta_2O_5 rib waveguides is described. In section 6.4, the measurement of the transmission spectrum for the corresponding photonic crystal structure is presented. Different computational schemes are utilized to calculate the transmission spectrum and the results are compared with the experimental data. In section 6.5, a brief conclusion is given.

6.2 Theoretical modeling methods

In this section, three computational schemes are introduced. For the calculation of photonic band structures, the plane wave expansion method (PWE) is used due to its straightforwardness and simplicity. Since plane waves form a complete set, any field distributions can be expressed as a linear combination of them. By expanding the dielectric function and the field pattern on the basis of plane waves, Maxwell's equations can be reduced into a set of linear equations, forming a typical Hermitian eigenvalue problem. The variational principle can then be utilized to find the eigenvalues and yield the corresponding eigenvectors.

For calculating the transmission spectrum, the transfer matrix method (TMM) and the finite-difference time-domain (FDTD) are used. The TMM expresses the electromagnetic field at a given plane in terms of the electromagnetic field at the previous plane, via a transfer matrix. The great advantage of this method is that once the initial electromagnetic field has been defined, the field at successive planes

of a structure can be deduced by sequentially multiplying the transfer matrix. The FDTD is the analogue of the TMM in time domain. A given refractive index distribution was discretised based on a space-time mesh and Maxwell's equations are solved successively through those grid points.

6.2.1 Plane wave expansion (PWE) method

The propagation of electromagnetic waves is governed by Maxwell's equations which place no limitation on mixed media such as photonic crystals. To maintain simplicity without losing physical insight, it is assumed that all materials comprising the photonic crystal are linear, lossless, isotropic, and have a negligible frequency dependence of the dielectric constant. Consequently, Maxwell's equations can be written in the following form:

$$\nabla \cdot \mathbf{E}(\mathbf{r},t) = 0 \tag{6.1}$$

$$\nabla \cdot \mathbf{H}(\mathbf{r},t) = 0 \tag{6.2}$$

$$\nabla \times \mathbf{E}(\mathbf{r},t) = -\mu_0 \frac{\partial \mathbf{H}(\mathbf{r},t)}{\partial t} \tag{6.3}$$

$$\nabla \times \mathbf{H}(\mathbf{r},t) = \varepsilon_0 \varepsilon(\mathbf{r}) \frac{\partial \mathbf{E}(\mathbf{r},t)}{\partial t} \tag{6.4}$$

Assuming the electromagnetic field has a sinusoidal time dependence, the electric and magnetic fields can be expressed as:

$$\mathbf{E}(\mathbf{r},t) = \mathbf{E}(\mathbf{r})\exp(-i\omega t) \tag{6.5}$$

$$\mathbf{H}(\mathbf{r},t) = \mathbf{H}(\mathbf{r})\exp(-i\omega t) \tag{6.6}$$

Taking the curl of equation (6.4) and eliminating $\mathbf{E}(\mathbf{r})$ using equation (6.3) with $1/\sqrt{\varepsilon_0\mu_0} = c$, the vector Helmholtz equation, containing only the magnetic field $\mathbf{H}(\mathbf{r})$ can be derived:

$$\nabla \times \left(\frac{1}{\varepsilon(\mathbf{r})} \nabla \times \mathbf{H}(\mathbf{r}) \right) = \left(\frac{\omega}{c}\right)^2 \mathbf{H}(\mathbf{r}) \tag{6.7}$$

In the literature, particularly that regarding photonic crystals, this equation is generally termed as the master equation. Since the dielectric constant of a photonic crystal has discrete periodicity, the field pattern can be expanded into a set of plane waves. Following the notation used in [26] and adapting Bloch's form:

$$\mathbf{H}_{\omega}^{\mathbf{k}}(\mathbf{r}) = \sum_{\mathbf{G}} \sum_{\lambda=1,2} h_{\mathbf{G},\lambda} \hat{\mathbf{e}}_{\lambda} \exp[i(\mathbf{k}+\mathbf{G})\cdot\mathbf{r}] \tag{6.8}$$

where **G** is the reciprocal lattice vector of the crystal, **k** is the wave vector in the Brillouin zone, $h_{\mathbf{G},\lambda}$ is the coefficient of the plane wave, and $\hat{\mathbf{e}}_{\lambda}$, indexed by the label λ, denotes the unit vector of the two polarizations orthogonal to (**k**+**G**) in order to fulfill the transversality requirement in equation (6.2).

Similarly, the inverse of $\varepsilon(\mathbf{r})$ is also a periodic function and can be expanded into plane waves with wave vector (**G**′-**G**) as

$$\frac{1}{\varepsilon(\mathbf{r})} = \sum_{\mathbf{G}',\mathbf{G}} \varepsilon_{\mathbf{G},\mathbf{G}'}^{-1} \exp[i(\mathbf{G}-\mathbf{G}')\cdot\mathbf{r}] \tag{6.9}$$

where $\varepsilon_{\mathbf{G},\mathbf{G}'}^{-1}$ is the Fourier transform of the inverse of the dielectric function. Substituting equation (6.8) and equation (6.9) into the master equation (6.7) and after a lengthy simplification process, the master equation can be converted into a matrix eigenvalue equation:

$$\sum_{\mathbf{G}'} \sum_{\lambda'=1}^{2} \Theta_{(\mathbf{G},\lambda)(\mathbf{G},\lambda)'}^{\mathbf{k}} h_{(\mathbf{G},\lambda)'} = \left(\frac{\omega}{c}\right)^2 h_{(\mathbf{G},\lambda)} \tag{6.10}$$

where

$$\Theta_{(\mathbf{G},\lambda)(\mathbf{G}',\lambda)}^{\mathbf{k}} = [(\mathbf{k}+\mathbf{G})\times\hat{\mathbf{e}}_{\lambda}]\cdot[(\mathbf{k}+\mathbf{G}')\times\hat{\mathbf{e}}_{\lambda'}]\varepsilon_{\mathbf{G},\mathbf{G}'}^{-1} \tag{6.11}$$

Many numerical techniques [27] are available to solve equation (6.10). In this study,

the electromagnetic variational theorem is applied to solve the eigenvalue ω for each required value of the wavevector **k** [26]. Since the operator Θ defined in (6.11) is Hermitian, according to the theory the function which minimizes the variational energy E is the eigenmode with minimum frequency ω_0, where E is:

$$E = \frac{\sum_{(G,\lambda)'}\sum_{(G,\lambda)} h_{(G,\lambda)}{}^{*}\Theta^{k}_{(\mathbf{G},\lambda),(\mathbf{G},\lambda)'}h_{(\mathbf{G},\lambda)'}}{\sum_{(\mathbf{G},\lambda)} h_{(\mathbf{G},\lambda)}{}^{*}h_{(\mathbf{G},\lambda)'}} \tag{6.12}$$

By successively minimizing E, and orthogonalising the eigenmode to the one obtained previously, all of the eigenvalues ω_n (labeled by the band number in order of increasing frequency) can be obtained for a given value of **k**. Scanning the values of wavevector **k** in the first Brillouin zone (1BZ) of the reciprocal lattice, the set of solutions $\omega_n(\mathbf{k})$ subject to a fixed value n constitute a band. The band structure can thus be built up by collecting bands with different n values. In this thesis, Bandsolve™ was used to calculate the band structures for the fabricated PCs.

6.2.2 PWE applied to known structures

To test the validity of the PWE introduced here, it was applied to the known structure reported in Ref. [28]. The structure has a 2D triangular lattice of air columns embedded in a dielectric material (ϵ_d=13). The radius of the air column is r=0.48a, where a is the lattice constant. The calculated band structure along the three symmetric directions in the BZ was plotted in Fig. 6.2.1, which reproduces Fig. 1 in [28], showing the validity of the program for applying it to the calculation of the band structure for 2D photonic crystals.

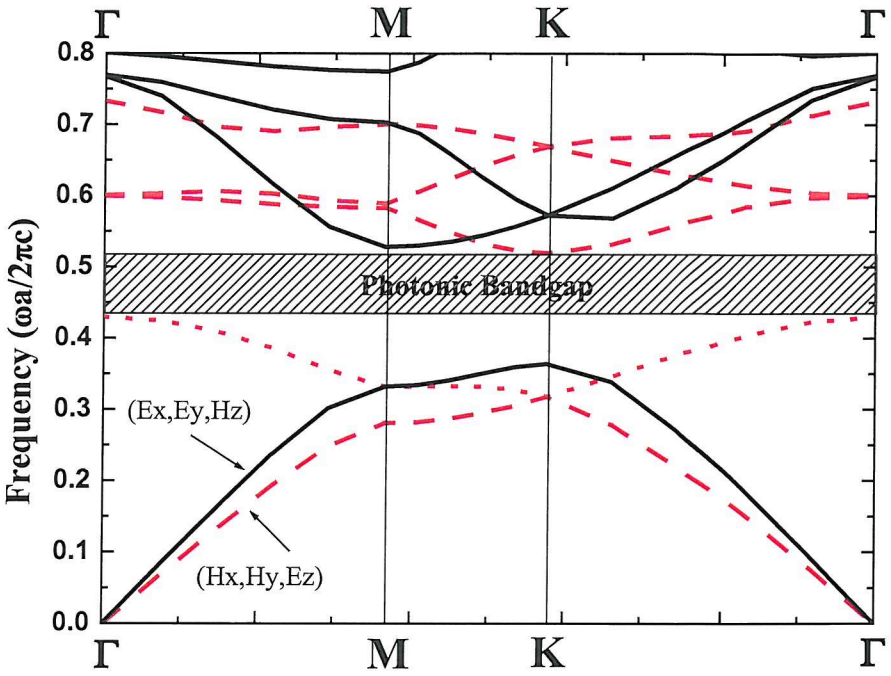

Fig. 6.2.1 Band structures simulated by PWE for the structure reported in Ref. [28]

6.2.3 Transfer matrix method (TMM)

The transfer matrix method (TMM) was used to calculate the transmission spectra of photonic crystal waveguides. The TMM is a numerical method that originated from the theoretical treatment of low-energy electron diffraction experiments [29]. Pendry [30] extended it further and applied the TMM to calculate photonic band structures of periodic dielectrics.

As the term suggests, the TMM expresses the electromagnetic field at a given plane in terms of the electromagnetic field at the previous plane, via a transfer matrix. Once the initial electromagnetic field has been defined at the z=0 plane, the

throughput field at the z=c plane can be calculated by successive matrix multiplications. In other words, the principle of the method is to build up a simple algebraic relationship which relates the field at one plane to another. To accomplish this, a procedure based on the shift property of Fourier transformation was utilized. A positional shift in real space corresponds to a modulation in k space. The following illustrates the calculation process based on Pendry's work [30] and shows how Maxwell's equations were transformed into a set of difference equations.

The first step is to sample the structure intended for study with a mesh. As shown in Fig. 6.2.2, the guiding layer was divided into slabs. Each slab can be further divided into grids with a unit cell area a×b.

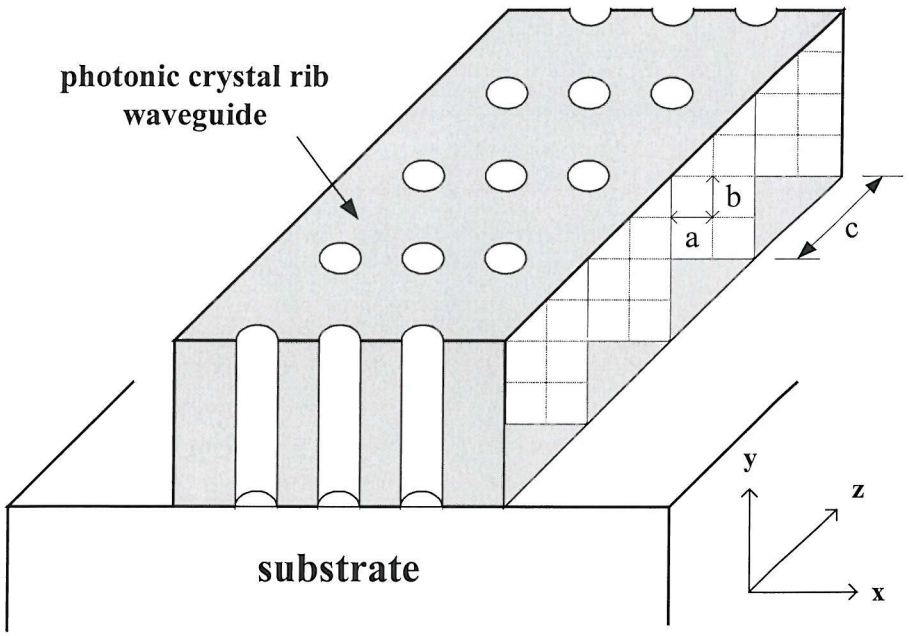

Fig. 6.2.2 The slabs and meshes which are used to discretize the electromagnetic fields.

The second step is to discretize Maxwell's equations on the mesh.

$$\nabla \times \mathbf{E}(\mathbf{r},t) = -\frac{\partial \mathbf{B}(\mathbf{r},t)}{\partial t} \tag{6.13}$$

$$\nabla \times \mathbf{H}(\mathbf{r},t) = \frac{\partial \mathbf{D}(\mathbf{r},t)}{\partial t} \tag{6.14}$$

For the transmission coefficient calculation, the TMM adopts a finite difference frequency domain (FDFD) approach. Therefore, Eq. (6.13) and (6.14) were first transformed into k space and led to the following equations:

$$\mathbf{k} \times \mathbf{E}(\mathbf{k},\omega) = \omega \mathbf{B}(\mathbf{k},\omega) \tag{6.15}$$

$$\mathbf{k} \times \mathbf{H}(\mathbf{k},\omega) = -\omega \mathbf{D}(\mathbf{k},\omega) \tag{6.16}$$

(6.15) and (6.16) can be rewritten using the three orthogonal components in Cartesian coordinate and yields:

$$\begin{aligned} k_yE_z\text{-}k_zE_y&=\omega B_x \\ k_zE_x\text{-}k_xE_z&=\omega B_y \\ k_xE_y\text{-}k_yE_x&=\omega B_z \end{aligned} \tag{6.17}$$

$$\begin{aligned} k_yH_z\text{-}k_zH_y&=\text{-}\omega D_x \\ k_zH_x\text{-}k_xH_z&=\text{-}\omega D_y \\ k_xH_y\text{-}k_yH_x&=\text{-}\omega Dz \end{aligned} \tag{6.18}$$

With the help of the following Taylor expansions:

$$\begin{aligned} \exp(ik_x a) &= 1+\frac{(ik_x a)}{1!}+\frac{(ik_x a)^2}{2!}+\cdots\cdots \\ \exp(ik_y b) &= 1+\frac{(ik_y b)}{1!}+\frac{(ik_y b)^2}{2!}+\cdots\cdots \\ \exp(ik_z c) &= 1+\frac{(ik_z c)}{1!}+\frac{(ik_z c)^2}{2!}+\cdots\cdots. \end{aligned} \tag{6.19}$$

and ignoring the terms higher than second order, the wave vector k_x, k_y and k_z in

(6.17) can be approximated by:

$$k_x \sim (ia)^{-1}[\exp(ik_x a)-1]$$
$$k_y \sim (ib)^{-1}[\exp(ik_y b)-1] \qquad (6.20)$$
$$k_z \sim (ic)^{-1}[\exp(ik_z c)-1]$$

Similarly, the wave vector k_x, k_y and k_z in equation (6.18) can be approximated by:

$$k_x \sim (-ia)^{-1}[\exp(-ik_x a)-1]$$
$$k_y \sim (-ib)^{-1}[\exp(-ik_y b)-1] \qquad (6.21)$$
$$k_z \sim (-ic)^{-1}[\exp(-ik_z c)-1]$$

Substituting (6.20), (6.21) into (6.17), (6.18) results in:

$$\frac{1}{ib}[\exp(ik_y b)-1]E_z - \frac{1}{ic}[\exp(ik_z c)-1]E_y = \omega B_x$$
$$\frac{1}{ic}[\exp(ik_z c)-1]E_x - \frac{1}{ia}[\exp(ik_x a)-1]E_z = \omega B_y \qquad (6.22)$$
$$\frac{1}{ia}[\exp(ik_x a)-1]E_y - \frac{1}{ib}[\exp(ik_y b)-1]E_x = \omega B_z$$

$$-\frac{1}{ib}[\exp(-ik_y b)-1]H_z + \frac{1}{ic}[\exp(-ik_z c)-1]H_y = -\omega D_x$$
$$-\frac{1}{ic}[\exp(-ik_z c)-1]H_x + \frac{1}{ia}[\exp(-ik_x a)-1]H_z = -\omega D_y \qquad (6.23)$$
$$-\frac{1}{ia}[\exp(-ik_x a)-1]H_y + \frac{1}{ib}[\exp(-ik_y b)-1]H_x = -\omega D_z$$

Using the shift property of Fourier transformation defined by:

$$\Im\{g(x-a, y-b, z-c)\} = G(k_x, k_y, k_z)\exp[-i2\pi(k_x a + k_y b + k_z c)] \qquad (6.24)$$

And Fourier transform (6.22), (6.23) yields the following real space difference equations:

$$(ib)^{-1}[E_z(\mathbf{r}+b)-E_z(\mathbf{r})]-(ic)^{-1}[E_y(\mathbf{r}+c)-E_y(\mathbf{r})]=\omega B_x(\mathbf{r}) \quad (6.25a)$$

$$(ic)^{-1}[E_x(\mathbf{r}+c)-E_x(\mathbf{r})]-(ia)^{-1}[E_z(\mathbf{r}+a)-E_z(\mathbf{r})]=\omega B_y(\mathbf{r}) \quad (6.25b)$$

$$(ia)^{-1}[E_y(\mathbf{r}+a)-E_y(\mathbf{r})]-(ib)^{-1}[E_x(\mathbf{r}+b)-E_x(\mathbf{r})]=\omega B_z(\mathbf{r}) \quad (6.25c)$$

$$-(ib)^{-1}[H_z(\mathbf{r}-b)-H_z(\mathbf{r})]-(ic)^{-1}[H_y(\mathbf{r}-c)-H_y(\mathbf{r})]=-\omega D_x(\mathbf{r}) \quad (6.26a)$$

$$-(ic)^{-1}[H_x(\mathbf{r}-c)-H_x(\mathbf{r})]-(ia)^{-1}[H_z(\mathbf{r}-a)-H_z(\mathbf{r})]=\omega D_y(\mathbf{r}) \quad (6.26b)$$

$$-(ia)^{-1}[H_y(\mathbf{r}-a)-H_y(\mathbf{r})]-(ib)^{-1}[H_x(\mathbf{r}-b)-H_x(\mathbf{r})]=\omega D_z(\mathbf{r}) \quad (6.26c)$$

All the unknown quantities (3 components of the E-field and 3 components of the H-field) can be derived from equations (6.25) and (6.26).

Introducing the following expressions:

$$\mathbf{D}(\mathbf{r})=\epsilon_0\epsilon(\mathbf{r})\mathbf{E}(\mathbf{r})$$

$$\mathbf{B}(\mathbf{r})=\mu_0\mu(\mathbf{r})\mathbf{H}(\mathbf{r})$$

$$c_0^2=(\epsilon_0\mu_0)$$

$$\mathbf{H}' = \frac{i}{c\omega\varepsilon_0}\mathbf{H}$$

The four transverse components E_x, E_y, H_x, H_y can be deduced from the two longitudinal components E_z, H_z in (6.25c) and (6.26c) and simplified into the following equations:

$$E_x(\mathbf{r}+c) = E_x(\mathbf{r}) + \frac{c^2\omega^2}{c_0^2}\mu(\mathbf{r})H'_y(\mathbf{r})$$

$$+\frac{c^2}{a\varepsilon(\mathbf{r})}\left[\frac{H'_y(\mathbf{r}-a)-H'_y(\mathbf{r})}{a}-\frac{H'_x(\mathbf{r}-b)-H'_x(\mathbf{r})}{b}\right]$$

$$-\frac{c^2}{a\varepsilon(\mathbf{r}+a)}\left[\frac{H'_y(\mathbf{r})-H'_y(\mathbf{r}+a)}{a}-\frac{H'_x(\mathbf{r}+a-b)-H'_x(\mathbf{r}+a)}{b}\right] \quad (6.27a)$$

$$E_y(\mathbf{r}+c) = E_y(\mathbf{r}) - \frac{c^2\omega^2}{{c_0}^2}\mu(\mathbf{r})H_x'(\mathbf{r}) + \frac{c^2}{b\varepsilon(\mathbf{r})}\left[\frac{H_y'(\mathbf{r}-a)-H_y'(\mathbf{r})}{a} - \frac{H_x'(\mathbf{r}-b)-H_x'(\mathbf{r})}{b}\right] - \frac{c^2}{b\varepsilon(\mathbf{r}+a)}\left[\frac{H_y'(\mathbf{r}-a+b)-H_y'(\mathbf{r}+b)}{a} - \frac{H_x'(\mathbf{r})-H_x'(\mathbf{r}+b)}{b}\right] \quad (6.27b)$$

$$H_x'(\mathbf{r}+c) = H_x'(\mathbf{r}) + \varepsilon(\mathbf{r}+c)E_y(\mathbf{r}+c) - \frac{{c_0}^2}{a\omega^2\mu(\mathbf{r}-a+c)}\left[\frac{E_y(\mathbf{r}+c)-E_y(\mathbf{r}-a+c)}{a} - \frac{E_x(\mathbf{r}-a+b+c)-E_x(\mathbf{r}-a+c)}{b}\right] + \frac{{c_0}^2}{a\omega^2\mu(\mathbf{r}+c)}\left[\frac{E_y(\mathbf{r}+a+c)-E_y(\mathbf{r}+c)}{a} - \frac{E_x(\mathbf{r}+b+c)-E_x(\mathbf{r}+c)}{b}\right] \quad (6.27c)$$

$$H_y'(\mathbf{r}+c) = H_y'(\mathbf{r}) - \varepsilon(\mathbf{r}+c)E_x(\mathbf{r}+c) - \frac{{c_0}^2}{b\omega^2\mu(\mathbf{r}-b+c)}\left[\frac{E_y(\mathbf{r}+a-b+c)-E_y(\mathbf{r}-b+c)}{a} - \frac{E_x(\mathbf{r}+c)-E_x(\mathbf{r}-b+c)}{b}\right] + \frac{{c_0}^2}{b\omega^2\mu(\mathbf{r}+c)}\left[\frac{E_y(\mathbf{r}+a+c)-E_y(\mathbf{r}+c)}{a} - \frac{E_x(\mathbf{r}+b+c)-E_x(\mathbf{r}+c)}{b}\right] \quad (6.27d)$$

Equations (6.27) can be rearranged into matrix form as follows:

$$\mathbf{F}(\boldsymbol{\rho}, z+c) = \sum_{\rho'} \mathbf{T}(\boldsymbol{\rho}, z+c; \boldsymbol{\rho}', z)\mathbf{F}(\boldsymbol{\rho}', z) \quad (6.28)$$

Where $\mathbf{r} = (\boldsymbol{\rho}, z)$, and $\mathbf{F}(\mathbf{r}) = \begin{bmatrix} E_x(\mathbf{r}) \\ E_y(\mathbf{r}) \\ H_x'(\mathbf{r}) \\ H_y'(\mathbf{r}) \end{bmatrix}$.

The TMM is now complete, and the transfer matrix T in (6.28) links the fields

between two adjacent planes. Once the incident wave is known, applying suitable boundary conditions [31] enables the overall field through the waveguide structure to be determined. In this thesis, a computational code Translight, developed by A. L. Renolds, was used for the calculation of the transmission spectrum.

6.2.4 TMM applied to known structures

To test the validity of the TMM introduced here, it was applied to the known structure reported in Ref. [32]. The structure has a 2D triangular lattice of air columns embedded in a dielectric material (ϵ_d=10.2) with air-filling factor f=28.5%. The calculated transmission spectrum for the TE polarization was plotted in Fig. 6.2.3, which reproduces Fig. 2 in [32], showing the validity of the program for applying it to the calculation of the transmission spectrum for 2D photonic crystals.

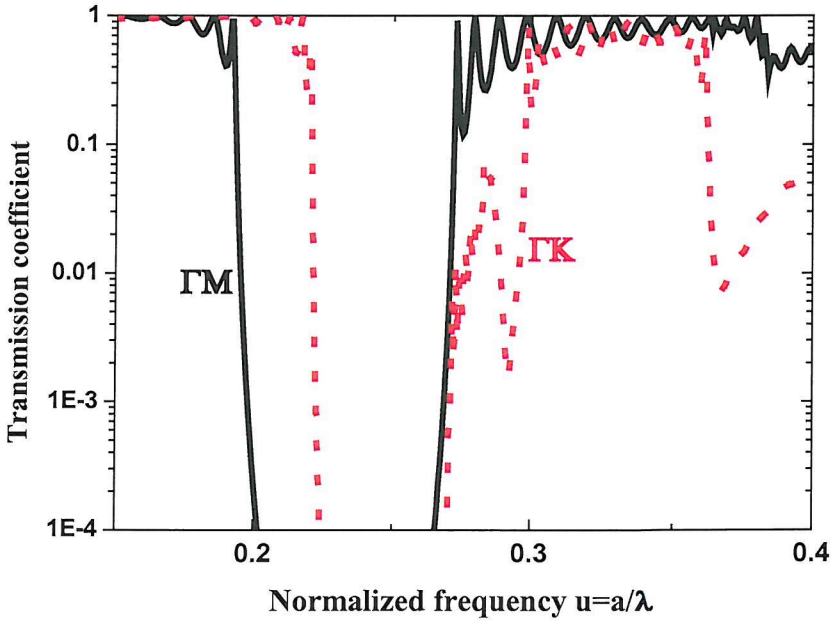

Fig. 6.2.3 Transmission spectrum simulated by TMM for the structure reported in [32]

6.2.5 Finite-difference time-domain (FDTD) method

The FDTD method was first introduced in 1966 by K. S. Yee [33] to solve electromagnetic scattering problems. It was shown that Maxwell's equations can be replaced by a set of finite difference equations based on a discrete space-time mesh, the so-called Yee-cell. Figure 6.2.4 shows the unit Yee-cell in a Cartesian coordinate system.

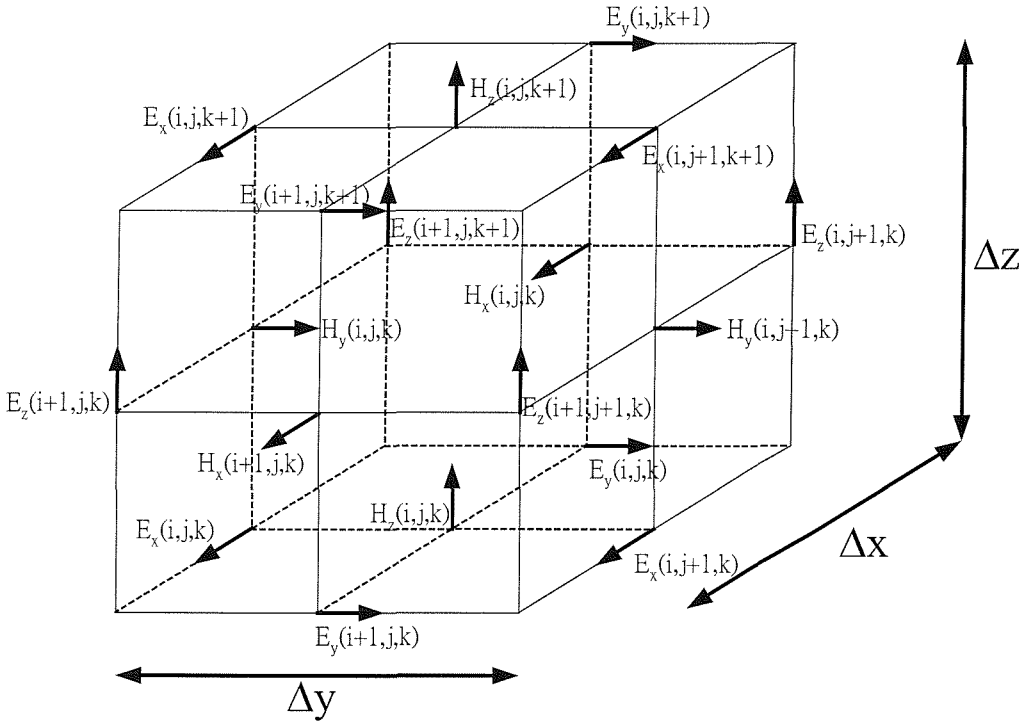

Fig. 6.2.4 A unit Yee-cell and positions of various field components.

The time dependent Maxwell's curl equations (6.3) and (6.4) can therefore be approximated using the central finite difference approximation as follows:

$$H_x^{n+\frac{1}{2}}(i,j,k) = H_x^{n-\frac{1}{2}}(i,j,k) - \frac{\Delta t}{\mu(i,j,k)}\left[\frac{E_z^n(i,j+1,k) - E_z^n(i,j,k)}{\Delta y} - \frac{E_y^n(i,j,k+1) - E_y^n(i,j,k)}{\Delta z}\right] \quad (6.29)$$

$$H_y^{n+\frac{1}{2}}(i,j,k) = H_y^{n-\frac{1}{2}}(i,j,k) - \frac{\Delta t}{\mu(i,j,k)}\left[\frac{E_x^n(i,j,k+1) - E_x^n(i,j,k)}{\Delta z} - \frac{E_z^n(i+1,j,k) - E_z^n(i,j,k)}{\Delta x}\right] \quad (6.30)$$

$$H_z^{n+\frac{1}{2}}(i,j,k) = H_z^{n-\frac{1}{2}}(i,j,k) - \frac{\Delta t}{\mu(i,j,k)}\left[\frac{E_y^n(i+1,j,k) - E_y^n(i,j,k)}{\Delta x} - \frac{E_x^n(i,j,k+1) - E_x^n(i,j,k)}{\Delta y}\right] \quad (6.31)$$

$$E_x^{n+1}(i,j,k) = \frac{\varepsilon(i,j,k) - \sigma(i,j,k)\Delta t/2}{\varepsilon(i,j,k) + \sigma(i,j,k)\Delta t/2} E_x^n(i,j,k) + \frac{\Delta t}{\varepsilon(i,j,k) + \sigma(i,j,k)\Delta t/2} \times \left[\frac{H_z^{n+\frac{1}{2}}(i,j,k) - H_z^{n+\frac{1}{2}}(i,j-1,k)}{\Delta y} - \frac{H_y^{n+\frac{1}{2}}(i,j,k) - H_y^{n+\frac{1}{2}}(i,j,k-1)}{\Delta z}\right] \quad (6.32)$$

$$E_y^{n+1}(i,j,k) = \frac{\varepsilon(i,j,k) - \sigma(i,j,k)\Delta t/2}{\varepsilon(i,j,k) + \sigma(i,j,k)\Delta t/2} E_y^n(i,j,k) + \frac{\Delta t}{\varepsilon(i,j,k) + \sigma(i,j,k)\Delta t/2} \times \left[\frac{H_x^{n+\frac{1}{2}}(i,j,k) - H_x^{n+\frac{1}{2}}(i,j,k-1)}{\Delta z} - \frac{H_z^{n+\frac{1}{2}}(i,j,k) - H_z^{n+\frac{1}{2}}(i-1,j,k)}{\Delta x}\right] \quad (6.33)$$

$$E_z^{n+1}(i,j,k) = \frac{\varepsilon(i,j,k) - \sigma(i,j,k)\Delta t/2}{\varepsilon(i,j,k) + \sigma(i,j,k)\Delta t/2} E_z^n(i,j,k) + \frac{\Delta t}{\varepsilon(i,j,k) + \sigma(i,j,k)\Delta t/2} \times \left[\frac{H_y^{n+\frac{1}{2}}(i,j,k) - H_y^{n+\frac{1}{2}}(i-1,j,k)}{\Delta x} - \frac{H_x^{n+\frac{1}{2}}(i,j,k) - H_x^{n+\frac{1}{2}}(i,j-1,k)}{\Delta y}\right] \quad (6.34)$$

Where the superscript n denotes the discrete time step, i, j, and k indicate the position of a grid point in the x, y, and z directions, respectively. Δt is the time step, and Δx, Δy, and Δz are the space increments along the x, y, and z directions, respectively.

By giving the refractive index distribution n(x,y,z) of a structure and the electromagnetic field excitation, the physical propagation problem can be solved successively through the discretized mesh. In this thesis, a commercial software Fullwave™ was used to calculate the transmission spectrum of the fabricated photonic crystals over a wide range of wavelengths.

6.3 Fabrication of photonic crystal structures

The designed photonic crystals have 2D triangular lattice patterns with lattice constant ranging from 500 nm to 600 nm , and air hole diameter ranging from 200 nm to 500 nm. The photonic crystal structures were fabricated in Ta_2O_5 slab waveguides with thickness 600nm, since this slab waveguide yields the lowest loss over the other two slabs with thickness 500 nm and 700 nm, respectively. Figure 6.3.1 schematically shows the fabrication procedure. First, Ta_2O_5 was RF sputtered onto a Si wafer with a 2 μm SiO_2 buffer layer following the same procedure and same conditions as described in the previous chapter (section 5.3.1). Secondly, an 80 nm thick film of Al was thermally evaporated onto the wafer for the purpose of removing excess charge and reducing the proximity effect during the electron beam (e-beam) direct-writing process. In addition, it functioned as an etching mask for transferring patterns into the underlying Ta_2O_5 layer at a later fabrication stage. A layer of 300 nm thick UV III electro-resist was subsequently spin-coated onto the wafer and soft-baked at 90°C for 1 hour. After this, the photonic crystal patterns were generated using the e-beam direct-writing technique. The exposed film was then developed resulting in the desired photonic crystal patterns being created in the

UV III electro-resist layer. The pattern was then transferred onto the Al layer by wet etching through the pore where the UV III was developed away.

In order to transfer the photonic crystal patterns into the Ta_2O_5 film, a reactive ion etching (RIE) process was followed. The etching characteristics of Ta_2O_5 using different plasma chemistries has been extensively studied [34] and were further evaluated in [35]. In this study, the dry etching was performed in a Plasmalab™ system reactor. The sample was placed on a graphite chuck and the system was driven by a 13.56 MHz RF power matching unit operating at 100W. A plasma was generated with Ar and CHF_3 gas introduced into the chamber at a relative partial pressure of 2:1 with the chamber pressure held at 20 mTorr. A series of chemical reactions, responsible for the etching mechanism of Ta_2O_5 took place subsequently and are described as follows [36]:

$$CHF_3 \rightarrow CF_x + F$$
$$F + Ta \rightarrow TaF_5$$
$$CF_x + O_2 \rightarrow CO + CO2 + COF_2$$

First, the CHF_3 was dissociated in the plasma to form various CF_x radicals and atomic fluorine, which then reacted with tantalum to form TaF_5. The CF_x radicals were then reacted with the oxygen in the Ta_2O_5 to form CO, CO_2, and COF_2. These gaseous products are volatile, so that they can be pumped out of the chamber easily.

After the etching process, the Al film was removed by wet etching resulting in photonic crystal structures within the film of Ta_2O_5. Figure 6.3.1 (a)-(f) schematically shows the fabrication process. SEM images of the fabricated photonic crystal waveguides are shown in Figure 6.3.2.

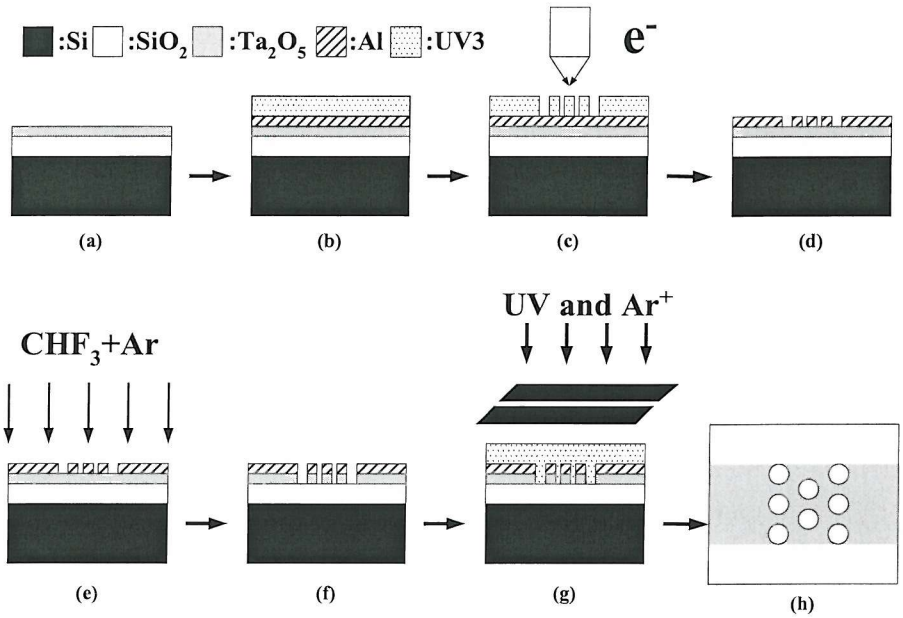

Fig. 6.3.1 Fabrication process of: (a)-(f) photonic crystal structures within Ta_2O_5 slab waveguide. (g)-(h) photonic crystal structures embedded in Ta_2O_5 rib waveguide.

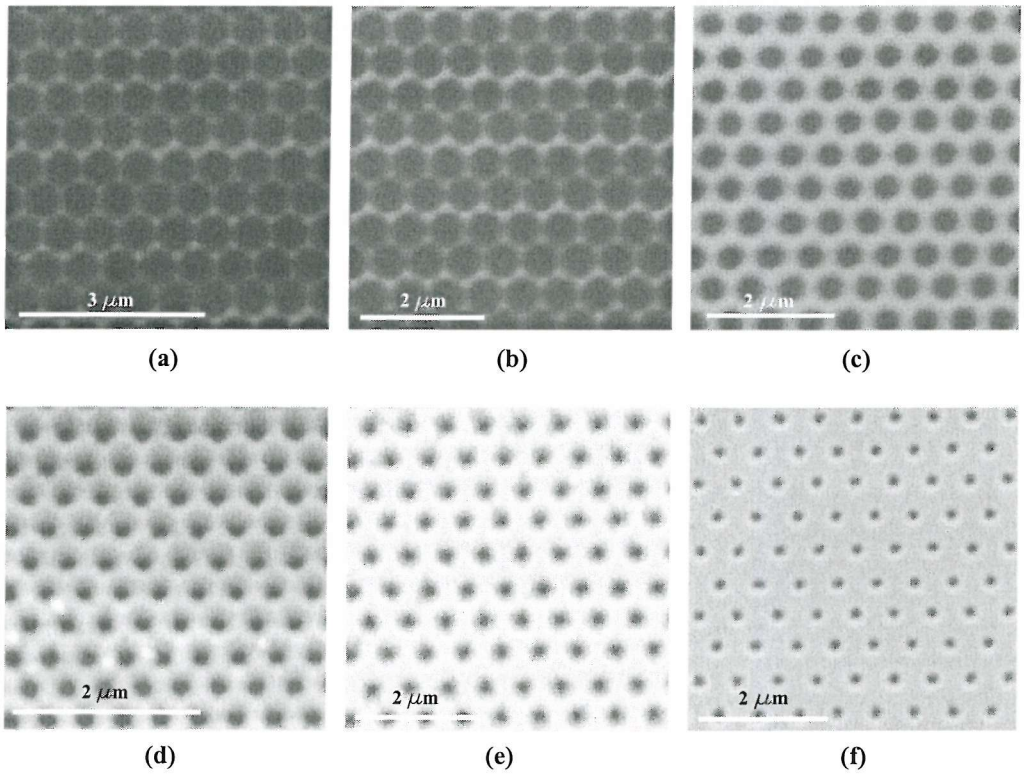

Fig. 6.3.2 SEM images of the fabricated photonic crystal structures.

A cross-sectional view of the etched cylinders is shown in Fig. 6.3.3. It is found that the Ta_2O_5 was etched throughout its depth with a sidewall angle very close to 90°. The detailed structure parameters (measured from the corresponding SEM images) for the fabricated photonic crystals are listed in Table III.

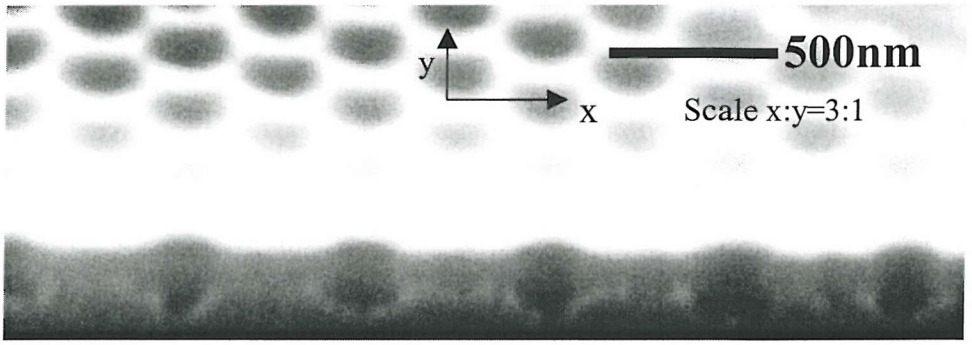

Fig. 6.3.3 Cross-sectional view of the etched photonic crystals (top view is shown in **Fig. 6.3.2(c)**).

Table III Structure parameters for the fabricated photonic crystals.

photonic crystal ID	lattice constant a (μm)	hole radius r (μm)	aspect ratio (r/a)
(a)	0.617	0.266	0.431
(b)	0.632	0.265	0.419
(c)	0.581	0.188	0.324
(d)	0.637	0.155	0.243
(e)	0.576	0.136	0.235
(f)	0.586	0.103	0.176

Since a photonic crystal is a highly dispersive medium, it is necessary to create lateral confinement in order to correctly probe the photonic band structures along a particular direction. To achieve this, standard photolithography was utilized to create protective stripes of photoresist of width 3 μm, aligned along the Γ-M direction in the first Brillouin zone (1BZ), over the fabricated slab photonic crystal waveguide. Argon ion beam etching was subsequently used to create the rib waveguide structures, resulting in photonic crystal embedded in rib waveguides. This part of the fabrication process is schematically shown in Fig. 6.3.1 (g)-(h). Fig. 6.3.4 shows an SEM image of a typical fabricated structure.

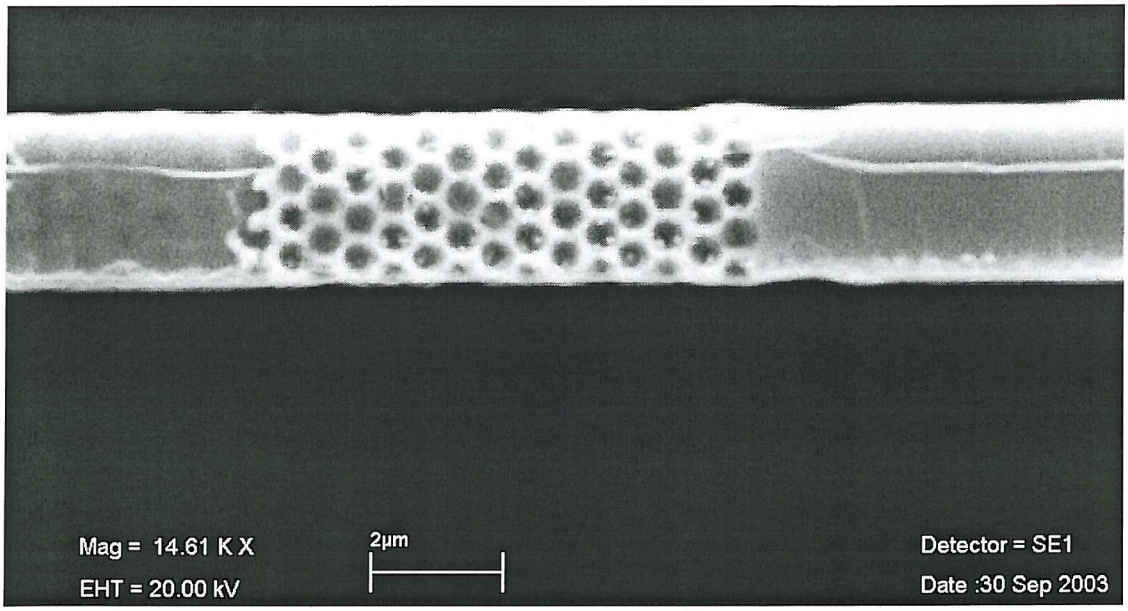

Fig. 6.3.4 Embedded photonic crystal structure in a Ta_2O_5 rib waveguide.

6.4 Characterization and discussion

To probe the fabricated photonic crystals, an ultrabroadband white light continuum (WLC) was used as the light source. This was obtained by focusing 1 μJ amplified pulses in a sapphire crystal, creating a strong whole beam self-focusing effect. As a consequence, the beam collapses on itself leading to a significant increase of the pulse intensity to the level where self-phase modulation (SPM) takes place to generate a rapid frequency sweep from the ultraviolet to the infrared. These (WLC) pulses were then focused into the photonic crystal structure using a 40× microscope objective, and the transmitted probe pulse was collimated and focused into a spectrometer, dispersed by a grating, and detected by a CCD array. Fig. 6.4.1 schematically shows the experimental arrangement for this transmittance measurement.

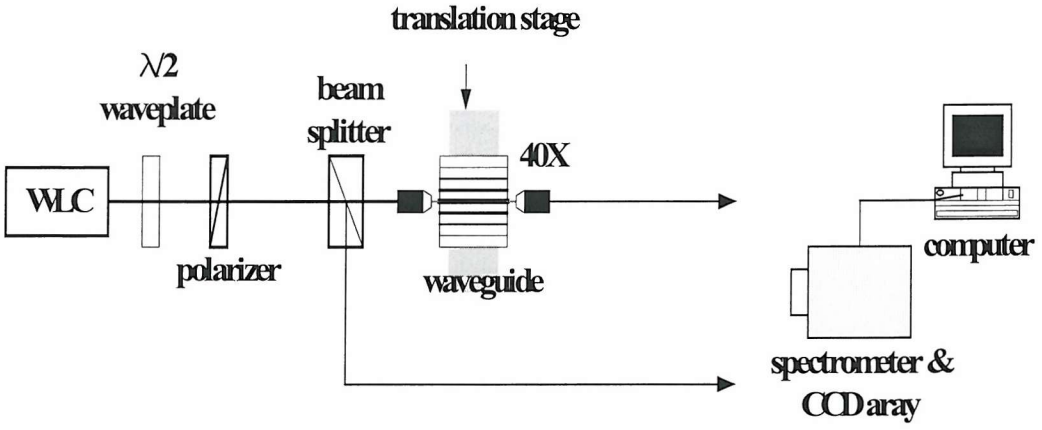

Fig. 6.4.1 Experimental setup for the transmittance measurements.

Prior to measuring the photonic crystals, a transmittance measurement was first performed for an unstructured Ta_2O_5 rib waveguide without photonic crystals incorporated. Figure 6.4.2 shows the obtained spectrum. The transmittance has been normalized so that the peak transmission is 1. A shallow transmission drop at λ~604 nm is observed, which is believed to be due to multimode interference. The fringes superimposed on the spectrum are not fully understood but may be attributed to the effect of polarization mode coupling. The transmittance at a wavelength shorter than λ=625 nm is proportional to λ^4, indicating that the waveguide roughness may responsible for the low transmittance caused by Rayleigh scattering. The subsequent increase of the transmittance is unclear yet. Apart from that, no significant transmission notches exist in the measured wavelength range.

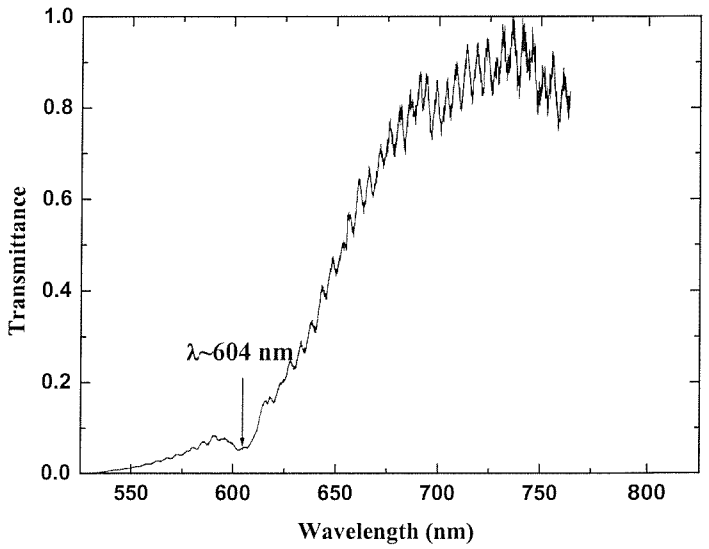

Fig. 6.4.2 Transmission spectrum for an unstructured Ta_2O_5 rib waveguide.

Fig. 6.4.3 shows the transmission spectrum for a rib waveguide with embedded photonic crystal which contains 14 rows of air rods distributed in a triangular lattice

arrangement with lattice constant a=581 nm and radius r=188nm. The transmittances for both polarizations are normalized to their respective peak transmission so that the peak transmittance in each case is 1. A mini transmission notch centered around λ=731 nm with a bandwidth of 23 nm has been observed for the TE polarization. For the TM polarization, two notches centered at λ=665 nm with a bandwidth of 27 nm and at λ=739 nm with a bandwidth of 41 nm were observed, respectively. These transmission notches have more than 30% extinction and occur in the wavelength range where no significant transmission notches were observed in the simple Ta_2O_5 rib waveguide. The low transmittance at shorter wavelengths due to the coupling to radiation modes and stronger Rayleigh scattering is clearly in evidence in the figure.

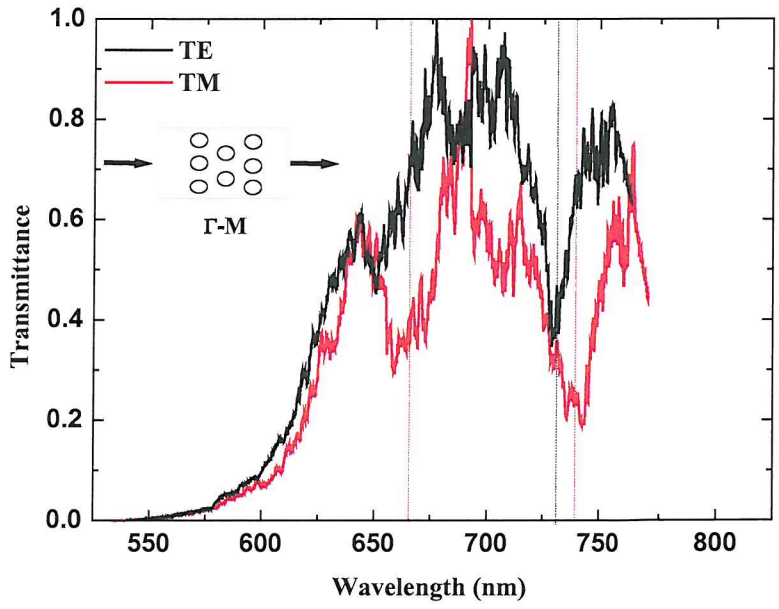

Fig. 6.4.3 Transmission spectra of the embedded photonic crystal with lattice constant a=581 nm, and radius r=188 nm.

The expected photonic band structure was calculated theoretically using the PWE method for both polarizations and is plotted in Fig. 6.4.4. According to the lattice orientation, the transmittance was probed along the Γ-M direction in the first Brillouin zone (1BZ) of the reciprocal lattice. It can be seen that in this direction, there are two PBGs, lying between (a/λ value): (0.316-0.358), (0.650-0.736), and (0.320-0.426), (0.712-0.732) for the TE and TM polarizations, respectively. The corresponding wavelength ranges are (1623-1839 nm), (789-894 nm), and (1364-1816 nm), (793-816 nm) for the TE and TM polarizations, respectively.

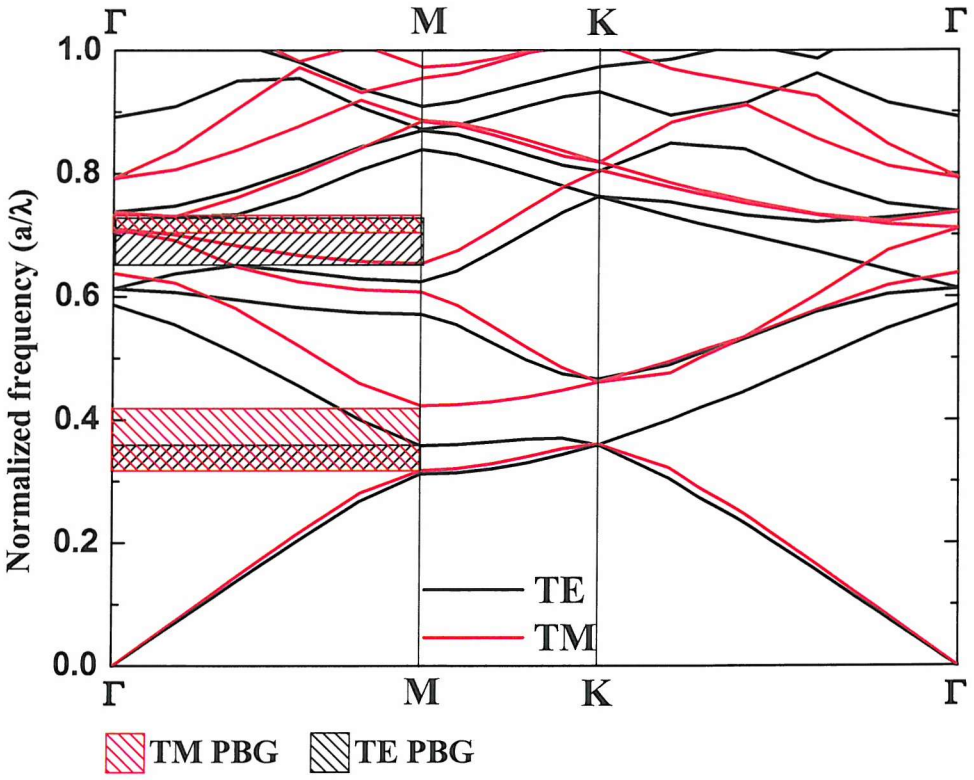

Fig 6.4.4. Photonic band structures for both polarizations. The hatched regions are PBGs.

Obviously, the first PBG is beyond the wavelength range where the experiment is performed for both polarizations, while both of the second PBGs are centered at wavelengths longer than those found experimentally, indicating a possible underestimation of the lattice constant. However, the theoretical prediction assumes a structure with air columns extended infinitely along the vertical direction. This is not exactly the case being dealt with here. For this reason, this result was compared with those obtained by the TMM and FDTD.

The transmission spectrum of the PC simulated using the TMM is shown in Fig. 6.4.5 and Fig.6.4.6 for the TE and TM polarization, respectively. For the TE polarization, the lowest PBG is signatured by the significant transmission drop in the wavelength range 780-877 nm with the presence of some suspicious shallow states, and the next higher order PBG is situated between 541-551 nm. The position of the first PBG (780-877nm) is situated at longer wavelengths than that of the experiment result (719-743 nm), and agrees well with that found using the PWE method (789-894 nm) previously. For the TM polarization, four deep transmission notches were found in the wavelength ranges 818-882 nm, 741-777 nm, 692-713 nm, and 647-671 nm, where the second PBG and the fouth PBG are close to the experimental result.

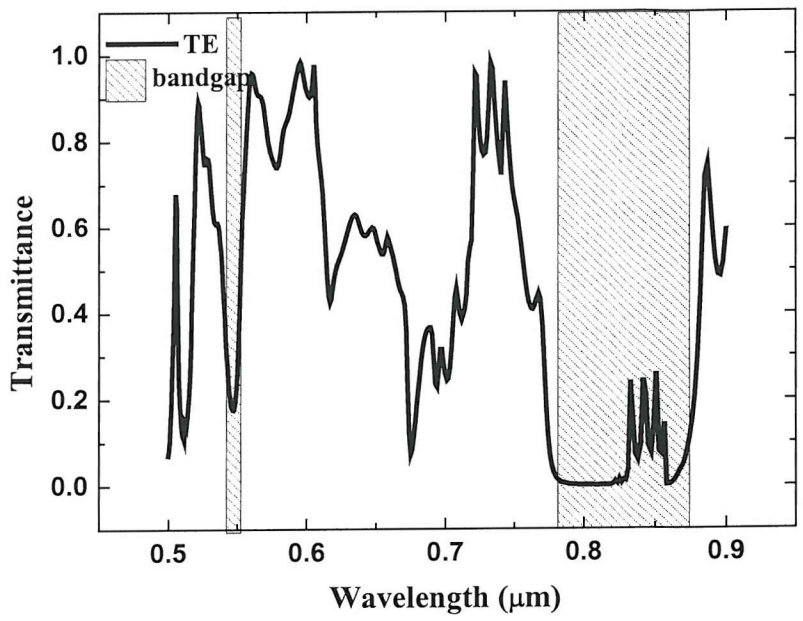

Fig. 6.4.5 TMM simulated transmission spectrum for the TE polarization.

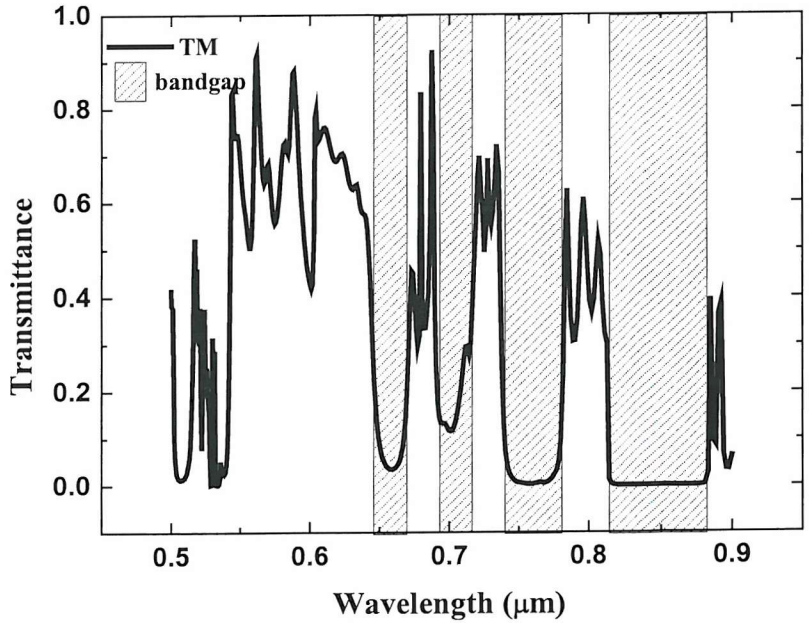

Fig. 6.4.6 TMM simulated transmission spectrum for the TM polarization.

Fig. 6.4.7 shows the transmission spectrum simulated by FDTD method. The result shows a broad PBG at 764-881 nm and a narrow one at 583-605 nm for the TE polarization. Three shallow PBGs at 852-930nm, 709-787 nm, and 496-538 nm were found for the TM polarization. Only the second PBG of the TM polarization fits the experimental result.

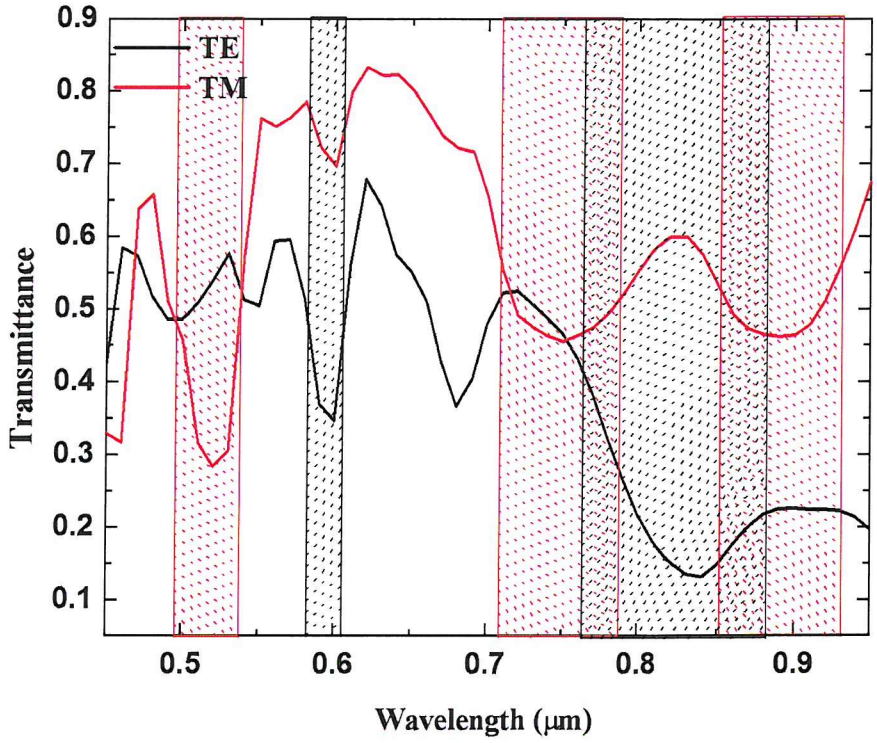

Fig. 6.4.7 FDTD simulated transmission spectrum for both polarizations.

Figure 6.4.8 is a summary of the measured PBGs, and a comparison of results obtaining from PWE, TMM, and FDTD methods. For TE polarization, all of the three computational schemes predict a PBG between ~764-894 nm, which is ~100 nm longer than that observed in the experiment (719-743 nm). Both FDTD and

TMM predict a second narrow PBG where experiment and PWE method do not find one. For the TM polarization, the deviations between the calculated PBGs become bigger and seem to have less correlation. In this case, TMM and FDTD methods match better to the experiment.

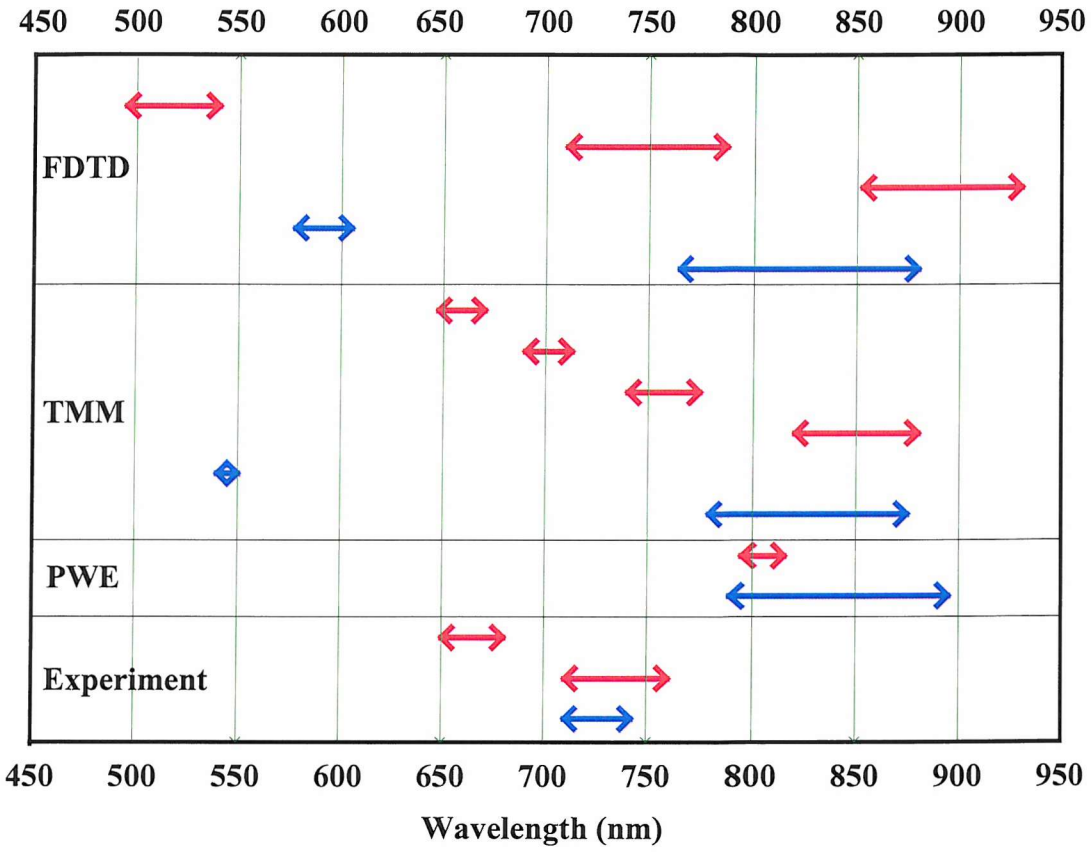

Fig. 6.4.8 A comparison between the measured PBGs and those predicted by PWE, TMM, and FDTD. The blue lines represent the TE polarization, and the red lines represent the TM polarization.

The wavelength response of photonic crystals is highly sensitive to the structural parameters, in particular, feature size fluctuations, due to the high index contrast. It has been shown that by changing the defect size of a quarter-wave stack mirror with

index contrast 3.4:1 by 0.2 nm, the wavelength response shifts by ~1 nm at λ=1.55 μm [37]. Assuming that the accuracy of the SEM resolved feature size for the photonic crystal waveguides reported here is of the order of 20nm, the wavelength response may be expected to shift by 100 nm. Therefore, it is very difficult to precisely predict of the position of the PBGs for a specific PC pattern based on the limited sampling of the SEM image. It is also apparent that different numerical approaches cannot achieve fully consistent results, presumably due to the different approximations made and different calculation parameters such as the size of the discretized mesh. This is very critical particularly in calculating nano-sized features.

To average out the fluctuations and to clarify whether the measured transmission notch corresponds to a possible PBG in the wavelength range where the previous experiment is performed, a cascaded PC was fabricated, in an attemp to overlap different PBGs based on different lattice constants and air column radii. The resultant structure contains 4 PC patterns (PC(a)-(d) in Fig.6.3.2) with a total number of air rods N=80. Fig. 6.4.9 shows the measured transmission spectrum. The transmittances for both polarizations have been normalized to their respective peak transmission. It can be seen that there is a broad transmission stop-band between 680-787 nm for both polarizations. This enlargement of the PBG is attributed to the overlap of individual PBGs of each PC pattern and gives an indication that PBGs for the PC patterns demonstrated in this study may exist in this wavelength range.

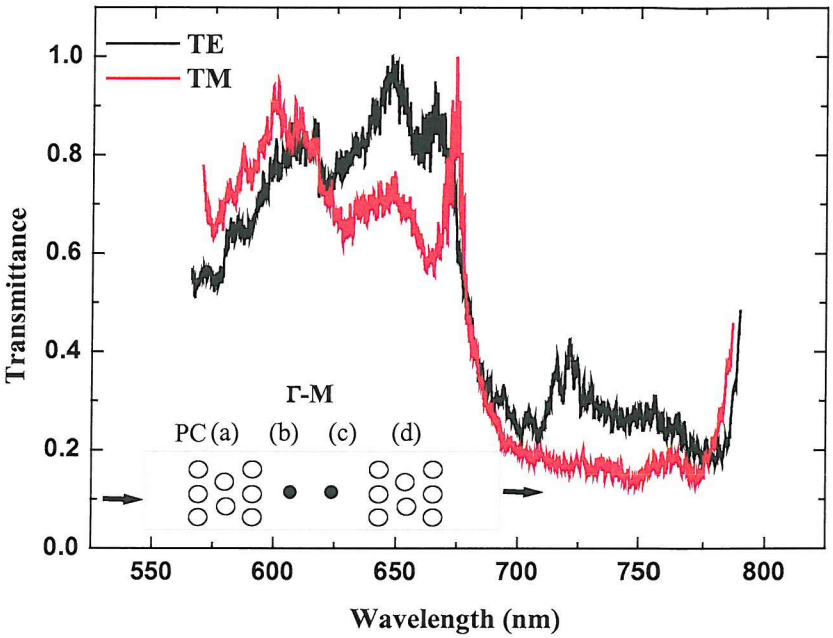

Fig. 6.4.9 Transmission spectrum of the embedded cascade photonic crystals for both polarizations.

6.5 Conclusion

Photonic crystals with air columns in a triangular lattice arrangement have been successfully fabricated in Ta_2O_5. To accurately probe the transmittance in a particular direction, photonic crystals are incorporated within a rib waveguide using post-fabrication photolithography. The transmission spectrum shows a transmission notch centered around 731 nm with a bandwidth of ~23 nm for the TE polarization. For the TM polarization, two transmission drops centered at 739 nm, with a bandwidth of 41nm, and another one centered at 665 nm, with a bandwidth of 27 nm, were observed. The transmission spectra simulated by PWE, TMM and

FDTD give different results except for the lowest band of TE polarization. The discrepancy is attributed to different approximations in the models and different discretized mesh, which are vital parameters for the calculation involving nano-structures. In order to identify whether the transmission notch corresponds to a possible PBG, a cascaded PC was fabricated. A broad transmission drop (over 100 nm) was observed and this was attributed to the overlap of individual PBGs for each PC pattern. This PBG enlargement effect gives stronger support to state that the PBGs corresponding to the PC patterns introduced in this study may lie at wavelength range from 680-790nm.

The result presented in this chapter shows some typical band gap features, however further work is required to confirm PBG behaviour. Theoretically, more rigorous theorem (3D full vectorial program for the Maxwell equations) has to be considered. Experimentally, more precise fabrication and measurement of the transmission spectrum in the infrared range has to be carried out. Further progress needs more computational resource and more advanced fabrication techniques, which is a challenge to current fabrication and modelling techniques. Constructing an empirical relationship between the design, fabrication, and the measured parameters and the device performance may provide a practical solution.

References

[1] Eli Yablonovitch, Phys. Rev. Lett., vol. **58**, 2059 (1987).

[2] Sajeev John, Phys. Rev. Lett., vol. **58**, 2486 (1987).

[3] Meade, R. D., O. Alerhand and J. D. Joannopoulos, Handbook of Photonic Band Gap Materials. (1993)

[4] K. M. Ho, C. T. Chan and C. M. Soukoulis, Phys. Rev. Lett., vol. **65**, 3152 (1990).

[5] E. Yablonovitch, T. J. Gmitter, and K. M. Leung, Phys. Rev. Lett., vol. **67**, 2295 (1991)

[6] Y. S. Chan, C. T. Chan and Z. Y. Liu, Phys. Rev. Lett., vol. **80**, 956 (1998).

[7] Zoorob ME, Charlton MDB, Parker GJ, Baumberg JJ and Netti MC, Nature, vol. **404**, 740 (2000).

[8] Attila Mekis, J. C. Chen, I. Kurland, Shanhui Fan, Pierre R. Villeneuve and J. D. Joannopoulos, Phys. Rev. Lett., vol. **77**, 3787 (1996).

[9] Tokushima M, Kosaka H, Tomita A and Yamada H, Appl. Phys. Lett., vol. **76**, 952 (2000).

[10] S. Yamada, T. Koyama, Y. Katayama, N. Ikeda, Y. Sugimoto, K. Asakawa, N. Kawai and K. Inoue, J. Appl. Phys., vol. **89**, 855 (2001).

[11] Min Qiu and Sailing He, Physica B, vol. **299**, 187 (2001).

[12] S. L. McCall, P. M. Platzman, R. Dalichaouch, D. Smith ans S. Schultz, Phys. Rev. Lett., vol. **67**, 2017 (1991).

[13] D. R. Smith, S. Schultz, S. L. McCall and P. M. Platzmann, J. Mod. Opt., vol. **41**, 395 (1994).

[14] J. D. Joannopoulos, P. R. Villeneuve and S. Fan, Nature, vol. **386**, 143 (1997).

[15] H. Yokoyama, Science, vol. **256**, 66 (1992).

[16] O. Painter, R. K. Lee, A. Scherer, A. Yariv, J. D. O'Brien, P. D. Dapkus and I. Kim, Science, vol. **284**, 1819 (1999).

[17] M. Boroditsky, T. F. Krauss, R. Coccioli, R. Vrijen, R. Bhat and E. Yablonovitch, Appl. Phys. Lett., vol. **75**, 1036 (1999).

[18] Yu. A. Vlasov, K. Luterova, I. Pelant, B. Hönerlage and V. N. Astratov, Appl. Phys. Lett., vol. **71**, 1616 (1997).

[19] Kazuaki Sakoda, Optics Express, vol. **4**, 167 (1999).

[20] Shunji Nojima, Jpn. J. Appl. Phys., vol. **37**, L565 (1998).

[21] Jonathan P. Dowling, Michael Scalora, Mark J. Bloemer and Charles M. Bowden, J. Appl. Phys., vol. **75**, 1896 (1994).

[22] Shamino Wang, Hernan Erlig, Harold R. Fetterman, Eli Yablonovitch, Victor Grubsky, Dmitry S. Starodubov and Jack Feinberg, Microw. Opt. Technol. Lett., vol. **20**, 17 (1999).

[23] N. I. Koroteev, S. A. Magnitskii, A. V. Tarasishin and A. M. Zheltikov, Opt. Comm., vol. **159**, 191 (1999).

[24] Hideo Kosaka, Takayuki Kawashima, Akihisa Tomita, Masaya Notomi, Toshiaki Tamamura, Takashi Sato and Shojiro Kawakami, Phys. Rev. B, vol. **58**, R10096 (1998).

[25] Hideo Kosaka, Takayuki Kawashima, Akihisa Tomita, Masaya Notomi, Toshiaki Tamamura, Takashi Sato and Shojiro Kawakami, Appl. Phys. Lett., vol. **74**, 1370 (1999).

[26] John D. Joannopoulos, Robert D. Meade, and Joshua N. Winn, " Photonic Crystal". (Princeton University Press) (1994).

[27] G. Golub and C. Van Loan, "Matrix Computations". (Johns Hopkins University Press) (1989).

[28] R. D. Meade, K. D. Brommer, A. M. Rappe, and J. D. Joannopoulos, Appl. Phys. Lett., vol. **61**, 495 (1992).

[29] J. B Pendry and A. Mackinnon, "Low Energy Electron Diffraction". (London Academic) (1974).

[30] J. B. Pendry and A. Mackinnon, Phys. Rev. Lett., vol. **69**, 2772 (1992).

[31] G. R. Hadley, Opt. Lett., vol. **16**, 624 (1991).

[32] D. Labilloy, H. Benisty, C. Weisbuch, T. F. Krauss, R. M. De La Rue, V. Bardinal, R. Houdre, U. Oesterle, D. Cassagne, and C. Jouanin, Phys. Rev. Lett., vol. **79**, 4147 (1997).

[33] K. S. Yee, IEEE Trans. Ant. Prop., vol. **14**, 302 (1966).

[34] Yue Kuo, J. Electrochem. Soc., vol. **139**, 579 (1992).

[35] K. P. Lee, K. B. Jung, R. K. Singh, S. J. Pearton, C. Hobbs, and P. Tobin, J. Vac. Sci. Technol. A, vol. **18**, 1169 (2000).

[36] L. B. Jonsson, J. Westlinder, F. Engelmark, C. Hedlund, J. Du, and U. Smith, J. Vac. Sci. Technol., vol. **18**, 1906 (2000).

[37] T. F Krauss, Photonics Crystals for Integrated Optics [Online]. 2001 [10th Apr 2002]. Available from World Wide Web: <http://www.st-and.ac.uk/phys>

Chapter 7 Conclusion and future work

7.1 Introduction

This thesis presents the assessment of a widely used dielectric material, Ta_2O_5, aimed at exploring its potential optical properties and demonstrating the feasibility of broadening the functionality of Ta_2O_5 waveguides for application to compact integrated multifunctional optical devices. Two approaches were followed to demonstrate the potential of Ta_2O_5 waveguides. One was based on exploring material properties (UV photosensitivity and optical nonlinearity), while the other approach was based on the alteration of the physical structures (embedded photonic crystals and hybrid integration). Both approaches exploited photolithographically defined rib waveguides. This chapter gives a comprehensive summary of the work carried out based upon these building blocks and draws together the conclusions from the individual chapters.

7.2 Conclusions from the work

Ta_2O_5 has a refractive index n>2, allowing a high Δn material system to be formed on standard SiO_2/Si wafers. The correlation between the modal field distributions and the waveguide geometry has been studied in Chapter 2. On one hand, the high Δn can provide strong confinement (stripe waveguide), enabling miniaturized devices, while on the other hand, the confinement can be weak (rib waveguide with shallow etch depth), giving better coupling with conventional fibre systems and other guided wave components. This property can be flexibly adjusted by selecting

appropriate etching time to result in different etch depths of the rib waveguide.

UV photosensitivity has been addressed using a rib waveguide based Mach-Zehnder interferometer. It is found that a total cumulative fluence of 72 J/cm^2 at λ=248 nm induces a saturated refractive index change of $\Delta n=(-2.1\pm0.1)\times10^{-3}$. This procedure yields a significant UV photosensitivity with no hydrogen loading and may provide an easy route to integrate additional functionalities through UV direct-writing. It also demonstrates the potential for post-fabrication trimming to correct fabrication errors, allowing a wider fabrication tolerance, or to customize the function of a standardized optical circuit layout.

The third-order optical nonlinearity in a 1 cm-long Ta_2O_5 rib waveguide has been evaluated from the observed spectral broadening induced by self-phase modulation. The experiment was carried out at λ=800 nm, where the group velocity dispersion was shown to have a negligible impact based on a femtosecond time-of-flight Kerr-gate technique. The optical nonlinear refractive index n_2 was estimated to be $7.2\pm0.4\ \times10^{-19}$ m^2/W, which is higher than conventional silica glass by more than one order of magnitude. This large value of n_2 in Ta_2O_5, in conjunction with its high index may provide an opportunity to achieve small-sized core, low-operating power, all-optical switching devices.

The other direction pursued in this thesis to broaden the functionality of Ta_2O_5 waveguides is by tailoring the waveguide structure. Hybrid integration was

demonstrated using a self-assembled microsphere grating combined with a rib waveguide. The optical coupling between the modal evanescent field and the self-assembled array results in a stopband in the transmission spectrum, at a wavelength close to the Bragg wavelength. Adjustable grating strength was also demonstrated by varying the refractive index of the cladding medium. More work upon sphere uniformity and the self-assembly process is required to improve the grating uniformity, however, this study represents significant progress towards a simple route to hybrid circuits combining microspheres in novel functional materials with waveguides in conventional materials.

Embedded photonic crystals within rib waveguides are also demonstrated in this thesis. These first results show some typical band gap features, and further work is required to improve these structures. Nonetheless, photonic crystals have been proved in other material systems and it is widely believed that the fabrication is the most challenging issue. From the fabrication standpoint, the work presented in the thesis demonstrates the success of developing a fabrication process to incorporate photonic crystals within rib waveguides, in particular, the etching conditions leading to a nearly perpendicular sidewall.

The following table summarizes some material properties of Ta_2O_5 combining properties from the literature used in this work and some determined as part of this work.

Table IV Selected material parameters of Ta_2O_5

Parameter	Value	Reference
Refractive index n	2-2.2@400-2000nm	[1]
Dielectric constant	>25	[2]
Electrical breakdown strength	1×10^6-8×10^6 Volt/cm	[3]
Band gap	~ 4.3eV	[4]
Absorption edge	λ~260 nm	This work
Phonon energy	<900 cm^{-1}	[5]
Crystallisation temperature	>600℃	[6]
UV-photosensitivity	Δn~ -2.1×10^{-3},72 J/cm^2@248nm	This work
Nonlinear refractive index n_2	7.2×10^{-19} m^2/W @800 nm	This work
Index-temperature coefficient	$dn/dT\sim2.3\times10^{-6}$ 1/K @633nm	[7]

7.3 Proposals for future work

This section proposes some possible future areas of work to improve the device performance, to extend functionality, and to apply the material properties explored in the present study.

7.3.1 Waveguide loss reduction and coupling interface construction

Propagation loss is a factor that limits the number of components that can be integrated on a chip. The minimum propagation loss achieved in this study was 1.6 dB/cm at 1550 nm and was identified to be primarily due to the defects and the sidewall roughness. A very dense and smooth Ta_2O_5 film has been demonstrated by

oxygen cluster ion assisted deposition [8], which can be applied to the present study to further decrease the intrinsic loss. Significant reduction of the sidewall roughness has been reported for a submicrometer sized waveguide in SOI material system utilizing the oxidation smoothing technique, leading to a low-loss level (0.8 dB/cm) at λ=1.54 μm [9]. A similar technique has also been employed to achieve a low-loss (0.9dB/cm) planar waveguide in Ta_2O_5 [10]. In this method, Ta_2O_5 rib waveguides can be obtained by thermally oxidizing sputtered metallic tantalum stripes which also has the advantage of avoiding the ion-beam milling process. This "bottom-up" approach may reduce the sidewall roughness and lead to a further reduction in propagation loss. In addition, UV annealing may be used to reduce the absorption and chemicals such as KOH may be used to smooth the structure.

Another requirement is to construct appropriate coupling interfaces between optical components, particularly for coupling to fiber-based systems. Although it has been shown that the rib waveguide structure has the potential for single mode operation with an oversized cross-section, the requirement for a very uniform thick film challenges the present fabrication technique and is not practical. A spot-size converter based on the tapered-velocity coupler (TVC) configuration [11] may provide a solution. Fig. 7.3.1 shows a schematic of the potential realization of the proposed structure. The ion-exchanged channel is designed to be compatible with the fibre mode. The photonic crystal waveguide, loaded on the ion-exchanged channel, was tapered laterally along the direction of propagation. When adiabatic condition is satisfied, the optical energy may be transferred from the bottom to the

upper layer with low loss.

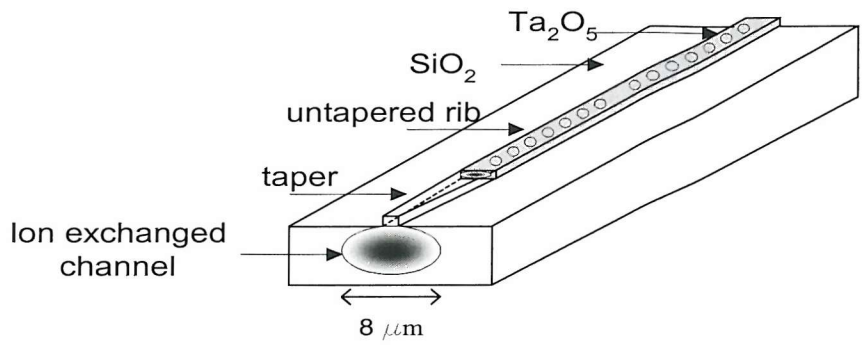

Fig. 7.3.1 Proposed TVC for the improvement of the coupling efficiency.

7.3.2 Uniformity improvement for self-assembled grating and photonic crystals

As demonstrated in the thesis, the wavelength response of the microsphere grating is strongly affected by the uniformity of the structure. Therefore, a longer effective grating length is desired for averaging out the disorder and for the enhancement of the extinction. Field assisted self-assembly using a technique such as optical holographic tweezers [12] may provide better control over particle spacing than simply relying upon capillary force and gravity. Locally controlling the surface chemistry is also worth pursuing in order to obtain a larger assembled area with improved uniformity.

The wavelength response of photonic crystals is even more sensitive to the structural parameters (period, hole radius, sidewall angle) than microsphere gratings due to their high index contrast. Obviously, the fabrication tolerance has to be taken into account at the design stage. Since the feature size has already challenged the accuracy of current fabrication and modelling techniques, constructing an empirical

relationship between the design, fabrication, and the measured parameters and the device performance seems to be practical and crucial work to stabilize manufacturing.

7.3.3 Practical devices and future applications

The significant UV photosensitivity and optical nonlinearity of tantalum pentoxide established in this thesis can be readily applied to the design of practical devices such as tunable Mach-Zehnder interferometers, all-optical switches and logic gates. Application of these material properties to photonic crystal waveguides can also provide static trimming or dynamic tuning which may find useful application in optical delay control. These individual components can further be linked, using photonic crystal waveguides, or self-assembled microsphere gratings as optical interconnections, to form multifunctional photonic circuits.

Rare earth ion doping of Ta_2O_5 waveguides is another potential topic for further exploration. Lasing operation has recently been observed in Nd-doped Ta_2O_5 waveguides which promises the possibility for doping with other rare-earth elements. This opens the opportunity to realize multi-wavelength light sources which may be integrated with other passive devices. The established piezoelectric effect may also be combined with the lasers for tailoring photon modes. For example, controlling the modes of photonic crystal defect lasers is an interesting topic for future work.

Ta_2O_5 has been shown to have many promising properties for application in a variety of planar lightwave circuit elements. In passive waveguide structures, it can form photonic crystals, be exploited for its strongly intensity-dependent refractive index, and be modified by UV writing, for example, while with the future incorporation of rare-earth elements, it can be further extended to realise active components such as lasers. Moreover, excellent compatibility with silicon technology, and well-established deposition techniques make it a competitive material for high-density integrated optical circuits.

References

[1] Tantalum oxide,Ta_2O_5 for optical coating [Online]. 2003 [Accessed 2nd May 2004]. Available from world wide web:<http://www.cerac.com/pubs/proddata>

[2] J. Y. Zhang, B. Lim, V. Dusastre, and I. W. Boyd, Appl. Phys. Lett., vol. **73**, 2299 (1998)

[3] C. Chaneliere, J. L. Autran, R. A. B. Devine, and B. Balland, Mat. Sci. Eng., vol. **R22**, 269 (1998).

[4] E. Franke, C. L. Trimble, M. J. DeVries, J. A. Woollam, M. Schubert, and F. Frost, J. Appl. Phys., vol. **88**, 5166 (2000).

[5] P. S. Dobal, R. S. Katiyar, Y. Jiang, R. Guo, and A. S. Bhalla, J. Raman Spectroscopy, vol. **31**, 1061 (2000).

[6] P. C. Joshi and M. W. Cole, J. Appl. Phys., vol. **86**, 871 (1999).

[7] A. K. Chu, H. C. Lin, W. H. Cheng, J. Electron. Mater., vol. **26**, 889 (1997).

[8] Y. Fujiwara, N. Toyoda, K. Mochiji, T. Mitamura, and I. Yamada, Nucl. Instrum. Met. Phys. Res. B, vol. **206**, 870 (2003).

[9] K. K. Lee, D. R. Lim, L. C. Kimerling, J. Shin, and F. Cerrina, Opt. Lett., vol. **26**, 1888 (2001).

[10] D. H. Hensler, J. D. Cuthbert, R. J. Martin, and P. K. Tien, Appl. Opt., vol. **10**, 1037 (1971).

[11] C. Y. Tai, *Tapered 1D Photonic Band Gap Waveguide Microcavity.* Mini-thesis, University of Southampton, (2002).

[12] R. L. Eriksen, P. C. Mogensen, and J. Glückstad, Opt. Lett., vol. **27**, 267 (2002).

List of Publications

In Journals

1) **A. Favre, E. Lee, V. Apostolopoulos, C. B. E. Gawith, C. Y. Tai, E. M. Taylor, Y. Kondo, and F. Koizumi**
UV-written channel waveguides in Er^{3+}-doped Bi_2O_3-based glass
Physica Status Solidi (c), 2004, Vol.1 (2), pp.295-8
2) **S. Pissadakis, A. Ikiades, C. Y. Tai, N. P. Sessions, and J. S. Wilkinson**
Sub-micron period grating structures in Ta_2O_5 thin oxide films patterned using UV laser post-exposure chemically assisted selective etching
Thin Solid Films, 2004, Vol. 453-454, pp. 458-461
3) **C. Y. Tai, B. Unal, J. S. Wilkinson, M. A. Ghanem, and P. N. Bartlett_**
Optical coupling between a self-assembled microsphere grating and a rib waveguide
Appl. Phys. Lett., 2004, Vol. 84, pp. 3513-3515
4) **C. Y. Tai, Christos Grivas, and J. S. Wilkinson**
UV photosensitivity in a Ta_2O_5 rib waveguide Mach-Zehnder interferometer
In press, scheduled in IEEE Photon. Technol. Lett., Vol. 16, No. 6, June 2004.
5) **C. Y. Tai, J. S. Wilkinson, N. M. B. Perney, M. C. Netti, F. Cattaneo, Chris E. Finlayson, and J. J. Baumberg**
Determination of nonlinear refractive index in a Ta_2O_5 rib waveguide using self-phase modulation
Submitted to Appl. Phys. Lett.
6) **B Unal, D. P. Shepherd, C. Y. Tai, M. C. Netti, J. S. Wilkinson, and G. J. Parker**
Nd:Ta_2O_5 rib waveguide laser
To be submitted to Appl. Phys. Lett.

At Conferences

1) **A. Favre, E. Lee, V. Apostolopoulos, C. B. E. Gawith, C. Y. Tai, E. M. Taylor, Y. Kondo, and F. Koizumi**
Fabrication and characterization of planar and channel waveguides in bismuth-based oxide glasses
Photonics West, San Francisco, 25-31 Jan 2003
2) **C. Y. Tai, B. Unal, J. S. Wilkinson, M. A. Ghanem, and P. N. Bartlett**
Self-assembled microsphere gratings on rib waveguides
ECIO 2003, Prague, 2-4 Apr 2003 WeA2.4
3) **S. Pissadakis, A. Ikiades, C. Y. Tai, N. P. Sessions, and J. S. Wilkinson**

Sub-micron period grating structures in Ta_2O_5 thin oxide films patterned using UV. laser post-exposure chemically assisted selective etching
E-MRS, Strasbourg, 10-13 Jun 2003 H-IV.3

4) **C. Y. Tai, J. S. Wilkinson, N. M. B. Perney, M. C. Netti, and J. J. Baumberg**
Self-phase modulation induced spectral broadening of ultrashort laser pulses in tantalum pentoxide (Ta_2O_5) rib waveguide
CLEO Pacific Rim 2003, Taipei, 15-19 Dec 2003 TH2F-(5)-4